Cover Page

Universiteit Leiden

Author: Khmelinskii, Artem
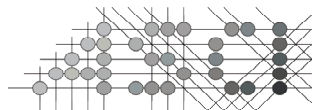**Title**: Multi-modal small-animal imaging: image processing challenges and applications
Issue Date: 2013-10-09

Multi-modal small-animal imaging:
image processing challenges and applications

Colophon

Multi-modal small-animal imaging: image processing challenges and applications
Ph.D. thesis with a summary in Dutch

Leiden University Medical Center (LUMC)–Leiden University, Leiden
the Netherlands

Advanced School for Computing and Imaging

Multi-modal small-animal imaging:
image processing challenges and applications

Proefschrift

ter verkrijging van

de graad van Doctor aan de Universiteit Leiden,

op gezag van Rector Magnificus Prof. mr. C. J. J. M. Stolker,

volgens besluit van het College voor Promoties

te verdedigen op woensdag 9 oktober 2013

klokke 10.00 uur

door

Artem Khmelinskii

geboren te Novosibirsk (Rusland)
in 1984

Promotiecommissie

promotor: Prof. dr. ir. B. P. F. Lelieveldt
Leiden University Medical Center
Delft University of Technology

co-promotor: Dr. ir. M. Staring
Leiden University Medical Center

overige leden: Prof. dr. M. Hoehn
Max Planck Institute for Neurological Research, Cologne

Prof. dr. ir. M. Hendriks-de Jong
Erasmus Medical Center, Rotterdam

Aan mijn familie

Contents

Chapter 1

Introduction

1.1   Background

In pre-clinical research, whole-body small animal imaging is widely used for the *in vivo* visualization of functional and anatomical information to study the different biological processes that take part in cancer, neurological and cardiovascular diseases, and help with a faster development of new drugs. Mice in particular are used, not only because they are small, have a fast reproduction rate, are easy to handle and widely available, but also because they share about 97.5% of human DNA [1, 2].

With the miniaturization of different clinical imaging equipment [3] the importance of small-animal imaging continues to grow [4]. Functional information (changes in metabolism, blood flow, regional chemical composition and absorption—physiological activities) is provided by imaging modalities such as positron emission tomography (PET), single-photon emission computed tomography (SPECT) and specialized magnetic resonance imaging (MRI). Both PET and SPECT have a high sensitivity and only nanomolar concentrations of molecular probes are needed for imaging. In SPECT, the nuclear isotopes are more readily available, cheaper, and have longer half-lives as compared to PET. PET however, has a slightly higher sensitivity [5].

Structural imaging modalities like radiography, computed tomography (CT), MRI and ultrasound provide detailed depictions of anatomy. μCT nowadays combines excellent spatial resolution with fast acquisition times. It is an excellent modality for bone imaging. Ultrasound is a real-time imaging modality that allows to visualize blood flow *in vivo*, and can be used to study blood flow and cardiac function in mice. It is extremely cost-effective and non-invasive. MRI provides good spatial resolution and has excellent contrast resolution to distinguish between normal and pathological tissue.

Optical imaging modalities, such as bioluminescence imaging (BLI), Fluorescence Imaging (FLI) and near-infrared (NIR) fluorescence imaging offer a high sensitivity in visualizing molecular processes *in vivo*. Optical imaging is fast and easy to perform, and relatively inexpensive. Bioluminescence imaging is often employed for assessing therapeutic response because of its excellent sensitivity whilst fluorescence imaging facilitates tumor growth monitoring because of its quick and convenient multiple time-point image capture [5].

Different combinations of these imaging techniques with targeted molecular contrast agents, can provide a window on the molecular processes in combination with structural changes followed in time in living animals without sacrificing them. This has the potential to advance several aspects of medicine, from fundamental research to early diagnosis to drug development.

1.2   Image processing challenges and motivation

With all these advances in image acquisition, the problem is shifting from data acquisition to data processing. The organization, analysis and interpretation of this heterogeneous integrated whole-body imaging data (Figure 1.1) has become a demanding task for the following reasons:

- the postural variability of the subjects between scans. There are little to no standardized protocols for whole-body animal imaging. If a subject is imaged using different imaging modalities and protocols, during follow-up studies or cross-sectional studies, the subject is positioned in different ways and postural variations occur (head, back and front limbs, *etc.*). This greatly complicates data analysis and comparison. Although there are some multimodality animal holders, to date they are not widely used or generally compatible with all the different scanners, and even with the use of the holders, there are still significant differences in animal posture in longitudinal studies

- the high-throughput nature of the data. More and more small-animal imaging is used in a life-span setting for drug development, in cancer studies and developmental studies. Exploring, detecting, visualizing and quantifying those changes in a robust way has become essential to utilize the full potential of the data

- the heterogeneous image structure. Some modalities provide 2D images (BLI), other, 3D (μMRI, μCT). Some are photographs, other are tomographic modalities. Some provide full whole-body information, other only functional information on only specific organs or lesions. Adding the temporal dimension, 4D images are used in follow-up and cross-sectional studies using different animals

- animal variability. Different animals are used, specific to the biological problem at hand. Different studies can have animals with different strain, size, age, body fat percentage or population. Comparing side-by-side, different animals on a common reference plane will thus facilitate the data analysis and quantification

Integrated imaging (molecular–to–organ–to–whole-body)
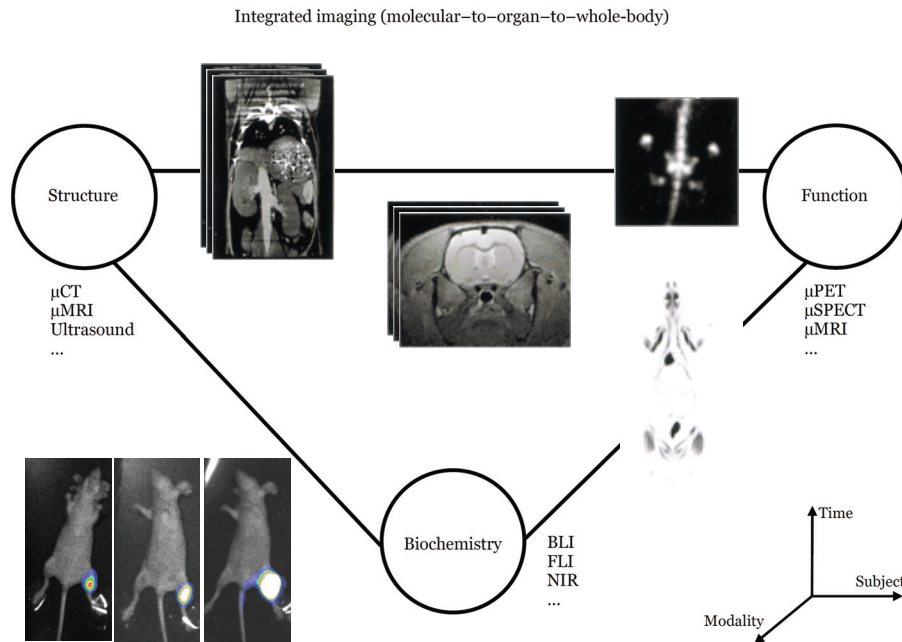
Figure 1.1 Organizing, analyzing and interpreting heterogeneous imaging data has become a demanding task for the following reasons: (i) the high-throughput nature of the data (longitudinal and developmental studies); (ii) the heterogeneous image structure (2D BLI images, 3D MRI and CT data); (iii) sometimes the whole-body is imaged, sometimes only a specific organ (*e.g.:* brain imaging); (iv) the postural variability of the subjects between scans (as depicted here in the example given for the BLI photographs)

1.3 Previous work

In recent years various approaches were proposed to deal with this multi-modal heterogeneous data in order to try to maximally exploit its information complementarity. Nevertheless, in relation to the whole-body imaging data, not much work is available. Joshi *et al.* [6] proposed a method for fitting an elastically deformable mouse atlas to surface topographic range data acquired by an optical system; Savinaud *et al.* [7] proposed a novel model-based approach to track animals in 3D from monocular video which allows the quantification of BLI signal on freely moving animals. Suh *et al.* [8] published a serial registration method to both serial µCT and µSPECT mouse images. However, these methods either do not incorporate the extremities, or were developed only for a portion of the body.

One way of handling the abovementioned problems is to use whole-body atlases. Atlases may consist of a 3D, sometimes 4D, whole-body or organ-based geometric representations. This enables mapping functional activity and anatomical variability among individuals and populations, integrating the data across modalities and quantifying change in follow-up studies. Gutierrez *et al.* [9] developed a method where automated analysis of small animal PET studies is performed through deformable registration to an atlas. This method however

depends on the availability of a correspondent co-registered CT dataset. In [10], Suh *et al.* developed a weighted demons registration method that can give preferences to particular regions of the input image using a weight image to register whole body rat CT image and PET images. Wang *et al.* [11] proposed in a simulation study the use of non-tomographic modalities like X-ray projections, to provide organ-level anatomical references of small animals in 3D by registering a digital mouse atlas. Le *et al.* [12] on the other hand developed an automatic non-rigid registration of whole body CT mice images. This method however cannot deal with very large postural differences.

As such, the recent interest in atlas based approaches has enabled combinations of different modalities, mainly in pairs. However, little to no work has been reported that enable combining several (>2) modalities into a comprehensive analysis framework, that also allows the study of follow-up data.

1.4   Contextualization

In this thesis, we further explore the approach as depicted in Figure 1.2, that served as a basis for the molecular image analysis research as performed at Laboratorium voor Klinische en Experimentele Beeldverwerking (LKEB)–LUMC. This approach is based on an *articulated* whole-body atlas as a common reference to normalize the geometric heterogeneity caused by postural differences, anatomical differences between individuals and geometric differences between imaging modalities. Mapping to this articulated atlas has the advantage that all the different imaging modalities can be (semi) automatically registered to a common anatomical reference; postural variations can be corrected, and the different animals can be scaled properly.

In the context of this framework (Figure 1.2), Wildeman *et al.* [13] proposed a 2D/3D registration of µCT data to multiview photographs based on a 3D distance map combining optical/BLI data with CT. Baiker *et al.* [14] on the other hand, presented a fully automated skeleton registration and organ approximation method using an articulated whole-body atlas in µCT mouse data [14]. This method was validated on 41 CT datasets and was successfully used to follow osteolytic lesions quantitatively and visually over time [14].

Kok *et al.* focused on integrating the whole-body data exploration across scale and time. For this purpose, he introduced the Articulated Planar Reformation (APR) algorithm [15], where after registering the articulated atlas to the data at hand, that data is reformatted along individual skeletal elements, and displayed in the atlas reference view. In this view, each volume of interest (VOI) corresponds to a single bone, which can be interactively selected for direct comparison with the corresponding VOI at another time-point or of another subject. Comparative visualization techniques that automatically highlight change over time were also provided [15].

A part of molecular image analysis research performed at LKEB–LUMC was dedicated to small animal brain data. Scheenstra *et al.* developed an automated

morphometry method for mouse brain MRI analysis with application to Alzheimer's Disease research in transgenic mice [1, 16, 17, 18].

Abdelmoula *et al.* recently proposed an automatic registration method to fuse both microscopic optical histology images and matrix assisted laser desorption ionization imaging mass spectroscopy (MALDI-IMS) data of the mouse brain. This allows to correlate the information about the neuroanatomical structures provided by the former with the chemical/molecular information provided by the latter. This assists in the early detection and diagnosis of migraine.

Mahfouz *et al.* is currently studying correlations between the specificity of certain groups of neuroreceptors to different regions of the mouse brain. The goal is to understand which genes/regulators are co-expressed with each neuroreceptor in different brain regions and link the functions of these neuroreceptors, genes and regulators to these brain regions.
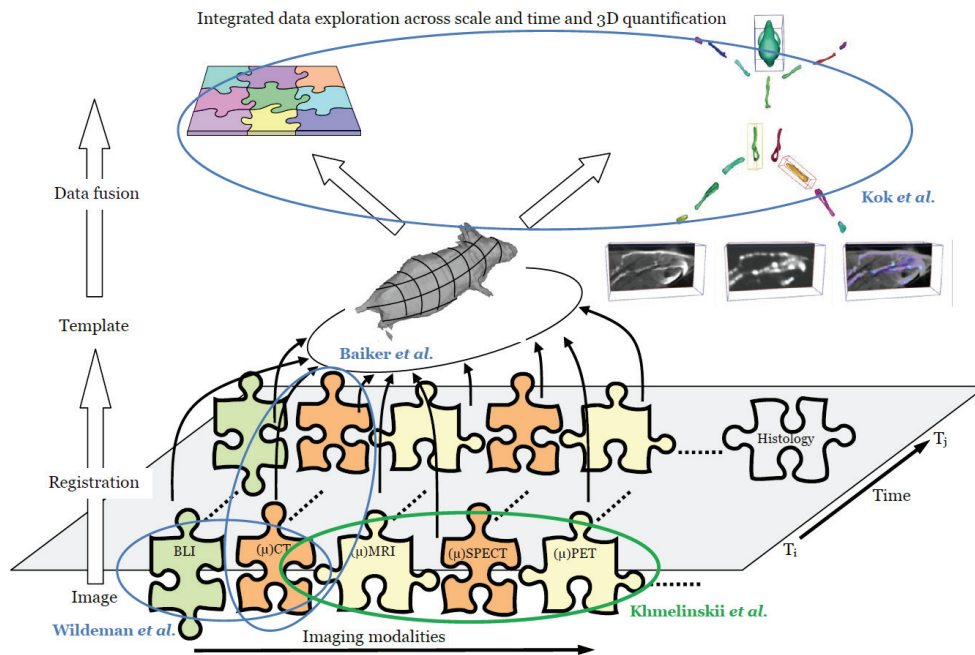
Figure 1.2 Overview of the proposed integrated approach. The data acquired using different imaging modalities for different time-points is registered to the common reference, which in this case is an *articulated* whole-body atlas. Once the data is in the atlas reference plane, it can be reformatted into individual bone VOIs. This allows normalized side-by-side visualization of the follow-up or multi-modal or cross-sectional data and quantification can be applied on a per VOI basis

1.5   Scope of this thesis

As mentioned above, in Figure 1.2, aspects such as whole-body follow-up registration and integrated visualization in the general approach have been addressed. In this thesis, we have focused on three complementary aspects, and worked towards an automated analysis pipeline for quantitative small animal image analysis. The specific goals of this thesis are:

(i)   to further generalize the articulated atlas-based registration method to the multi-modality component of the global approach presented in Figure 1.2, focusing on SPECT and MRI whole-body mouse data

(ii)   to expand the Articulated Planar Reformation algorithm by linking it to recently introduced resolution-enhancing MR reconstruction techniques which enable "zooming in" on small anatomical details not detectable with conventional MRI

(iii)   to prove the added value of atlas-based analysis of multi-modal follow-up data in a life-science study of the ageing processes in the brain, with a specific focus on multi-contrast MR rat brain data

1.6   Thesis outline

The remainder of this thesis is structured as follows.

In **Chapter 2**, an overview of the construction process of an articulated small animal atlas together with its applications is described. Using three publicly available whole-body small animal atlases (MOBY mouse [19], Digimouse [20] and *SD* Rat [21, 22]), each skeleton is segmented manually into individual bones or bone groups. For each bone, its corresponding joint(s) locations together with anatomically realistic degrees of freedom are defined. These labeled atlases form the basis of the methodology presented in Chapters 3, 4 and 5.

In **Chapter 3,** a method for whole-body μSPECT mouse data segmentation and visual analysis is presented, provided that a tracer that is resorbed by the skeleton is used during the acquisition. It is an extension of the method previously developed for segmentation of *in vivo* whole-body μCT data combined with the articulated planar reformation (APR) algorithm. The articulated MOBY atlas presented in Chapter 2 is registered to the SPECT skeleton following a hierarchical anatomical tree. First, the atlas is coarsely registered to the entire skeleton and then, starting with the skull, each atlas bone is accurately registered to the correspondent bone in the data using the Iterative Closest Point (ICP) approach. After the atlas is registered to the data, the APR algorithm is applied to reformat the segmented data into segments corresponding to a mouse atlas and thus mapping the data to a standardized atlas space for interactive exploration and side-by-side visualization of follow-up, or multi-modal or cross-sectional whole-body data.

Chapters 4 and 5 focus on MRI mouse data. In **Chapter 4,** a novel semi-automated atlas organ and bone approximation for µMRI mouse data is presented. Guided by anatomically realistic kinematic constraints imposed by the articulated MOBY atlas the user interactively identifies a number of joints/landmarks in the MRI dataset. Individual atlas bones are automatically mapped to the target data based on the joint correspondences and the organs are mapped using Thin-Plate-Spline interpolation. In **Chapter 5,** the relevance of combining the articulated atlas-based segmentation and articulated planar reformation solutions for whole-body mouse data is further extended. An end-to-end integrated interactive approach is presented where, guided by BLI hotspots, VOIs in whole-body mouse MRI are super-resolution reconstructed (SRR) and presented in the standardized atlas space complemented by anatomical CT, for study of (micro) bone metastasis. This approach allows to overcome the limitations of CT in investigating small/micro tissue-events like micro tumors (less than half slice thickness), soft tissue tumors pathology, the homing of labeled stem cells or disease and inflammatory test pools. It also allows to overcome the high computation demand of the SRR technique when applied to large datasets (whole-body mice in this case).

Chapters 6 and 7 are dedicated to an explorative study of juvenile development and ageing processes of the brain. In **Chapter 6,** a visualization platform for side-by-side exploration of co-registered high-throughput, follow-up, cross-sectional, multi-contrast MRI rat brain data is presented. This tool is built to assist in the exploration of this high-throughput and highly heterogeneous life-span rat brain data. Its functionality and utility in molecular imaging research are evaluated by means of a case study evaluation with three domain experts. In **Chapter 7** results of this development and ageing study are presented.

In **Chapter 8,** main findings of each chapter are summarized and future work is discussed.

References

[1]   Scheenstra A. *Automated morphometry of transgenic mouse brains in MR images* 2011

[2]   Fox J. G., Barthold S. W., Davisson M. T. *et al. The Mouse in Biomedical Research: Diseases* Academic Press, 2nd edn. 2007.

[3]   Massoud T. F. and Gambhir S. S. *Molecular imaging in living subjects: seeing fundamental biological processes in a new light* Genes and Development 17(5): 545–580 2003

[4]   Lelieveldt B. P. F., Botha C. P., Kaijzel E. L. *et al. Towards integrated analysis of longitudinal whole-body small animal imaging studies* Proc IEEE Intal Conf on Acoustics, Speech and Signal Processing 5768–5771 2011

[5]   Koo V., Hamilton P. W. and Williamson K. *Non-invasive in vivo imaging in small animal research* Cellular Oncology 28: 127–139 2006

[6]   Joshi A. A., Chaudhari A. J., Li C. *et al. Posture matching and elastic registration of a mouse atlas to surface topography range data* Proc IEEE Intl Symp Biomed Imaging 366–269 2009

[7]   Savinaud M,. de La Gorce M., Maitrejean S. *et al. Model-based multi-view fusion of cinematic flow and optical imaging* Med Image Comput Comput Assist Interv 13(Pt2): 668–675 2010

[8]   Suh J. W., Scheinost D., Dione D. P. *et al. A non-rigid registration method for serial lower extremity hybrid SPECT/CT imaging* Med Image Anal 15(1): 96–111 2011

[9]   Gutierrez D. F. and Zaidi H. *Automated analysis of small animal PET studies through deformable registration to an atlas* Eur J Nucl Med Mol Imaging 39(11): 1807–20 2012

[10]   Suh J. W., Kwon O. K., Scheinost D. *et al. CT-PET weighted image fusion for separately scanned whole body rat* Med Phys 39(1): 533–42 2012

[11]   Wang H, Stout D. B. and Chatziioannou A. F. *Mouse Atlas Registration with Non-tomographic Imaging Modalities—a Pilot Study Based on Simulation* Mol Imaging Biol 14: 408–419 2012

[12]   Li X., Yankeelov T. E., Peterson T. E. *et al. Automatic nonrigid registration of whole body CT mice images* Med Phys 35(4): 1507–20 2008

[13]   Wildeman M. H., Baiker M., Reiber J. H. C. *et al. 2D/3D registration of micro-CT data to multi-view photographs based on a 3D distance map* Proc IEEE Intl Symp Biomed Imaging 987–990 2009

[14]   Baiker M., Milles J., Dijkstra J. *et al. Atlas-based whole-body segmentation of mice from low-contrast micro-CT data* Med Image Anal 14(6): 723–737 2010

[15]   Kok P., Baiker M., Hendriks E. *et al. Articulated planar reformation for change visualization in small animal imaging* IEEE T Vis Comput Gr 16(6): 1396–1404 2010

[16]   Scheenstra A. E. H., Dijkstra J. and van der Weerd L. *Volumetry and other quantitative measurements to assess the rodent brain* Methods Mol Biol 771: 277–291 2011

[17]   Muskulus M., Scheenstra A. E. H., Braakman N. *et al. Prospects for early detection of Alzheimer's Disease from serial MR Images in transgenic mouse models* Curr Alzheimer Res 6(6): 503–518 2009

[18]   Scheenstra A. E. H., Muskulus M., Staring M. *et al.The 3D Moore-Rayleigh test for the quantitative groupwise comparison of MR brain images* Inf Process Med Imaging 21: 564–575 2009

[19]   Segars W. P., Tsui B. M. W., Frey E. C. *et al. Development of a 4D digital mouse phantom for molecular imaging research* Mol Imag Biol 6(3): 149–159 2004

[20] Dogdas B., Stout D., Chatziioannou A. *et al. Digimouse: a 3D whole body mouse atlas from CT and cryosection data* Phys Med Biol 52(3): 577–587 2007

[21] Bai X., Yu L., Liu Q. *et al. A highresolution anatomical rat atlas* J Anat 209(5): 707–708 2006

[22] Wu L., Zhang G., Luo Q. *et al. An image-based rat model for Monte Carlo organ dose calculations* Med Phys 35(8): 3759–3764 2008

Chapter 2

# Articulated whole-body atlases for small animal image analysis: construction & applications

Abstract

Using three publicly available small-animal atlases (*Sprague–Dawley* rat, MOBY, and Digimouse), we built three articulated atlases and present several applications in the scope of molecular imaging. Major bones/bone groups were manually segmented for each atlas skeleton. Then, a kinematic model for each atlas was built: each joint position was identified and the corresponding degrees of freedom were specified. The articulated atlases enable automated registration into a common coordinate frame of multimodal small-animal imaging data. This eliminates the postural variability (*e.g.,* of the head, back, and front limbs) that occurs in different time steps and due to modality differences and nonstandardized acquisition protocols. The articulated atlas proved to be a useful tool for multimodality image combination, follow-up studies, and image processing in the scope of molecular imaging. The proposed models were made publicly available.

2.1   Introduction

In preclinical research, different imaging modalities are used for the *in vivo* visualization of functional and anatomical information. Structural imaging modalities such as MRI, CT, and ultrasound provide detailed depictions of anatomy; PET, SPECT, and specialized MRI protocols add functional information. In addition, optical imaging modalities, such as BLI and near-infrared fluorescence imaging, offer a high sensitivity in visualizing molecular processes *in vivo.* In combination, these modalities enable the visualization of the cellular function and the follow-up of molecular processes in living organisms without perturbing them.

Due to the high number of existing imaging modalities, a new, different challenge emerged: how to best combine and analyze all these data? The problem is shifting from data acquisition to data organization, processing and analysis, and the main difficulty of this task is the enormous data heterogeneity and volume/throughput. The above-mentioned imaging techniques provide 2D, 3D, or 4D images depending on modality and are used in follow-up and cross-sectional studies using different animals (according to strain, size, age, body fat percentage, population). One other very important factor is the postural variability: there is no standardized protocol for imaging. If a subject is imaged using different imaging modalities and protocols, during follow-up studies or if different animals are used, the subject is positioned in different ways and postural variations occur (*e.g.,* of the head, back, and front limbs, *etc.;* Figures 2.1, 2.3, 2.4). Although there are some multimodality animal holders, to date, they are not widely used, and even with the use of the holders, there are still significant differences in animal posture between different time points. All these factors contribute to the large data heterogeneity.
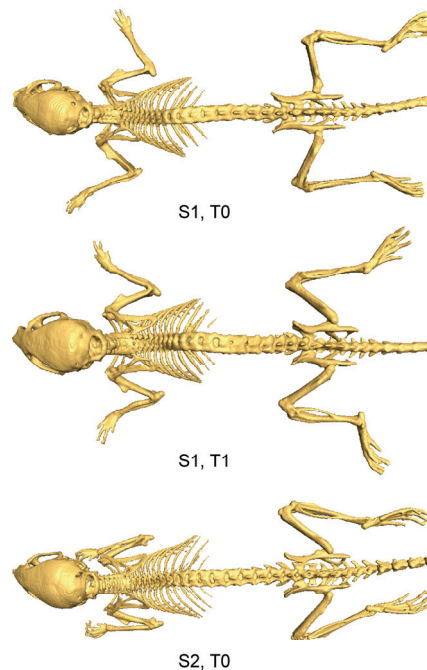
Figure 2.1 Illustration of the postural variability (limbs, head) that occurs in follow-up and cross-sectional molecular imaging studies: top and middle mouse—same subject S1, two time steps T0 and T1; bottom mouse—different subject S2

One way of handling this problem is to use atlases. In biomedical imaging research, anatomical atlases have proven to be useful for defining a standard geometric reference for further subject analysis and meaningful comparisons. Atlases may consist of a 3D, sometimes 4D, whole-body or organ-based geometric representation. This enables mapping functional activity and anatomical variability among individuals and populations. Considering the issues mentioned above, having such a model allows for a more effective way to combine, structure, and execute all sorts of comparisons and correlations within the data. For example, it is possible to make population brain studies in a specific time frame. For that, brain images from each individual, obtained through MRI, PET, and other imaging techniques, are spatially warped to a brain template. After combining the data, inferences are made about tissue identity at a specific location by referring to the atlas or looking for variability of those locations within that population.

There are a large number of clinical atlases that are available and widely used in population imaging, image segmentation, image registration, and in shape differences and follow-up studies. Three of the most well-known and used atlases within the clinical research scope are the Talairach brain atlas [1], the Visible Human Project whole body atlas [2], and the 4D NCAT torso phantom [3]. The Talairach atlas consists of a standard 3D coordinate space with labeled regions and structural probability maps and is available for clinical use. This atlas is not only used for stereotactic and functional neurosurgery but also in human brain mapping, neuroradiology, medical image analysis, and neuroscience education. The Visible Human Project consists of manually annotated MRI, CT, and cryosection images

for both male and female human bodies. The available datasets were designed to serve as a reference for the study of human anatomy and have been applied to a wide range of educational, diagnostic, treatment planning, virtual reality, and artistic, mathematical, and industrial uses [2]. The 4D NCAT phantom on the other hand provides a more realistic model of the human anatomy and motions because it does not sacrifice any flexibility to model the anatomical variations and patient motion and has been used in SPECT simulations [3]. For a more detailed survey on computational anatomical and physiological models, see [4].

Within the scope of preclinical molecular imaging research, there are various mouse and rat atlases with different characteristics and purposes, acquired using different techniques (CT, MRI, cryosectioning, *etc.*). Many of those are thoroughly described and published in literature and are publicly available: the LONI Rat atlas published by the UCLA Laboratory of Neuro Imaging [5] and other brain focused atlases [6–10], the Edinburgh Mouse Atlas Project [11] that describes and presents a 3D model of the mouse embryo, the MRI Atlas of Mouse Development from the California Institute of Technology [12], the Mouse Cochlea Database made by the University of Minnesota [13], and whole-body small animal atlases like MOBY mouse [14] and Digimouse [15] and the high resolution *Sprague–Dawley (SD)* rat [16, 17].

However, these mouse and rat atlases are either specific, organ-dedicated atlases (brain, hypothalamus, heart, *etc.*), low-resolution, or cannot deal with the large postural variations that occur within the scans acquired using different imaging modalities during follow-up studies (different time steps) or if different animals are used because mice are positioned in different ways when scanned and there is no standardized acquisition protocol.

The work described here addresses the abovementioned problems by introducing articulations in three existing whole-body atlases: (1) Digimouse [15], (2) MOBY mouse [14], and (3) high-resolution *SD* rat [16, 17]. A kinematic model is built for each atlas where bones in each skeleton are manually segmented and labeled, and the corresponding degrees of freedom (DoFs) for each joint are defined.

Mapping to this articulated atlas has the advantage that all the different imaging modalities can be (semi) automatically registered to a common anatomical reference; postural variations can be corrected, and the different animals (according to strain, size, age, body fat percentage) can be scaled properly.

The goals of this work are to:

(i)   Introduce the concept of the articulated whole-body small animal atlas

(ii)   Present and discuss several implemented application examples: atlas to μCT data registration, follow-up μCT studies, cross-sectional μCT studies, multimodality atlas to BLI and μCT image registration and analysis, and atlas to μMRI data approximation; and

(iii) Make these three articulated whole-body small animal atlases publicly available

16

2.2 Methods

2.2.1 Atlas descriptions

Presently, in the work described here, three small animal atlases are used. In this section, a brief description of each one is presented.

MOBY (mouse whole-body) atlas
Segars *et al.* generated a realistic 4D digital mouse phantom based on high-resolution 3D MRI data from Duke University. The organs of this atlas were built using non-uniform rational b-spline (NURBS) surfaces, which are widely used in 3D computer graphics.
The final package includes a realistic 3D model of the mouse anatomy and accurate 4D models for the cardiac and respiratory motions. Both the cardiac and respiratory motion models were developed based on cardiac gated black-blood MRI and respiratory gated MRI data from the University of Virginia. It has been used in simulation studies in SPECT and X-ray CT [14].

Digimouse atlas
Dogdas *et al.* constructed a 3D whole-body multimodal mouse atlas from co-registered X-ray μCT and color cryosection data (anatomical information) of a normal nude male mouse. It also includes PET data (functional information) representing the distribution of a mixture of the tracers [18F] fluoride and 2-deoxy-2-[18F]fluoro-D-glucose within the mouse. The image data were co-registered to a common coordinate system using the fiducials and resampled to an isotropic 0.1 mm voxel size. Using interactive editing tools, several organs were segmented and labeled.

The final atlas consists of the 3D volume (in which the voxels are labeled to define the anatomical structures listed above) with co-registered PET, X-ray CT, and cryosection images and can be used in 3D BLI simulations and PET image reconstruction [15].

High-resolution SD rat atlas
Xueling *et al.* built a highresolution 3D anatomical atlas of a healthy adult *SD* rat from 9,475 horizontal cryosection images (at 20 μm thickness). Coronal and sagittal section images were digitized from the horizontal sections and anatomical structures under the guidance of an experienced anatomist. The 3D computerized model of the rat anatomy was generated using a parallel reconstruction algorithm and interactive atlas-viewing software was developed that offers orthoslice visualization, featuring zoom, anatomical labeling, and organ measurement. Also, an interactive 3D organ browser based on a virtual reality modeling language was deployed on a website. The models of each organ and tissue constructed from the images were used for calculations of absorbed dose from external photon sources [16, 17].

Figure 2.9 in the Appendix provides a visual comparison between the original atlases described above. While the MOBY and Digimouse atlases are quite similar in content, they differ in terms of the species of the mouse, the types of organs defined, resolution, and in the modalities from which they were constructed. Also, the MOBY atlas includes a model of cardiac and respiratory motion. In Table 2.4 in

the Appendix, an overview of the main differences between these three atlases is presented.

2.2.2   Articulated atlas constructions

In all the abovementioned atlases, the included skeletons do not distinguish between single bones and joints. To render the registration performance independent of the data acquisition protocol and large postural variations due to postural heterogeneity between scans, we present a segmentation of the skeleton into individual bones and add anatomically realistic kinematic constraints to each joint.
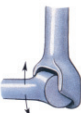
Segmenting the skeleton
The first step was to manually segment the following bones/bone groups in each atlas from the skeleton using the Amira™ V3.1 software [18], guided by anatomical text books [19, 20], and a high resolution CT scan of a real mouse: *scapula, humerus* (upper front limb), *clavicula* (collarbone, rat only), *ulna-radius* (lower front limb), *manus* (front paw), *femur* (upper hind limb), *tibia-fibula* (lower hind limb), *pes* (hind paw), *caput* (skull), *columna vertebralis* (spine), *costae* (ribs), *sternum* (chest bone), and *pelvis*. The resulting labeled skeletons for each atlas can be seen in Figure 2.2

Introducing joint kinematics
In the second step, a kinematic model for each atlas was built, *i.e.,* each joint position was identified and the corresponding DoFs were specified. Two types of joints were distinguished: ball joints and hinge joints.

In Table 2.1, the DoFs for the ball and hinge joints can be seen. These DoFs are anatomically correct and were defined according to expert specifications described in literature [19, 20].

Joint types	Modeled joint	DoFs of the articulated bone
Ball joint	Shoulder Wrist Hip Ankle	3 translations 3 rotations 3 scalings
Hinge joint	Elbow Knee	3 translations 1 rotation 3 scalings

Table 2.1 Joint types in the atlas skeleton and the correspondent DoFs [21], pictograms from [22]

2.2.3   Atlas-based whole-body registration/segmentation of small animals datasets

The skeleton is the rigid frame of the animal, in the sense of tissue stiffness. Besides the articulations of individual bones with respect to each other, little deformation takes places in the bones themselves within the same animal. This is in contrast to,

e.g., organs, which highly vary in shape, depending on the posture of the animal. Therefore, a robust registration strategy should be based on the skeleton. Although there are approaches in literature that perform small animal whole-body image registration based on the entire skeleton [23, 24], these methods may fail if large postural variations among different animals or among the same animal in a follow-up study occur.

Therefore, we propose an approach that employs the articulated skeleton model as described above for registration of the skeleton in a first step. Organs are non-rigidly matched in a second step, initialized by the result of the skeleton matching.
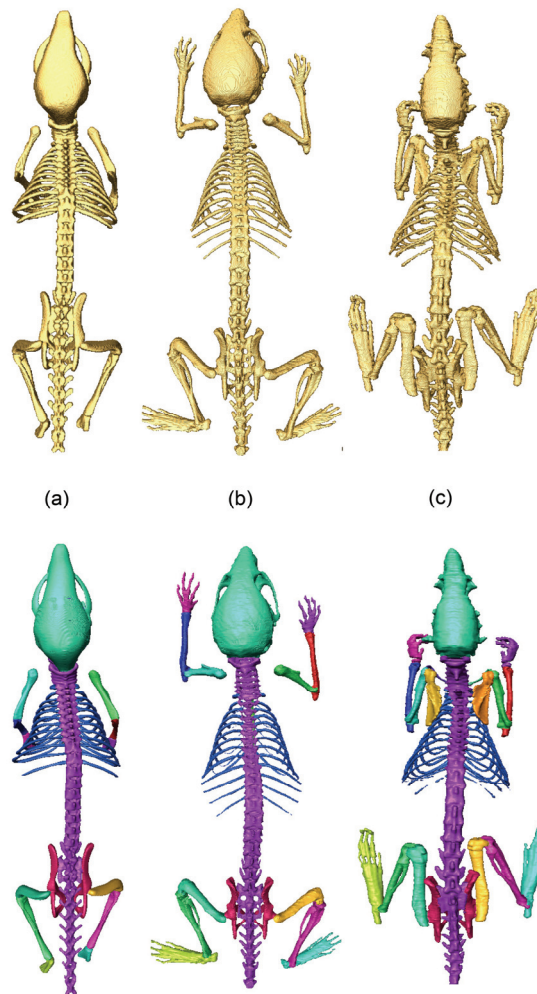
Figure 2.2 Illustration of the three segmented skeletons for each atlas: top row—before partitioning, bottom row—after partitioning. (a) MOBY, (b) Digimouse, and (c) *SD* rat

Skeleton registration
The more distal a given bone is in the skeleton, the more variable its position between acquisitions is. Therefore, if datasets of several mice are globally aligned to each other, the location of the skulls is more similar than for instance that of the paws. Given that the entire atlas skeleton is coarsely aligned to a target dataset in a

first step, all bones can subsequently be matched individually by executing the registration from proximal to distal bone segments. The registration of a distal segment is thereby constrained by the joint type of the proximal bone it connects to. For example, for the tibia, the registration is constrained by the DoFs of the knee joint. The deformation model that is required for the individual bones depends on the type of study and may vary between rigid (intra-subject) and non-rigid (inter-subject) deformation models. The selected registration criterion depends on the modality of interest. It can be a point-based (*e.g.,* Euclidean distance), surface-based (*e.g.,* Euclidean distance and surface curvature), or volume-based registration criterion (*e.g.,* Normalized Mutual Information). In this paper, we limited ourselves to a surface-based registration measure, *i.e.,* the Euclidean distance between two surfaces. Since the registration has to deal with large articulations, potentially pathological data (as a result of bone resorption) and inter-subject data, a rigid transformation model including non-isotropic scaling was chosen. This renders the registration robust to pathological cases while still taking different bone sizes into account. The registration was embedded in the Iterative Closest Point [25] framework and optimized using an interior-reflective Newton method.

Organ registration
The registered skeleton allows us to initialize the registration of several other major organs, because their location is strongly dependent on the animal posture. To realize this, the transformation model should be chosen such that it can handle the large deformations that can occur for soft tissues. Many methods have been proposed for registration of individual organs (see *e.g.,* [26, 27] for reviews), which are not discussed further here. In the applications described next, we selected thin-plate-spline (TPS) interpolation [28]. The required anatomical landmarks that define the TPS mapping are primarily derived from the registered skeleton. To this end, we compute a sparse set of initial correspondences on the animal skin by selecting the skin points closest to a set of anatomical landmarks on the skeleton (*e.g.,* the joints). From this sparse set of skin points, a denser set of point correspondences is calculated by means of an iterative matching of local distributions of geodesic distances [21]. This results in a set of correspondences on the skin and on the skeleton, which in combination define the TPS interpolants.

Evaluation metrics for registration accuracy
To evaluate the accuracy of the registration algorithm for the skeleton, skin, and organs, three different error metrics were defined [21]:

- Joint localization error is calculated as the Euclidean distance between corresponding anatomical landmarks (point-to-point distance). To this end, the locations of the upper lower limb and the lower limb-paw joints of all datasets were indicated manually using the extracted skeleton surfaces. For validation, the manually determined joint locations were compared to those automatically determined by registration of the skeleton

- Euclidean point-to-surface distance was determined to quantify border positioning errors. It was used to evaluate the registration error over the surface of the entire skeleton and skin

- Dice coefficients of volume overlap [29] were computed to assess the organ interpolation performance. The Dice coefficient is widely used in literature to assess segmentation accuracy by evaluation of the spatial overlap of a manual

and an automated segmentation. It is a voxel-based measure and therefore includes differences in object sizes as well as spatial misalignment [30]. Given the absolute volumes of a manual segmentation result V_m and an automated segmentation result V_a, the Dice coefficient is defined as the intersection of the volumes, divided by the average volume:

$$D_c = \frac{2|V_m \cap V_a|}{|V_m| + |V_a|} \quad (1)$$

2.3   Applications

In this section, three application examples are presented that employ the articulated skeleton model for analysis of follow-up, cross-sectional, and multimodality small animal imaging studies. Each application was quantitatively validated.

2.3.1   Atlas to µCT registration for follow-up and cross-sectional µCT studies

Whole-body segmentation based on articulated skeleton registration
Anatomical referencing of molecular events inside the animal using non-contrast-enhanced µCT is difficult, because although the skeleton can be extracted easily from the data as a whole it is often required to know exactly in which bone the molecular event takes places and because the poor soft-tissue contrast in the abdomen complicates organ localization and renders registration very difficult. Above that, µCT is often used in oncological studies to assess metastatic activity in bone, and since the locations where possible metastases can develop greatly varies, a very flexible data acquisition protocol with respect to animal positioning in the scanner is required. For such applications, animal posture, shape, and limb position may vary substantially.

To deal with the challenges specific to µCT, we employ the fully automated articulated atlas-based skeleton and organ segmentation method for non-contrast-enhanced whole-body data of mice [21] described in the section above. The skeleton is represented with a surface, derived from the modified MOBY atlas.

To test the proposed method, data acquired during a study of the metastatic behavior of breast cancer cells were used. Breast cancer has a preference to metastasize to bone, and at the location of a metastatic lesion, osteolysis occurs, causing structural damage in the skeleton (fractures or completely resorbed bones). The subject was injected with luciferase positive human MDA-MB-231 breast cancer cells into the cardiac left ventricle. The animal was scanned 40 days after cell injection to screen for possible small amounts of photo-emitting tumor cells in bone marrow/bone mimicking µCT-metastatic spread. Nine anesthetized mice (*BALB/c,* Charles River WIGA, Sulzfeld, Germany), 6–9 week old, eight female, one male, with a mean weight of 22.23±2.18 g, were acquired with a Skyscan™ (Kontich, Belgium) 1178 µCT scanner. Fourteen 3D data volumes of the nine mice were acquired with step size 1°, 50 keV X-ray voltage, an anode current of 200 µA, an aluminum filter of 0.5 mm thickness, an exposure time of 640 ms, and without

using a contrast agent. The reconstructed datasets covered the range between −1,000 (air) and +1,000 (bone) Hounsfield units. Neither cardiac nor respiratory gating was used. The mice were scanned in arbitrary prone and supine postures and arbitrary limb positions. Table 2.2 shows the joint localization and point to surface errors for before and after registering the articulated atlas skeleton, lungs, and skin to the data. Subsequently, the brain, heart, liver, kidneys, spleen, and stomach were mapped from the atlas to the subject using TPS interpolation [21].

	Before registration	After registration
	Joint localization error (mm)	
Right knee	14.29 ± 5.51	0.75 ± 0.29
Right ankle	18.70 ± 5.87	1.82 ± 1.01
Left knee	16.61 ± 4.80	0.77 ± 0.26
Left ankle	19.93 ± 5.15	1.69 ± 1.14
Right elbow	5.66 ± 2.11	1.31 ± 0.44
Right wrist	15.56 ± 4.49	1.27 ± 0.53
Left elbow	5.23 ± 2.96	1.23 ± 0.39
Left wrist	18.04 ± 6.47	1.21 ± 0.56
	Euclidean point to surface distance (mm)	
Entire skeleton	3.68 ± 0.77	0.58 ± 0.03
Lungs	1.27 ± 0.26	0.47 ± 0.03
Skin	11.06 ± 8.49	0.75 ± 0.53

Table 2.2 Skeleton, lungs, and skin registration results. The results are separated in two columns: before registration, *i.e.:* after the initialization alone and after registration. For the bone, the used error metric is the joint localization error, while for the lungs, skin, and the whole skeleton, it is the point to surface distance
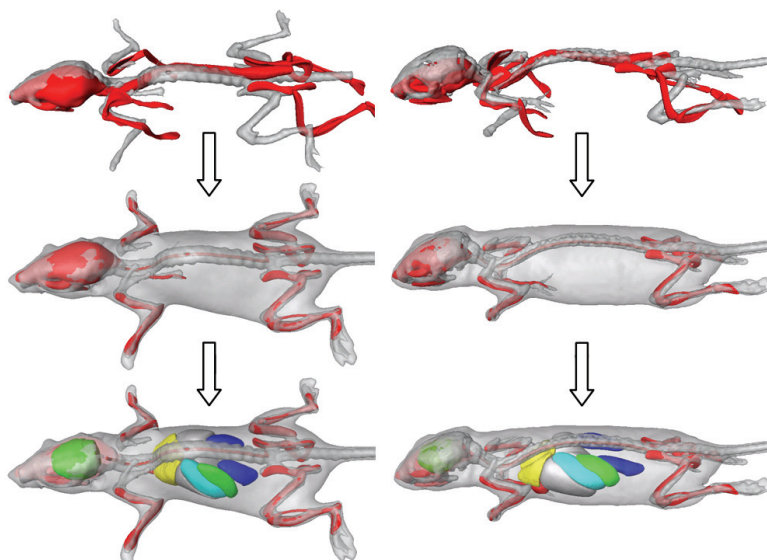
Figure 2.3 Registration results between the atlas (red) and two different subjects (gray) after coarsely aligning the skeleton (top), after the articulated registration (middle), and after organ approximation (bottom)

The result is a segmentation of the animal body into individual bones and major organs. This can be used for qualitative assessment of morphology at a single point in time in one or more animals—a cross-sectional study (Figure 2.3), or to follow morphological changes over time—a follow-up study (Figure 2.4). To facilitate the comparison of cross-sectional and follow-up data, also visualization concepts were developed that are based on mapping the data to a common reference frame and present the results simultaneously (Figure 2.5).
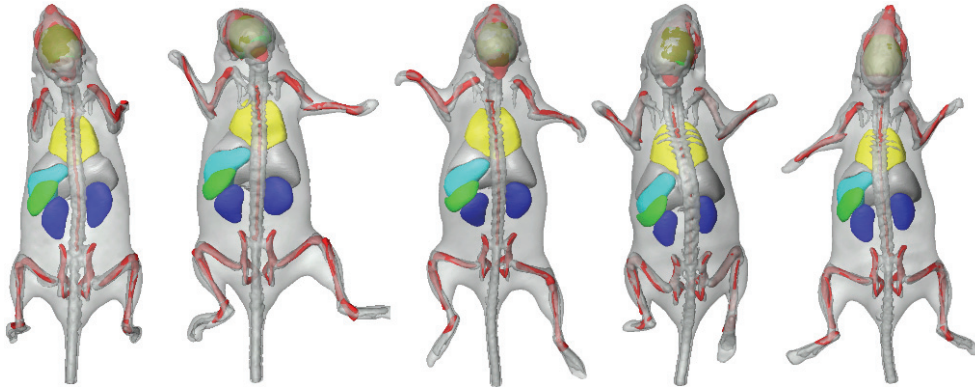
Figure 2.4 Skeleton registration and organ approximation using the same subject, at five different time points (4 weeks). The animal was put into the acquisition device arbitrarily, in supine (first three) and prone (last two) position, respectively, and the postural variations of the head, back, and front limbs are clearly visible

2.3.2 Multimodality registration, visualization and analysis

Combination of BLI and segmented µCT data
BLI is an imaging technique that has found widespread application in preclinical research over the past years. It is used to track cells and monitor the function of specific genes and processes in the cellular biochemistry with a high sensitivity in living animals. A typical application domain is oncology, where researchers aim at monitoring the development of metastases using a highly sensitive optical modality, BLI, and relate it to morphological changes using an anatomical modality like µCT [31, 32].

Since BLI does not show anatomical information, it is often overlaid on multiple 2D photographs from different angles around the animal. This, however, has the disadvantage that anatomical referencing is limited to the animal skin and, therefore, allows only coarse source localization. Thus, a combination with a real 3D anatomical modality like µCT is preferable. This requires a BLI to CT registration approach.
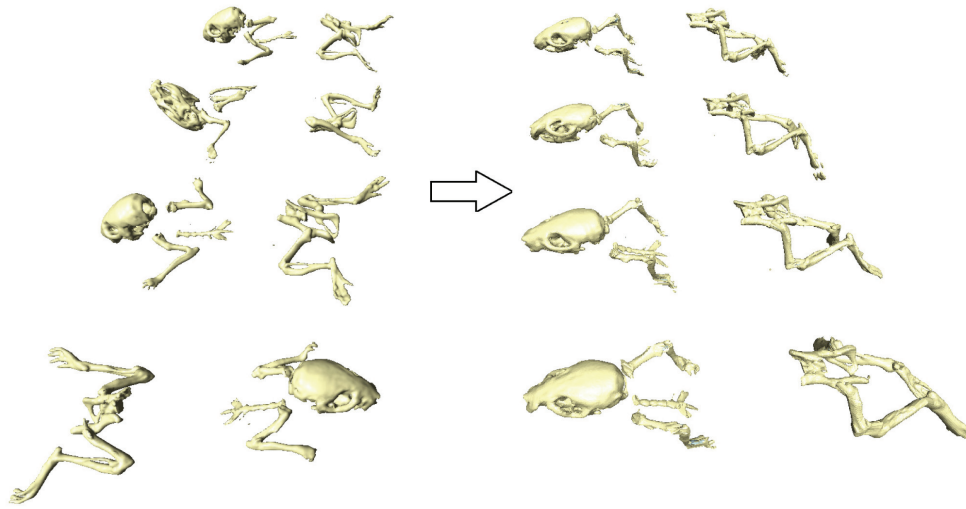
Figure 2.5 Demonstration of mapping the registered bones of four different animals from the corresponding target domain to a common reference domain (the MOBY atlas domain). The large postural differences of the animals (left) are not present any more (right), enabling a more intuitive comparison of different time points

The BLI data in this work were acquired using the Xenogen IVIS Imaging System, 3D series scanner by Caliper LifeSciences™ (Alameda, USA). The data were collected from a study with two experiments in mice on the metastatic behavior of breast cancer cells as to visually verify the reconstructed BLI sources with the injection site as seen in the μCT data. One hundred thousand RC21-luc cells-luciferase expressing human renal carcinoma cell line and 100 μl 100,000 KS483-HisLuc cells-luciferase expressing murine mesenchymal stem cell line were injected under the renal capsule and into the left heart ventricle, respectively, and scanned after 3 to 4 weeks (time for the carcinoma to establish).

Two alternative ways have been worked out to perform the BLI to CT registration. A semi-automated method, which requires manual selection of at least three anatomical landmarks both on the photographs, and the CT data were implemented. Subsequently, these corresponding landmarks are used to map one data domain to the other. As a second approach, a fully automated way to perform this registration was implemented. Based on the skin contours on the photographs, a 3D distance map is derived and used for registration of the animal skin, derived from CT [33]. In addition, the atlas to CT mapping as described above can be applied as well. The result is a fully segmented animal that serves for anatomical referencing if combined with a qualitative BLI source localization algorithm (*e.g.,* [34]) as shown in Figure 2.6. The quantitative results for the articulated skeleton atlas to μCT registration are the following: entire skeleton—before registration 4.25±12.25 mm, after registration 0.63±1.04 mm; lungs—before registration 1.27 ±2.44 mm, after registration 0.50±1.35 mm.
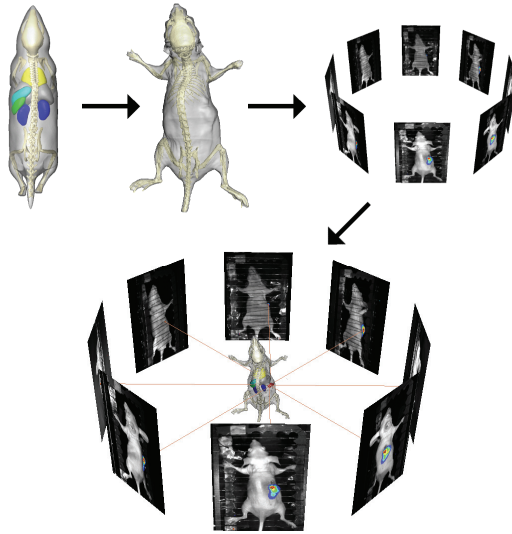
Figure 2.6 Overview of the steps towards a combined visualization of fully segmented whole-body μCT and BLI data. The MOBY atlas is registered to the μCT data and subsequently, the μCT data are registered to the BLI data using the photographs either by using manually selected landmarks or fully automatically using a 3D distance map (see text). In the resulting visualization, the BLI source (red) is shown and can be related to the skeleton and organs

2.3.3   Atlas to μMRI approximation

Organ and bone approximation for ex vivo mouse data
Since μMRI data provide greater contrast between the different soft tissues of the body but poorer bone contrast than CT data, it can be used to closely follow the changes in phenotype in studies that require genetic modifications.

A novel semi-automated organ approximation method for μMRI mouse data that considerably reduces the required user effort compared to manual segmentation was implemented. It includes the limbs and provides a shape approximation of the bones in MR data. To derive the set of skin correspondences, the user interactively points out the joints/bone landmarks guided by anatomically realistic kinematic constraints imposed by the articulated atlas. Given this set of dense skin correspondences, the organ approximation is performed using the TPS approximation as described in the "Methods" section. The bone approximation is performed by (1) automatically identifying all the joints out of the manually indicated landmarks and (2) applying a scaling and rotation to the atlas bone surfaces [35].

This MRI segmentation method was tested on female *C3H* mice perfusion fixed with formalin and 10 mM Magnevist with ultrasound guidance [36]. Imaging was performed on a 7T magnet with a four-channel VarianINOVA™ console (Varian Inc., Palo Alto, CA) multiplexed to 16 coils for parallel imaging. A spin echo sequence was used: TR/TE=650/15 ms and $(100~\mu m)^3$ voxels with an imaging time of 13 h.

Application of the registration resulted in segmentations of the limbs and six major organs: heart, spleen, lungs, kidneys, liver, and stomach. See Figures 2.7 and 2.8 where the obtained results are presented both in 2D-and 3D visualizations, respectively. Table 2.3 shows the Dice coefficients for four major organs (heart, lungs, kidneys, and liver). In all the abovementioned application examples, experiments were executed using MATLAB™ R2008b (The Mathworks, Natick, USA) and took always ≤6 min of runtime in a 2.40 GHz Intel Quad Core™, with 4 GB of RAM, Windows™ PC.
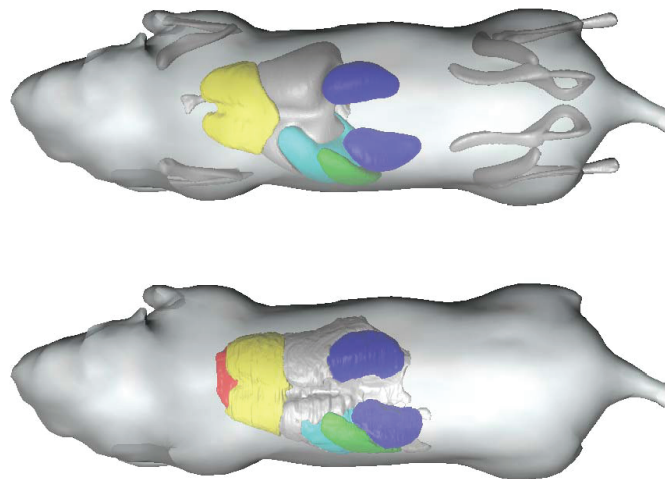
Figure 2.7 Top—Atlas-based bone and organ approximation. Bottom—Manual organ segmentation

2.4   Discussion and conclusions

This paper introduces three realistic, articulated skeleton phantoms derived from publicly available small animal atlases: Digimouse [15], MOBY mouse [14], and Rat atlas [16, 17]. A number of application examples using the MOBY atlas for such articulated atlases were presented. Mainly, it was demonstrated that articulated atlases can be used in correcting the postural variation, in referencing optical to CT data and in organ approximation. By combining the atlas with the hierarchical anatomical model and articulated registration, whole-body skeleton registration could be performed robustly, even in the presence of large postural variations: all 14 µCT datasets could be registered successfully. For the skeleton, a registration accuracy within two-voxel dimensions was achieved. This performance is comparable to the results given in [23]. However, that method takes several hours while the method presented here takes less than 10 min. Regarding the joint localization error, suboptimal registration results can occur where two adjacent long bones are pointing in almost the same direction. In some of these cases, the resulting scaling factor along the longitudinal bone axis was the maximum value that was considered anatomically realistic (scaling by 15%). As a result, parts of the distal bones were erroneously assigned to target bone during registration. Due to animal placement during acquisition, this mainly is a problem for the ankle joint and is reflected in the somewhat higher error. Also, the results for the joint localization errors are comparable to those reported in literature [40].
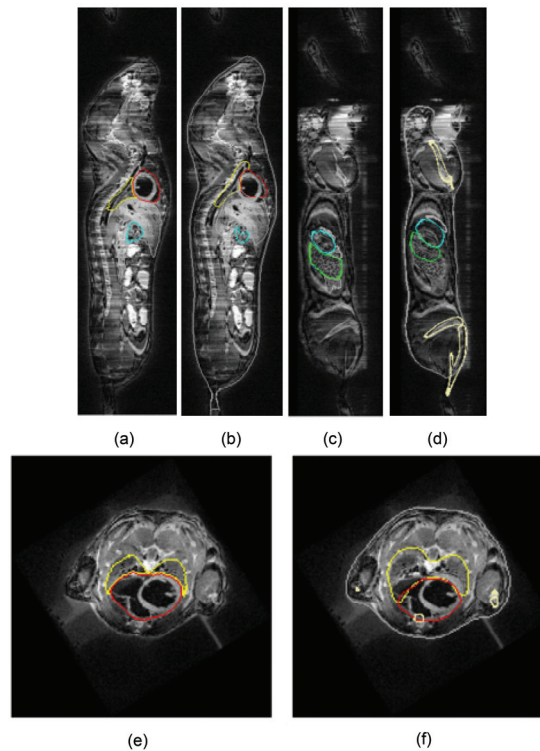
Figure 2.8 Organ and bone approximation results for μMRI mouse data: a, c, e—manual organ segmentation. b, d, f—organ and bone approximation results. Coronal and sagittal planes, respectively. yellow lungs, red heart, green spleen, cyan stomach, cream bone, gray skin, white liver. Reproduced from [35] with permission

The obtained results for the semi-automatic atlas to MRI data approximation were generally satisfactory and similar to the manual segmentations (heart, kidneys, liver), while for other organs the atlas approximations are more variable (organs with inherent shape variability such as the stomach and spleen), and errors were larger. The calculated Dice coefficients reveal "moderate" (0.41–0.6 [41]) performance for the lungs and mostly "substantial" (0.61–0.80) or "excellent" (>0.7 [42]) performance for heart, liver, and kidneys. The comparison of the calculated Dice coefficients with previously published results shows that while performing better than [37] and at a similar level as [39], the proposed method does not obtain as good results for the lungs as the method proposed in [38] (see Table 2.3). However, the example given in Figure 2.6 reveals that the proposed TPS mapping of the mouse major organs leads to a realistic approximation and can be used by biologists for qualitative anatomical referencing. Also, in the context of the intended application of combining segmented 3D data and BLI, the achieved accuracy should suffice to define a heterogeneous tissue model for Bioluminescence Tomography; it has been shown [43] that integration of tissue-specific photon properties yields more accurate and quantitative BLI source reconstruction than a homogeneous tissue model.

At the moment, μCT data are required to perform the whole-body segmentation step. To be able to obtain whole-body segmentation also in the absence of μCT data, without putting restrictions on the positioning of the animals during data acquisition, a method is under development to register the modified Digimouse

atlas to a 3D distance map, which is derived from multiple photographs. This is especially interesting for cases, where researchers are interested mainly in quantification of the light source. If morphological changes have to be studied in detail over time, a μCT scan would still be required. However, since these usually occur at a later point in time, CT data acquisition could be omitted at early time points and therefore reduce radiation burden of the animals.

The strategy applied here to make the atlases articulated was outlined to deal with major postural variations (involving long bones or large bone complexes); however, it can be extended to the whole skeleton to cope with any minor variation. One can define a kinematic model for each vertebra of the columna vertebralis (whereas here the columna vertebralis is defined as one big bone complex) and even to some non-rigid organs. Also, it is important to refer that often, depending on the task at hand, the DoFs for each bone/bone complex can be defined or redefined accordingly (*e.g.,* in [21] some additional DoFs were allowed, although they are anatomically unnecessary, to compensate for errors that have been made during the specific task of whole-body atlas to 3D mouse data registration).

	Mouse 1			Mouse 2			Mouse 3			[37]	[38]	[39]
	V_s(mm³)	V_a(mm³)	Dice	V_s(mm³)	V_a(mm³)	Dice	V_s(mm³)	V_a(mm³)	Dice	Dice	Dice	Dice
Heart	292.62	227.16	0.65	282.36	241.83	0.80	292.56	202.19	0.74	0.4673	0.81	0.8161
Lungs	421.15	392.78	0.39	429.74	437.26	0.56	344.55	362.38	0.44	0.4871	0.82	N/A
Kidneys	264.57	268.10	0.43	301.28	268.94	0.72	305.68	231.27	0.72	0.4363	0.60	0.5899
Liver	1131.77	1776.11	0.63	1087.54	1939.77	0.68	1484.82	1551.95	0.63	0.6508	0.80	N/A

Table 2.3 Organ approximation results for 3 μMRI mouse datasets: dice coefficients for four major organs—heart, lungs, kidneys, and liver. The last three columns provide a comparison with results obtained by Chaudari *et al.* [37], Baiker *et al.* [38], and Joshi *et al.* [39] for μCT data mouse data. Vs is subject volume, Va, atlas volume
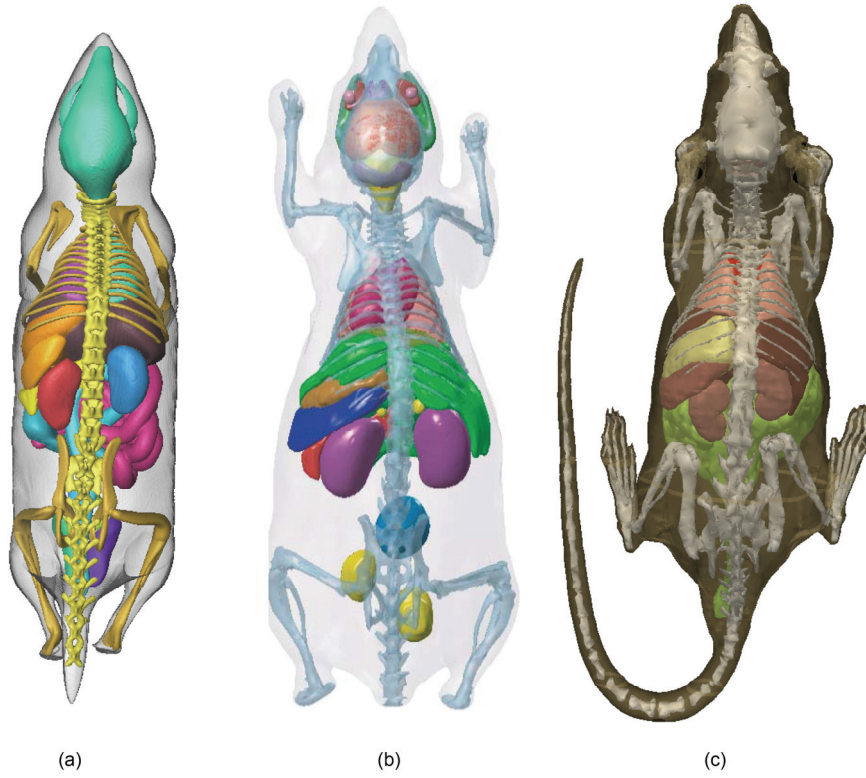
The presented articulated models were made publicly available and can be downloaded from the "Articulated Atlases Download" section of the following web address: www.lkeb.nl

Acknowledgments

Appendix

Comparison of the three original atlases

(a)　　　　　　　　　(b)　　　　　　　　　(c)

Figure 2.9 Illustration of the three original atlases: (a)—MOBY, (b)—Digimouse and (c)—*SD* Rat

	Moby mouse	Digimouse	SD rat
Made in	John Hopkins University	University of Southern California	Huazhong University of Science and Technology
Strain	*C57BL/6*	NA, nude	*Sprague-Dawley (SD)*
Gender	male	male	male
Age	15, 16 weeks	adult	~2 months
Number of Cryosectional	NA	418	horizontal, 9475
Cryosectional image Size	NA	1740x2560	4600x2580x24-bit
Weight(g)	~30	28	156-190
Articulated Skeleton	No	No	No
Resolution cubical voxels (microns)	110	100	20
Imaging Modalities	MRI	X-ray CT, PET, Cryosectioning	Cryosectioning
Processing Data software	SURFdriver, Rhinoceros NURBS	ImageJ, RVIEW, LEREG, MATLAB, BrainSuite	Photoshop, VTK
Website	http://dmip1.rad.jhmi.edu/xcat	http://neuroimage.usc.edu/Digimouse.html	http://vchibp.vicp.net/VCH/Mice/tech.html
Segmented organs			
Skeleton	√	√	√
Ribs	√		
Spine	√		
Skull	√		
Skin surface		√	√
Esophagus			√
Stomach	√	√	√
Stomach wall	√		
Stomach contents	√		
Intestines	√		√
Small and Large intestines	√		
Small and Large intestines air	√		
Liver	√	√	√
Lungs	√	√	√
Kidneys	√	√	√
Heart	√	√	√
LV, RV, LA, RA, myocardium	√		
LV, RV, LA, RV chambers (blood pool)	√		
Spleen	√	√	√
Background	√	√	√
Brain	√	√	√
Neocortical white matter	√		
Neocortical gray matter	√		
Cerebellum white matter	√		
Cerebellum gray matter	√		
Cerebellum nuclei	√		
Thalamus	√		
Hippocampus	√		
Cerebrum		√	
Cerebellum		√	
Olfactory bulbs		√	
Striatum		√	
Medulla		√	
Masseter muscles		√	
Eyes		√	
Lachrymal glands		√	
Pancreas	√	√	
Adrenal glands		√	
Testes	√	√	
Bladder	√	√	
Vas deferens	√	√	
Thyroid	√		

Table 2.4 Comparison between the three atlases. √ indicates whether a specific organ is present in one of the described atlases

References

[1].   Talairach J. and Tournoux P. *Co-planar stereotaxic atlas of the human brain: 3-dimensional proportional system - an approach to cerebral imaging* Thieme Medical Publishers; New York 1988

[2].   The visible human project, http://www.nlm.nih.gov/research/visible/visible_human.html

[3].   Segars W. P., Lalush D. S. and Tsui B. M. W. *Modeling respiratory mechanics in the MCAT and spline-based MCAT phantoms* IEEE T Nucl Sci 48(1): 89–97 2001

[4].   Zaidi H., Tsui B. M. W. *Review of Computational Anthropomorphic Anatomical and Physiological Models* P IEEE 97(12): 1938–1953 2009

[5].   Toga A. W., Santori E. M., Hazani R. *et al. A 3D digital map of rat brain* Brain Res Bull 38(1):76–85 1995

[6].   Broadwell R. D. and Bleier R. *A cytoarchitectonic atlas of the mouse hypothalamus* J Comp Neurol 167(3): 315–339 1976

[7].   Celio M. R., Hof P. R., Bloom F. E. *et al. A computerized stereotaxic atlas of the mouse brain* Soc Neurosci Abst 24: 1065–1065 1998

[8].   MacKenzie-Graham A., Lee E. F., Dinov I. *et al. A multimodal, multidimensional atlas of the c57bl/ 6j mouse brain* J Anat 204: 93–102 2004

[9].   Rosen G. D., Williams A. G., Capra J. A. *et al. The mouse brain library* Int Mouse Genome Conference 14: 166 2000

[10].   Thompson P. M., Mega M. S., Narr K. L. *et al. Brain Image Analysis and Atlas Construction* In: Sonka M. and Fitzpatrick J. M., eds. Medical image processing and analysis. Academic Press; chapter 17: 1063–1119 2000

[11].   Brune R. M., Bard J. B. L., Dubreuil C. *et al. A three-dimensional model of the mouse at embryonic day 9* Dev Biol 216: 457–468 1999

[12].   Dhenain M., Ruffins S. W. and Jacobs R. E. *Three-dimensional digital mouse atlas using high-resolution MRI* Division of Biology 232: 458–470 2001

[13].   Santi P. A. and Nietfeld J. *Development of a mouse cochlea database* ARO Session K4 Inner Ear Anatomy 2 Abst 376 2002

[14].   Segars W. P., Tsui B. M. W., Frey E. C. *et al. Development of a 4D digital mouse phantom for molecular imaging research* Mol Imag Biol 6(3): 149–159 2004

[15].   Dogdas B., Stout D., Chatziioannou A. *et al. Digimouse: a 3D whole body mouse atlas from CT and cryosection data* Phys Med Biol 52(3): 577–587 2007

[16].   Bai X., Yu L., Liu Q. *et al. A high resolution anatomical rat atlas* J Anat 209(5): 707–708 2006

[17]. Wu L., Zhang G., Luo Q. *et al. An image-based rat model for Monte Carlo organ dose calculations* Med Phys 35(8): 3759–3764 2008

[18]. Amira, http://www.amiravis.com

[19]. Cook M. J. *Anatomy of the Laboratory Mouse* Academic Press 1965

[20]. Bab I., Hajbi-Yonissi C., Gabet Y. *et al. Micro-tomographic atlas of the mouse skeleton* Springer 2007

[21]. Baiker M., Milles J., Dijkstra J. *et al. Atlas-based whole-body segmentation of mice from low-contrast micro-CT data* Med Image Anal 14(6): 723–737 2010

[22]. Martini F. H., Timmons M. J., Tallitsch R. B. *et al. Human Anatomy,* Pearson Education-Benjamin Cummings, Fifth Edition, ISBN-0-321-31204-X 2006

[23]. Li X., Yankeelov T. E., Peterson T. E. *et al. Automatic nonrigid registration of whole body CT mice images* Med Phys 35(4): 1507–20 2008

[24]. Somayajula S., Joshi A. A. and Leahy, R. M. *Mutual information based non-rigid mouse registration using a scale-space approach* Proc IEEE Intl Symp on Biomedical Imaging 1147–1150 2008

[25]. Besl P. J. and McKay N. D. *A method for registration of 3D shapes* IEEE T Pattern Anal 14: 239–256 1992

[26]. Maintz J. B. A. and Viergever M. A. *A survey of medical image registration* Med Image Anal 2: 1–36 1998

[27]. Zitova B. and Flusser J. *Image registration methods: a survey* Image Vision Comput 21: 977–1000 2003

[28]. Bookstein F. L. *Principal warps - Thin-Plate Splines and the decomposition of deformations* IEEE T Pattern Anal 11: 567–585 1989

[29]. Dice L. *Measures of the amount of ecologic association between species* Ecology 297–302 1945

[30]. Zijdenbos A. P., Dawant B. M. and Margolin R. A. *Morphometric analysis of white-matter lesions in MR-images - method and validation* IEEE T Med Imaging 13: 716–724 1994

[31]. Kaijzel E. L., van der Pluijm G. and Löwik C. W. G. M. *Whole-body optical imaging in animal models to assess cancer development and progression* Clin Cancer Res. 13(12): 3490–3497 2007

[32]. Kaijzel E. L., Snoeks T. J. A., Buijs J. T. *et al. Multimodal imaging and treatment of bone metastasis* Clin Exp Metastasis 26(4): 371–379 2007

[33]. Wildeman M. H., Baiker M., Reiber J. H. C. *et al. 2D/3D registration of micro-CT data to multi-view photographs based on a 3D distance map* Proc IEEE Intl Symp Biomed Imaging 987–990 2009

[34]. Kok P., Dijkstra J., Botha C. P. *et al. Integrated visualization of multi-angle bioluminescence imaging and micro CT* Proc SPIE Medical Imaging 6509: 1–10 2007

[35]. Khmelinskii A., Baiker M., Chen X. J. *et al. Atlas-based organ & bone approximation for ex-vivo µMRI mouse data: a pilot study* IEEE Intl Symp on Biomedical Imaging 1197–1200 2010

[36]. Zhou Y. Q., Davidson L., Henkelman R. M. *et al. Ultrasound-guided left-ventricular catheterization: a novel method of whole mouse perfusion for microimaging* Lab Invest 84(3): 385–389 2004

[37]. Chaudhari A. J., Joshi A. A., Darvas F. *et al. A method for atlas-based volumetric registration with surface constraints for optical bioluminescence tomography in small animal imaging* Proc SPIE Medical Imaging 6510 Part 2: 651024 2007

[38]. Baiker M., Dijkstra J., Que I. *et al. Organ approximation in µCT data with low soft tissue contrast using an articulated whole-body atlas* Proc IEEE Intl Symp on Biomedical Imaging 1267–1270 2008

[39]. Joshi A. A., Chaudhari A. J., Shattuck D. W. *et al. Posture Matching and Elastic Registration of a Mouse Atlas to Surface Topography Range Data* Proc IEEE Intl Symp on Biomedical Imaging 366–369 2009

[40]. Li X., Yankeelov T. E., Peterson T. E. *et al. Constrained non-rigid registration for whole body image registration: method and validation* Proc SPIE Medical Imaging 6512: 651202-1–651202-8 2007

[41]. Landis J. R. and Koch G. G. *The measurement of observer agreement for categorical data* Biometrics 33(1): 159–174 1977

[42]. Bartko J. J. *Measurement and reliability: statistical thinking considerations* Schizophrenia Bulletin 17(3): 483–489 1991

[43]. Alexandrakis G., Rannou F. R. and Chatziioannou A. F. *Tomographic bioluminescence imaging by use of a combined optical-PET (OPET) system: a computer simulation feasibility study* Phys Med Biol 50(17): 4225–4241 2005

2

Chapter 3

Segmentation and visual analysis of whole-body mouse skeleton μSPECT

Abstract

Whole-body SPECT small animal imaging is used to study cancer, and plays an important role in the development of new drugs. Comparing and exploring whole-body datasets can be a difficult and time-consuming task due to the inherent heterogeneity of the data (high volume/throughput, multi-modality, postural and positioning variability). The goal of this study was to provide a method to align and compare side-by-side multiple whole-body skeleton SPECT datasets in a common reference, thus eliminating acquisition variability that exists between the subjects in cross-sectional and multi-modal studies. Six whole-body SPECT/CT datasets of *BALB/c* mice injected with bone targeting tracers ^{99m}Tc-methylene diphosphonate (^{99m}Tc-MDP) and ^{99m}Tc-hydroxymethane diphosphonate (^{99m}Tc-HDP) were used to evaluate the proposed method. An articulated version of the MOBY whole-body mouse atlas was used as a common reference. Its individual bones were registered one-by-one to the skeleton extracted from the acquired SPECT data following an anatomical hierarchical tree. Sequential registration was used while constraining the local DoFs of each bone in accordance to the type of joint and its range of motion. The APR algorithm was applied to the segmented data for side-by-side change visualization and comparison of data. To quantitatively evaluate the proposed algorithm, bone segmentations of extracted skeletons from the correspondent CT datasets were used. Euclidean point to surface distances between each dataset and the MOBY atlas were calculated. The obtained results indicate that after registration, the mean Euclidean distance decreased from 11.5 ± 12.1 to 2.6 ± 2.1 voxels. The proposed approach yielded satisfactory segmentation results with minimal user intervention. It proved to be robust for "incomplete" data (large chunks of skeleton missing) and for an intuitive exploration and comparison of multi-modal SPECT/CT cross-sectional mouse data.

3.1   Introduction

Whole-body small animal imaging is widely used for the *in vivo* visualization of functional and anatomical information to study cancer, and for evaluation of drugs in pre-clinical research. An efficient combination of functional and structural information enables the visualization of cellular function and the follow-up of molecular processes in the living animals in their anatomical context. Functional information is provided by modalities such as PET, SPECT, MRI and Optical Imaging (OI), while anatomical information is usually obtained using CT and ultrasound.

The data heterogeneity and volume created by whole-body multimodality imaging presents a complex problem with respect to combining, analyzing and quantifying this data with low inter-observer and intra-observer variability and minimal human input. This is caused in part by a high degree of shape and postural variability present in follow-up and cross-sectional animal studies. This variability is due to the fact that an animal body is a highly deformable system with many rigid parts (bones) and non-rigid structures (organs) [1, 2]. Also, there are no standardized protocols for animal positioning: if a subject is imaged using different imaging modalities and protocols during follow-up studies or if different animals are used,

36

the subject is positioned in different ways and postural variations occur (*e.g.,* of the head, back and front limbs, *etc.*). One way to cope with this variability is to use multimodal animal holders between different scanners or use combined SPECT/CT, PET/CT, PET/MRI, or PET/SPECT/CT scanners that are becoming increasingly available. However, multimodal holders are not widely used or compatible and when they are, there are still significant differences in animal posture between different time points [3].

Various approaches were proposed to handle heterogeneous multi-modality data: Joshi *et al.* [4] proposed a method for fitting an elastically deformable mouse atlas to surface topographic range data acquired by an optical system; this method does not incorporate the extremities. Savinaud *et al.* [5] proposed a novel model-based approach to track animals in 3D from monocular video which allows the quantification of bioluminescence (BLI) signal on freely moving animals. Wildeman *et al.* [6] proposed a 2D/3D registration of μCT data to multiview photographs based on a 3D distance map combining optical/ BLI data with CT. Suh *et al.* [7] published a serial registration method to serial μCT/SPECT mouse lower extremities images.

In [2, 3], the authors suggested the use of articulated whole-body small animal atlases as a standard geometric reference to tackle the problem of segmenting and organizing heterogeneous whole-body multi-modality small animal data. Using the articulated whole-body MOBY atlas, Baiker *et al.* presented a fully-automated skeleton registration and organ approximation method in low-contrast μCT mouse data [1]. This method exploits the high contrast of bone to automate the registration process of the skeleton model and the subsequent organ approximation. However, performing an anatomical CT scan together with a functional one is not always desired in longer term follow-up studies, where prolonged radiation exposure may become a confounding factor in cancer research, or may cause adverse radiation effects [8].

The goal of this study is to provide a segmentation and exploration tool for whole-body skeleton SPECT mouse data that eliminates any postural variability between the study subjects with minimal user intervention. Whole-body skeletal SPECT imaging with bone targeting tracers is of great interest for arthritis studies [9], development of bone pain palliation agents [10] as well in the field of bone metastases imaging in animal models. Since the location of metastatic appearance is unknown, whole-body scans, including follow-up, are essential to assess the growth and/or metastatic response to treatment [11]. This is a challenging task due to the nature of whole-body skeleton SPECT data: usually noisy, due to the relative short acquisition time and low resolution with an incomplete skeleton image (several portions missing in limbs, skull, *etc.*).

The main technical contributions of this paper are twofold:

(i) we present a semi-automated atlas-based skeleton segmentation method for whole-body SPECT mouse data that requires minimal user input

(ii) using the Articulated Planar Reformation (APR) algorithm [12, 13], we provide the user with an intuitive side-by-side comparison and exploration platform for multi-modal (SPECT/CT), cross-sectional and follow-up data in a standardized layout, independent on the position of the animal during acquisition
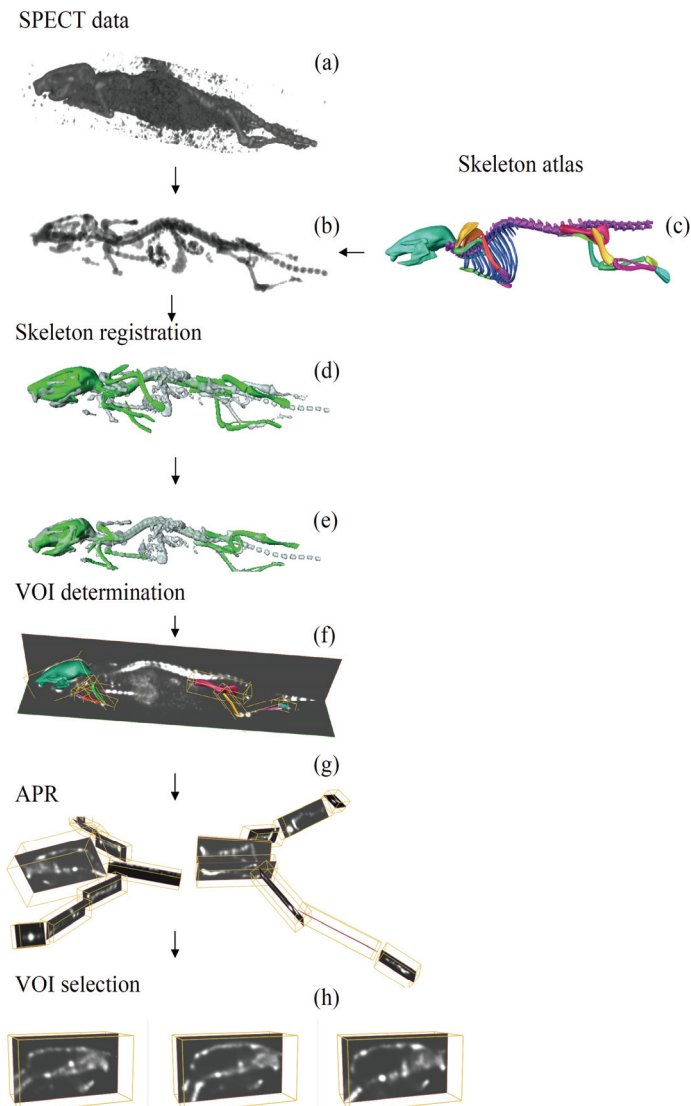
Figure 3.1 Overview of the proposed segmentation method: given a SPECT dataset (a), the skeleton is extracted from the SPECT dataset (b). Next, the atlas skeleton (c) and the extracted skeleton (b) are registered to each other (d, e) using an anatomically realistic kinematic model. After the registration, the segmented data is reformatted into segments corresponding to the mouse atlas and thus mapping the data to a standardized atlas space (f, g). The data is now ready for an easy, fast and intuitive side-by-side exploration (multi-modal, follow-up or cross-sectional data) (h)

3.2 Materials and methods

3.2.1 Method overview

The first step of the proposed approach is to extract the skeleton from the SPECT data. Subsequently, the articulated mouse atlas is registered to the data following a hierarchical anatomical tree: first, the atlas is coarsely registered to the entire skeleton. Then, starting with the skull, each atlas bone is accurately registered to the correspondent bone in the data using the Iterative Closest Point (ICP) approach [14]. After the atlas is registered to the data, we apply the APR algorithm [12, 13] to reformat the segmented data into segments corresponding to a mouse atlas and thus mapping the data to a standardized atlas space. The presented method is validated using 6 *BALB/c* mice, and the quantitative performance of the method is assessed calculating the Euclidian point to surface distance between the atlas and the correspondent μCT skeleton surface. The results are compared to the results present in the literature for low-contrast μCT whole-body mouse data [1]. For a visual overview of the proposed method see Figure 3.1.

3.2.2 Articulated MOBY atlas

A realistic 4D digital mouse phantom was generated by Segars *et al.* [15] based on high-resolution 3D MRI data of a *C57BL/6*, 15 week old mouse from Duke University. The skeleton in this atlas did not distinguish between single bones and joints. To allow the registration to perform independent of the data acquisition protocol and large postural variations due to postural heterogeneity between scans, we presented a segmentation of the skeleton into individual bones and added anatomically realistic kinematic constraints and DoFs to each joint in [1, 3, 16]. Using the Amira™ V3.1 software [17] and guided by anatomical text books [18, 19] the following bones/bone groups were labeled: *scapulae, humeri* (upper front limbs), *ulnae/radii* (lower front limbs), *manus* (front paws), *femora* (upper hind limbs), *tibiae/fibulae* (lower hind limbs), *pedes* (hind paws), *caput* (skull), *columna vertebralis* (spine), *costae* (ribs), *sternum* (chest bone), and *pelves*. Each joint position was identified and the corresponding DoFs and kinematic constraints were specified. Two types of joints were distinguished: ball joints and hinge joints. The resulting articulated version of the MOBY skeleton can be seen in Figure 3.2.
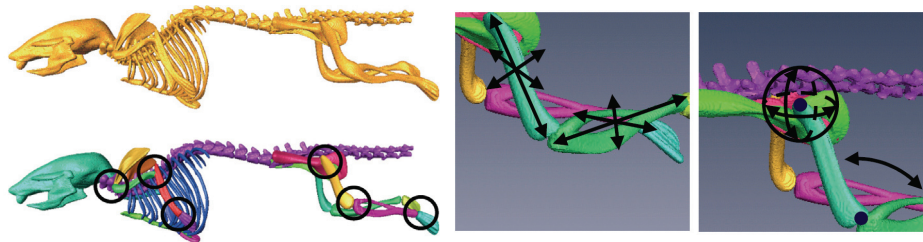
Figure 3.2 The MOBY mouse atlas skeleton: as originally included in the atlas (top left), after segmenting the individual bones (bottom left), and a detail of the kinematic constraints and the DoFs of the femur/tibia-fibula bone complex (right). The colors indicate the different labels of each bone

3.2.3 Whole-body SPECT/CT mouse data acquisition

In this study, we aim to demonstrate the robustness of the atlas-based segmentation with respect to the different whole-body SPECT scan settings and high posture variability that exists between those scans. Therefore, six male, *BALB/c* mice were retrospectively collected from several different imaging studies to represent that variability. One half was intravenously injected with 50 ± 6 MBq ^{99m}Tc-MDP, and the other one with 50 ± 6 MBq ^{99m}Tc-HDP. All mice were scanned 4 hours later using the Bioscan NanoSPECT/CT™ device (Washington DC, USA), equipped with four gamma cameras and pinhole apertures. With the combined scanner, the SPECT and CT were acquired one after the other without movement of the animal, so both imaging modalities are registered by hardware calibration. SPECT images were reconstructed using the ordered subset expectation maximization (OSEM) and CT images using the filtered back projection (FBP) algorithms. ^{99m}Tc-MDP and ^{99m}Tc-HDP are gamma-emitting radionuclide substances, where the metastable technetium (^{99m}Tc) is tagged onto a phosphonate compound (MDP, HDP) to generate ^{99m}Tc-MDP and ^{99m}Tc-HDP respectively, which selectively concentrate in the bone and are the primary imaging agents used to image changes in bone vascularity and osteoblastic activity [20]. Both tracers are used in translational research. For all mice, part of the tracer is cleared by the liver and as such, this organ is visible as well. Between these six datasets, the resolution of the scanner varies, ranging from SPECT voxel size of 0.60 x 0.60 x 0.60 mm^3 to 0.20 x 0.20 x 0.20 mm^3. The highest resolution CT dataset has a voxel size of 0.10 x 0.10 x 0.10 mm^3 and the lowest 0.99 x 0.99 x 1.00 mm^3 (see Table 3.1 for further detail). All procedures involving animals were approved by the Animal Experimental Committee (DEC) of the Erasmus MC and performed in agreement with The Netherlands Experiments on Animals Act (1977) and the European Convention for Protection of Vertebrate Animals Used for Experimental Purposes (Strasbourg, 18 March 1986).

	SPECT	CT
	Resolution (voxel size in mm^3)	
Mouse 1	0.60 x 0.60 x 0.60	0.80 x 0.80 x 0.80
Mouse 2	0.30 x 0.30 x 0.30	0.99 x 0.99 x 1.00
Mouse 3	0.30 x 0.30 x 0.30	0.20 x 0.20 x 0.20
Mouse 4	0.30 x 0.30 x 0.30	0.10 x 0.10 x 0.10
Mouse 5	0.20 x 0.20 x 0.20	0.20 x 0.20 x 0.20
Mouse 6	0.20 x 0.20 x 0.20	0.10 x 0.10 x 0.10

Table 3.1 Resolution of each SPECT and correspondent CT dataset

The SPECT datasets were used for testing the proposed approach, and the correspondent µCT datasets to quantitatively validate the performance of the method.

3.2.4 SPECT/CT data pre-processing

To reduce the noise, small objects and other artifacts present in the SPECT data, in the first step of the algorithm, a threshold combined with a connected components filtering and morphological operations (erosion and dilation) was applied to the SPECT data to estimate the skeleton. Due to the variation of the tracer distribution,

the extraction of the best possible skeleton requires minimal user input to adjust the threshold and morphological operators parameter settings (more specifically in the extraction of the spine centerline step, see section below). This results in a coarse estimation of the major accumulations of the radioactive tracer: bladder, kidneys, part of the liver and the skeleton. In Figure 3.3, one can see that due to the differences in nature between the SPECT and CT data, the resultant skeleton in the case of the SPECT data is incomplete, with several parts missing (especially the front limbs, hind limbs and the skull, which is incomplete with large holes). For the CT datasets on the other hand a simple threshold returns the full, complete skeleton (Figure 3.3).
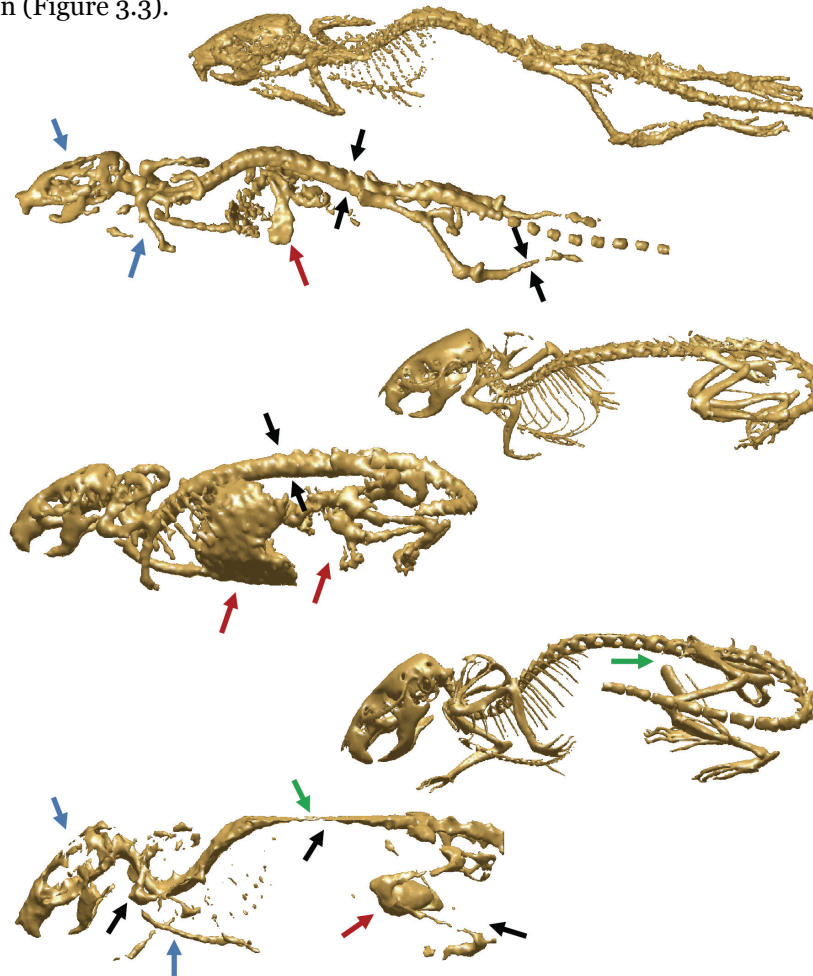
Figure 3.3 Examples of SPECT skeleton isosurfaces with the corresponding CT skeleton isosurfaces after the pre-processing step. The figure shows the positioning differences of the mouse in the scanner, SPECT (left) and the correspondent CT (right). The SPECT skeletons are incomplete, with several parts missing: especially in the case of front, hind limbs and the skull with large holes (blue arrows); also remnants of non-relevant objects such as lungs, kidneys and bladder are present (red arrows). In the bottom dataset the right femur and part of the spine are missing (green arrows) due to incomplete acquisition. The CT skeletons are complete and clean after the pre-processing step and are used in the validation of the proposed approach to calculate the Euclidean point to surface distance between the registered atlas and the skeleton surface. Black arrows indicate examples of regions where over and underestimation of the bone thickness occurred during the skeleton estimation in the data pre-processing step

3.2.5 Articulated atlas-based SPECT skeleton data segmentation

In this step the articulated MOBY atlas is fitted to the skeleton extracted from the SPECT data. For this purpose a modified version of the fully automated approach presented in [1] was used. To deal with the large articulations between bones and/or bone groups, the registration of the atlas is employed following a hierarchical model tree (see Figure 3.4). It is initialized with a coarse alignment of the atlas and the entire target SPECT skeleton, where a similarity transformation model is applied to accommodate for the animal pose in the scanner and for size differences between animals (7 DoFs are taken into account: three for translation, three for rotation and one for isotropic scaling). After the coarse alignment of the entire skeleton, the individual bones are registered stepwise using the ICP algorithm [14], which is a method for point-based registration (skeleton surfaces in this case). We start at the skull, then, if necessary, the user locates the spine location where the vertebra connects the spine to the pelvis, the spinal centerline is extracted using three dimensional region growing until the pelvis is reached and registered and finally proceed to the back limbs, sternum and front limbs separately. The transformation models for the individual bones are dependent on the joint type (ball or hinge) and for each type a realistic motion model was defined ensuring that the bones remain in anatomically realistic shapes. See [1] for more details.
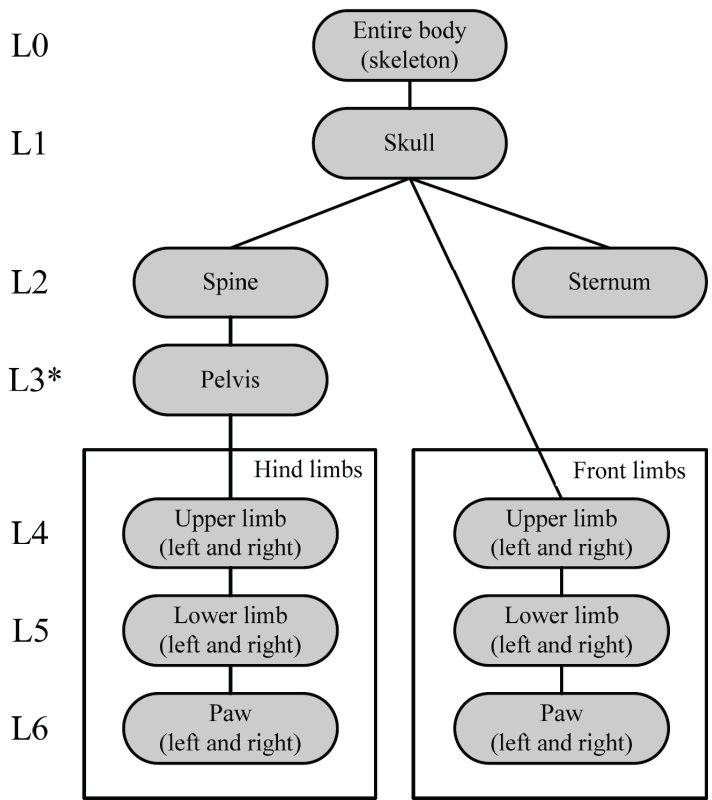
Figure 3.4 Hierarchical anatomical tree followed during the registration process. * indicates where user input is necessary: to pin-point the spine location where the vertebra connects the spine to the pelvis

3.2.6 APR of combined SPECT/CT mouse data

The fitted atlas yields a completely segmented SPECT skeleton where each bone has its own unique label. In this step we use the Articulated Planar Reformation (APR) algorithm [12, 13], that uses the segmented bones and the correspondent transformation models to reformat the data into segments corresponding to the atlas and thus maps the data to a standardized atlas space.

For each bone in the atlas, based on the surface representation of the bone and the corresponding linear transform that was determined during registration a bounding box is automatically determined. Using the bounding box, the volume SPECT data is resampled for each bone with the aim of obtaining the volume in a standard coordinate frame, which facilitates comparison (Figures 3.1(f, g)).

The result is a visualization that consists of a global whole-body view at the top, with a number of focus views of longitudinal, cross-sectional or multimodal data side-by-side at the bottom (Figure 3.1(h) and Figure 3.5). This standardized layout facilitates the comparison between subjects, eliminating large differences in animal posture. It allows the user to quickly identify regions/volumes of interest in the global whole-body view and then study the differences or changes in synchronized local per-segment focus views.

3.2.7 Quantitative evaluation indices

To quantitatively validate the registration accuracy and enable comparison with the registration error achieved in μCT data as reported in [1], we used the same error metric to evaluate the SPECT segmentation: the mean Euclidean point to surface distance in voxels, *i.e.,* the shortest distance between objects in space. For each SPECT dataset, we calculated this distance between the registered MOBY atlas skeleton and the correspondent co-registered CT skeleton, before (*i.e.:* after the coarse alignment) and after articulated registration. The results were compared to the mean Euclidean point to surface distance published in [1] for μCT.

To investigate quantitatively intrinsic differences between SPECT and CT (Figure 3.3), we calculated the mean Euclidean point to surface distance between the estimated SPECT and its correspondent CT skeletons (Table 3.2).

	Mean Euclidian point to surface distance between the SPECT and correspondent CT skeletons and standard deviation (in voxels)
Mouse 1	6.4 ± 11.1
Mouse 2	5.9 ± 7.9
Mouse 3	4.5 ± 5.7
Mouse 4	2.7 ± 4.1
Mouse 5	9.6 ± 13.4
Mouse 6	7.7 ± 8.1
Mean	6.1 ± 8.4

Table 3.2 Mean Euclidian point to surface distance between the SPECT and CT skeletons after the pre-processing step
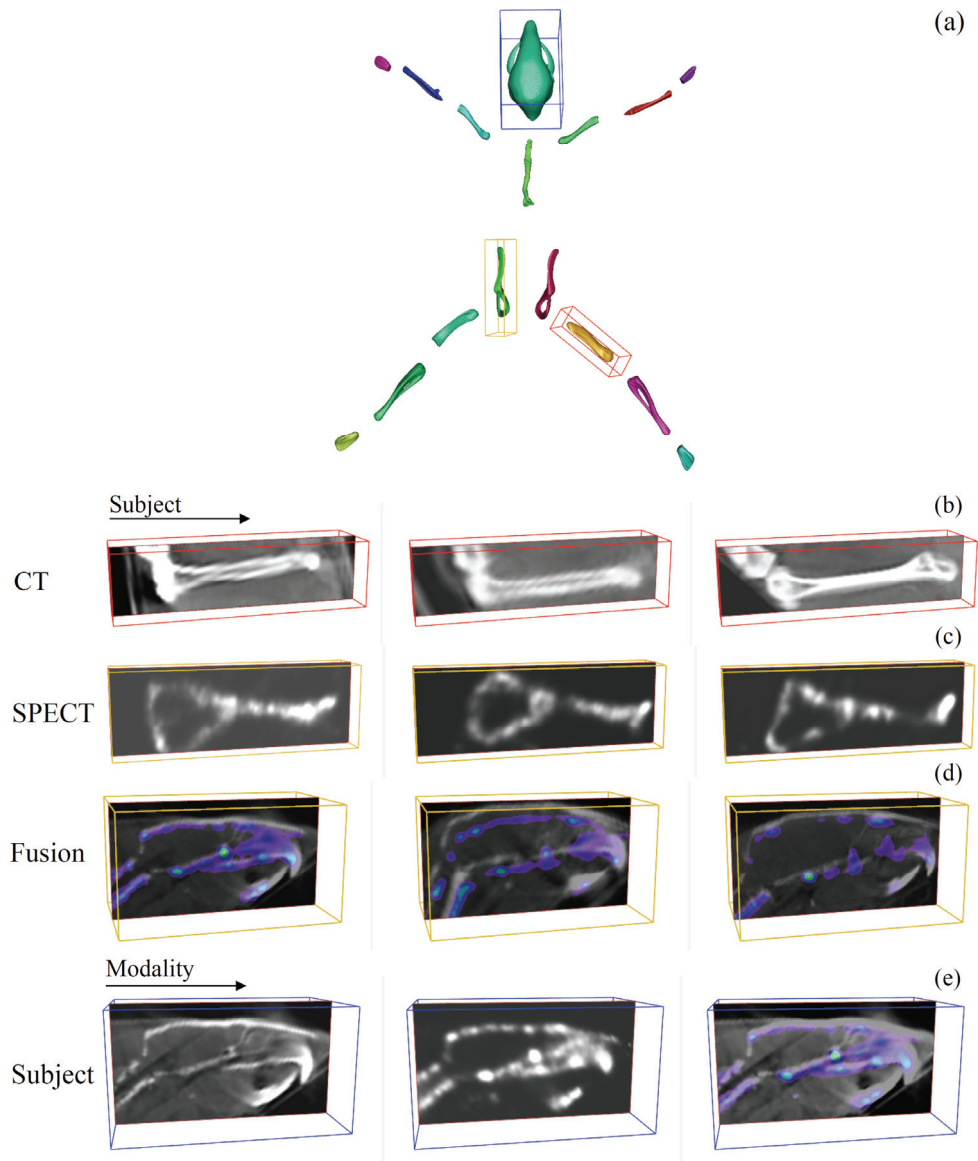
Figure 3.5 APR layout of the segmented mouse data. (a)—global articulated planar reformatted visualization of the atlas. (b), (c), (d) and (e) show the different data visualization options after applying the proposed approach. One can choose to visualize simultaneously and side-by-side a particular region of interest in cross-sectional studies for CT, SPECT or the combination of both. (b)—side-by-side visualization of the CT femur bone of 3 subjects, (c)—side-by-side visualization of the SPECT pelvic bone of 3 subjects, (d)—side-by-side visualization of the CT skull data fused with the correspondent SPECT data for 3 subjects, (e)—side-by-side visualization of the skull data of one particular subject: CT, SPECT and a combination of both. Follow-up data visualization was demonstrated in [10] for longitudinal CT mouse data

44

3.3 Results

Table 3.3 presents the Euclidian point to surface distance before and after articulated registration for all the subjects. For all the mice, after the registration the Euclidean point to surface distance between the MOBY atlas and the SPECT skeleton decreased: the calculated mean of the distance decreased from 11.5 ± 12.1 to 2.6 ± 2.1 voxels. In case of mouse 4 (Figure 3.3, bottom mouse), the Euclidean point to surface distance before registration is higher than for the other subjects for two reasons. The first reason is the positioning of the mouse in the scanner: the hind and front limbs were pulled towards the belly resulting in a lower alignment/overlay between the atlas and the data surfaces during the coarse alignment. The second reason is the fact that the SPECT skeleton after the pre-processing step in case of mouse 4 is underestimated (only remains of the limbs are visible, and a very small portion of the skull and the spine are present). Since the amount of total bone content of the skeleton has an influence on the coarse alignment step [1], in this case, during the coarse alignment, the atlas successfully accommodates for the animal position (prone/supine) and orientation of the animal, but the main overlap between the atlas and the animal after this coarse step happens between the skulls. Figure 3.3 shows three data examples with variations in posture with which the proposed method successfully coped. An example of a segmented SPECT dataset is presented in Figure 3.6.

	Mean Euclidian point to surface distance and standard deviation (in voxels)	
	Before registration	After registration
Mouse 1	10.3 ± 10.1	2.4 ± 2.4
Mouse 2	6.6 ± 7.8	2.5 ± 2.1
Mouse 3	8.2 ± 8.2	2.0 ± 1.7
Mouse 4	25.8 ± 32.1	3.3 ± 2.8
Mouse 5	10.4 ± 8.7	2.6 ± 1.9
Mouse 6	7.5 ± 5.9	2.9 ± 2.0
Mean	11.5 ± 12.1	2.6 ± 2.1
Baiker *et al.* [1] (µCT)	8.8 ± 1.9	1.8 ± 0.1

Table 3.3 Quantitative results of the MOBY atlas-to-skeleton registration for 6 mouse SPECT datasets and [1]

After applying the APR algorithm to both µCT and SPECT data, one can use a range of visualization techniques that enable exploration of both datasets, the result of which is depicted in Figure 3.5. The articulated layout visualization is shown, where all segments of the atlas have been spread out into a plane—Figure 3.5(a). In Figure 3.5 the different visualization options are generated using the proposed approach. The femur, pelvis and skull were selected and are shown in the correspondent focus views. All focus views show an outline and an image slice visualization and one can visualize CT, SPECT, or a combination of both (where the SPECT data is shown as an overlay with a color map applied to it) in either cross-sectional analysis—Figures 3.5(b, c, d) or for multi-modality complementarity—Figure 3.5(e).

The entire articulated registration process was implemented in MATLAB R2008b™ and took approximately 2 minutes of runtime (including minimal user interventions to assist the spine centerline extraction) on a standard desktop PC (2.40GHz Intel Quad Core™ with 3GB of RAM, Windows™).

3.4   Discussion and conclusion

In vivo visualization of functional and anatomical information produces heterogeneous, high throughput data. Efficiently combining, analyzing and quantifying whole-body small animal cross-sectional, longitudinal and multi-modal data is a complex problem. In this paper, we demonstrated the feasibility of the articulated atlas-based skeleton segmentation approach combined with the articulated planar reformation algorithm for whole-body mouse bone imaging using SPECT.
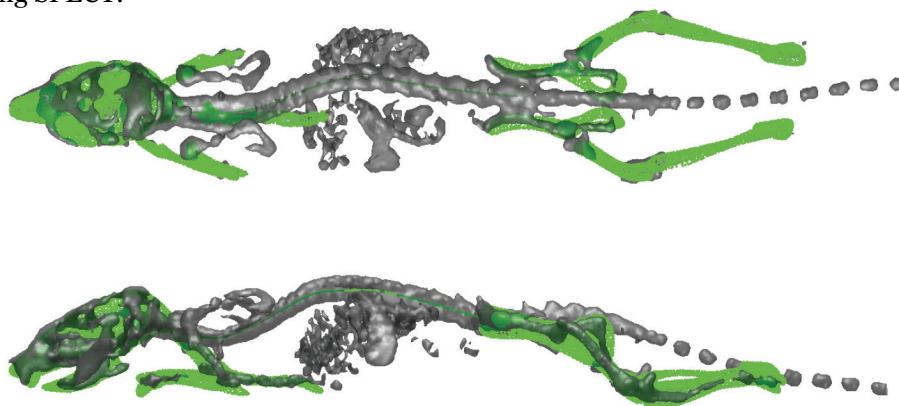
Figure 3.6 Top and side views of the segmented SPECT skeleton initially presented in Figure 3.1a). The registered MOBY atlas is represented in green

Quantitative evaluation was performed by calculating the Euclidian point to surface distance between the registered atlas and the correspondent CT dataset. The obtained mean distance of 2.6 ± 2.2 voxels, showed that the registration accuracy for the SPECT data is of the same order as the previously published results for μCT, 1.8 ± 0.1 voxels [1]. The large difference in the standard deviation between the μCT fittings results and the ones presented in this paper might be due to the variable nature of the SPECT data (tracer uptake and distribution, where the tracer targets the bone growth and not the entire bone and partial volume effect) versus the more robust bone contrast in CT. Due to these factors the pre-processing step (extraction of the skeleton out of the data while removing the noise, small objects and other artifacts) may result in either a partial or a much thinner (Figure 3.3) or thicker skeleton than as seen in the μCT. This explains the difference in distance measures between the SPECT and CT skeleton surfaces (Table 3.2). As mentioned above, by collecting data from several different imaging studies, one of the goals of this study was to demonstrate the robustness of the atlas-based segmentation with respect to the different whole-body SPECT scan settings. Depending on the research question, the amount of injected tracer, the pinhole size and scan time a trade-off has to be chosen between resolution and signal. However, as long as a skeleton estimation is possible the approach presented here holds.

In [1], it was demonstrated that the proposed atlas-based segmentation method is robust with respect to osteolytic bone defects. Here, it was demonstrated, that the use of the articulated mouse atlas, with defined DoFs and size restrictions for each bone, proved to be robust for "incomplete" data (*i.e.:* images where large bits of

limbs are missing), like exemplified in Figures 3.3 (bottom mouse) and 6. If a lower or an upper part of a limb is completely missing, than the proposed approach will only segment the part that is present in the dataset, *i.e.,* the part where there was significant/enough tracer uptake.

It also proved to be relatively insensitive to non-relevant objects still present in the image after threshold-based segmentation, like kidneys, bladder, some lung and liver. The proposed approach effectively compensated for the large variations in posture that existed within the data and yielded segmentation results requiring minimal user input. These were of satisfactory quality for the ensuing mapping of the data to the standard reference and side-by-side visualization. Applying the APR algorithm to multi-modal cross-sectional data proved to be useful to provide proper referencing and visualization for an intuitive exploration and comparison of µCT, SPECT data (Figure 3.5). The authors are currently working on further extending the approach presented here to combine automatic segmentation of the different bones with tracer quantification.

The segmentation approach presented here was developed to cope with a scenario when a combined whole-body SPECT/CT bone scan is not always desired or available. Thus, one of the limitations of the proposed approach is the fact that the skeleton should exhibit sufficient image contrast, *i.e.,* direct application of the atlas fitting to SPECT data requires tracer uptake in the skeleton. When that is not the case, the limitation can be overcome by applying the fitting directly to the provided whole-body anatomical CT scan and then propagating it to the SPECT data. Furthermore, though very minimal, this method requires user input during the extraction of the possible skeleton out of the data. This only stands true when the method is applied to SPECT directly and correspondent CT data is not available. When CT whole-body data is available, due to its robust and consistent nature, this kind of user input is not required anymore, as shown and extensively validated in [1].

An articulated atlas-base skeleton segmentation method for SPECT whole-body small animal data was presented. The evaluation of the method demonstrated it to be sufficiently accurate and robust for intuitive exploration of whole-body, cross-sectional multi-modal small animal imaging data. The approach presented here can be applied to other animals, provided there is an adequate atlas.

References

[1].   Baiker M., Milles J., Dijkstra J. *et al. Atlas-based whole-body segmentation of mice from low-contrast micro-CT data* Med Image Anal 14(6): 723–737 2010

[2].   Khmelinskii A., Baiker M., Kok P. *et al. Atlas-based articulated skeleton segmentation of µSPECT mouse data* Proc IEEE Intl Symp Biomed Imaging 437–440 2011

[3].   Khmelinskii A., Baiker M., Chen X. J. *et al. Articulated whole-body atlases for small animal image analysis: construction and applications* Mol Imaging Biol 13(5): 898–910 2011

[4]. Joshi A. A., Chaudhari A. J., Li C. *et al. Posture matching and elastic registration of a mouse atlas to surface topography range data* Proc IEEE Intl Symp Biomed Imaging 366–269 2009

[5]. Savinaud M., de La Gorce M., Maitrejean S. *et al. Model-based multi-view fusion of cinematic flow and optical imaging* Med Image Comput Comput Assist Interv 13(Pt2): 668–675 2010

[6]. Wildeman M. H., Baiker M., Reiber J. H. C. *et al. 2D/3D registration of micro-CT data to multi-view photographs based on a 3D distance map* Proc IEEE Intl Symp Biomed Imaging 987–990 2009

[7]. Suh J. W., Scheinost D., Dione D. P. *et al. A non-rigid registration method for serial lower extremity hybrid SPECT/CT imaging* Med Image Anal 15(1): 96–111 2011

[8]. Hindorf C., Rodrigues J., Boutaleb S. *et al. Total absorbed dose to a mouse during microPET/CT imaging* Eur J Nucl Med Mol Imaging 37: S274 2010

[9]. Ostendorf B., Scherer A., Wirrwar A. *et al. High-resolution multipinhole single-photon-emission computed tomography in experimental and human arthritis* Arthritis Rheum 54(4): 1096–104 2006

[10]. Máthé D., Balogh L., Polyák A. *et al. Multispecies animal investigation on biodistribution, pharmacokinetics and toxicity of ^{177}Lu-EDTMP, a potential bone pain palliation agent* Nucl Med Biol 37(2): 215–26 2010

[11]. Franc B. L., Acton P. D., Mari C. *et al. Small-animal SPECT and SPECT/CT: Important tools for preclinical investigation* J Nucl Med 49(10): 1651–1663 2008

[12]. Kok P., Baiker M., Hendriks E. *et al. Articulated planar reformation for change visualization in small animal imaging* IEEE T Vis Comput Gr 16(6): 1396–1404 2010

[13]. http://graphics.tudelft.nl/~pkok/CVP/

[14]. Besl P. J. and McKay N. D. *A method for registration of 3D shapes* IEEE T Pattern Anal 14(2): 239–256 1992

[15]. Segars W. P., Tsui B. M. W., Frey E. C. *et al. Development of a 4-D digital mouse phantom for molecular imaging research* Mol Imaging Biol 6(3): 149–159 2004

[16]. http://www.lkeb.nl

[17]. http://www.amira.com

[18]. Bab I., Hajbi-Yonissi C., Gabet Y. *et al. Micro-Tomographic Atlas of the Mouse Skeleton* Springer 2007

[19]. Cook M. J. *Anatomy of the laboratory mouse* New York, Academic 1965

[20]. MICAD - Molecular Imaging Probes and Contrast Agents Dataset
http://www.ncbi.nlm.nih.gov/books/NBK24575/

Chapter 4

Atlas-based organ & bone approximation for *ex-vivo* µMRI mouse data

Abstract

In this paper we propose a novel semi-automated atlas-based approach for organ and bone approximation for μMRI data of mice. Based on a set of 18 manually indicated landmarks at specific joint & bone locations, individual atlas bones (pelvis, limb bones and sternum) are mapped to the target in a first step and a sparse set of corresponding landmarks on a skin surface representation is determined in a second step. Subsequently, this sparse set on the skin is used to derive a dense set of correspondences relying on matching spectra of local geodesic distances. Finally, determined by the skin correspondence, a Thin-Plate-Spline (TPS) approximation of major organs (heart, lungs, liver, spleen, stomach, kidneys) is performed. The method was tested using 3 μMRI mouse datasets and the MOBY atlas. The performance of the organ approximation algorithm was estimated using manual segmentations of 6 organs for each MRI dataset and calculating Dice indices of organ-volume overlap for each dataset and the atlas. The obtained results indicate excellent fitting of heart and kidneys and moderate fitting of spleen, lungs, liver and stomach. These initial results are satisfactory and comparable to other organ mapping studies using different approaches and μCT mouse data.

4.1 Introduction

In pre-clinical research, whole-body small animal (mice and rats) imaging is widely used for the *in vivo* visualization of functional and anatomical information to study cancer, neurological and cardiovascular diseases and help with a faster development of new drugs. Structural imaging modalities such as MRI, CT and ultrasound provide detailed depictions of anatomy; PET, SPECT, and specialized MRI protocols add functional information. In addition, optical imaging modalities, such as BLI and near-infrared (NIR) microscopy offer a high sensitivity in visualizing molecular processes *in vivo*. In combination, these modalities enable the visualization of the cellular function and the follow-up of molecular processes in living organisms without sacrificing them.

However, whole-body imaging creates a large amount of data and there is an urgent need to effectively combine, organize, analyze and quantify all this data to help look for differences between wild type and mutant mice rapidly and with minimal human intervention. This is a complicated task, since an animal body is a complex system with many rigid (bones), non-rigid (organs) structures and articulated parts [1] leading to shape and postural variability in follow-up and cross-sectional studies.

For different imaging modalities several approaches were proposed to solve this problem of fitting whole-body small animal data to a common reference. Joshi *et al.* [2] proposed a method for fitting an elastically deformable mouse atlas to surface topographic range data acquired by an optical system; this method does not incorporate the extremities. Wildeman *et al.* [3] proposed a 2D/3D registration of μCT data to multi-view photographs based on a 3D distance map combining optical data with CT. Baiker *et al.* presented a fully automated skeleton registration and organ approximation method using an articulated whole-body atlas in μCT mouse data [1]. This method exploits the high contrast of bone to automate the registration process of the skeleton model and the subsequent organ

approximation; the reason for this is the fact that optical and CT lack soft tissue contrast for most abdominal organs. In this paper, we investigate the generalization of this method towards application in µMRI data. This type of data provides greater contrast between the different soft tissues of the body, but poorer bone contrast than CT data. We present a semi-automated atlas-based bone and organ approximation method for µMRI data. 18 joint landmarks are manually determined and together with surface representations of the bones and the skin, individual atlas bones are mapped to the target based on the joint correspondences and the organs are mapped using TPS approximation as reported earlier in [1]. Given the complexity of this type of data, the work described in this paper is a first step towards a more automated whole-body atlas-based bone and organ mapping in µMRI mouse data.

The contributions of this paper are twofold:

(i)   we present a novel semi-automated organ approximation method for µMRI mouse data that considerably reduces the required user effort compared to manual segmentation

(ii) the presented method includes the limbs and provides a shape approximation of the bones in MR data. The user interaction mechanism to identify the joints is guided by anatomically realistic kinematic constraints imposed by the atlas

4.2   Materials and methods

4.2.1   MOBY atlas

In this work the MOBY mouse atlas was used as the anatomical reference (Figure 1.(a)). Using a *C57BL/6,* 15 weeks old male mouse, Segars *et al.* [4] generated a realistic 4D digital mouse phantom based on high-resolution 3D MRI data from Duke University. The organs of this atlas are represented using non-uniform rational bspline (NURBS) surfaces, which are widely used in 3D computer graphics. For bone approximation we used an articulated version of the MOBY skeleton [1], where all major bones or bone compounds like the paws were separately labeled and joint locations and types were defined. See Figure 4.1.(b).

(a)   (b)
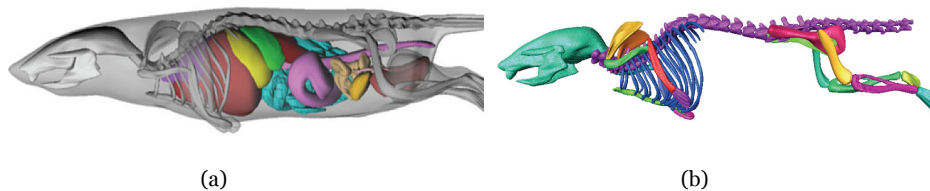
Figure 4.1 MOBY mouse atlas: (a)—Original skeleton + organs + skin. (b)—Articulated skeleton

4.2.2 μMRI data acquisition and manual organ segmentation for evaluation

Sixteen *C3H* mice were perfusion fixed with formalin and 10 mM Magnevist with ultrasound guidance [5]. Imaging was performed on a 7–T magnet with a four-channel VarianINOVA™ console (Varian Inc., Palo Alto, CA) multiplexed to 16 coils for parallel imaging. A spin echo sequence was used: TR/TE = 650/15ms and (100 μm)^3 voxels with an imaging time of 13h[1]. In this work a subset of 3 mice was used.

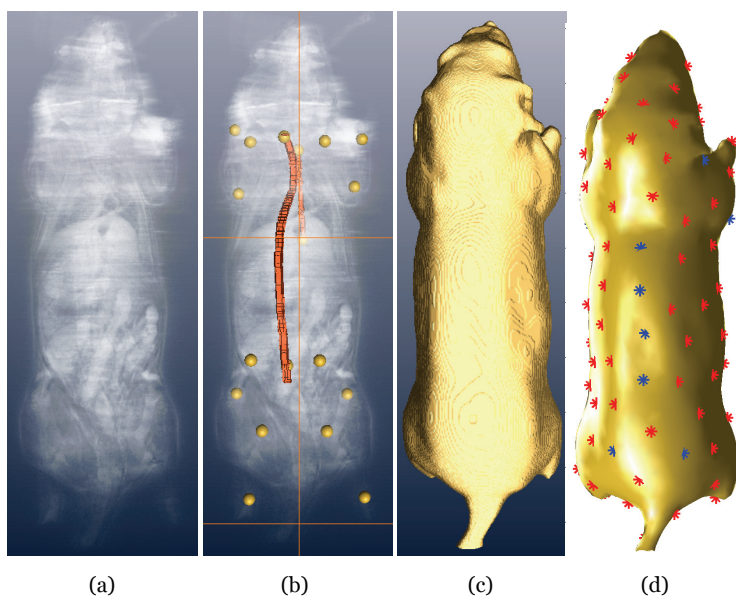To validate and evaluate the performance of the method presented in this paper, six organs (liver, heart, kidneys, lungs, stomach and spleen) were manually segmented by an expert in all three mice using the Amira™ software [6].

(a)   (b)   (c)   (d)

Figure 4.2 Landmark extraction: (a)—Original data. (b)—Manual landmarks: 2 knee joints, 2 hip joints, posterior and anterior extremities of the *sternum*, middle of the atlas vertebra, middle of the last *lumbar vertebra* and the correspondent inner surface of the *columna vertebralis*, 2 elbow joints, 2 shoulder joints, 2 ankle joints, 2 wrist joints, right and left anterior *pelvis* extremities. (c)—Mouse skin. (d)—Initial (blue) and dense (red) sets of skin correspondences used for TPS organ approximation

4.2.3 Manual landmark selection

Using the Amira™ software and guided by an anatomical text book [7] the following 18 joint and bone landmarks were manually extracted in all 3 mouse datasets: 2 *femur/tibia-fibula*—knee joints, 2 *femur/pelvis*—hip joints, posterior and anterior extremities of the *sternum,* right and left anterior pelvis extremities, middle of the *atlas vertebra,* middle of the last *lumbar vertebra,* 2 *humerus/ulna-radius*—elbow joints, 2 *humerus/scapula*—shoulder joints, 2 *tibia-fibula/pes*—ankle joints and 2 *ulna-radius/manus*—wrist joints. Between the middle of the *atlas vertebra* and middle of the last *lumbar vertebra* respectively, the inner

---

[1] All animal protocols were approved by the Hospital for Sick Children Animal Care Committee

surface of the *columna vertebralis* was extracted. This whole step takes about 1 hour to execute and the final result can be seen in Figure 4.2.(b).

4.2.4   Joint identification

As mentioned above, the joints have to be indicated manually. To facilitate this procedure, we developed a method for automated joint identification. The expert does not have to follow a strict identification protocol every time but is free to indicate the joints in arbitrary order. Using the atlas joint locations, anatomically realistic bone dimensions, anatomically realistic Degrees of Freedom (DoFs) for each joint and a hierarchical anatomical model of the skeleton (please refer to [1] for details) all joints can be labeled. After identification of a hip joint, the more distal joints are identified by searching candidates that lie within a minimum/maximum Euclidean distance of the length of the atlas upper hind limb ± 15% as we consider a bone length in the atlas ± 15% as anatomically realistic variation. In addition, the knee joint has to lie within an anatomically realistic solid angle according to the properties of the hip, which is a ball joint. In most cases, this clearly identifies the knee joint but sometimes there can be two candidates, if the ankle joint is in approximately the same distance from the hip and the knee. In such a case, all possible hip, knee, ankle constellations have to be tested for plausibility.

4.2.5   Skin extraction

For each mouse dataset, triangular surface meshes of the skin were automatically extracted using the marching-cubes algorithm [8] after performing a chain of Gaussian smoothing(σ=5)-thresholding-morphological filtering on the original data to remove noise, artifacts and organ regions. See Figure 4.2.(c). This task and all the included steps was automatically executed using MeVisLab™ software [9]. Skin surface was simplified to approximately 2000 vertices using the QSlim method by Garland *et al.* [10]. Note that the extracted isosurface is not perfect, since it does not cover the mouse body to its full extent: the *pes* and the *manus* were left out. However, those are not necessary for the proposed method.

4.2.6   μMRI data organ approximation

Based on a subset of 14 of the manually selected landmarks (the wrist and the ankle joints are not used for mapping the organs) and four additional landmarks, derived using the manual spine approximation, a sparse set of 16 corresponding skin landmarks is derived. Since at many locations in the animal body, skin is very close to the skeleton, we simply take the skin vertex with the smallest Euclidean distance from each joint. Note that the initial set of correspondences was established for the atlas skin in the same manner as for the target. However, this has to be done only once. Starting from this sparse set of correspondences, a dense set of 99 correspondences on the skin is determined. To this end we use a method presented previously in [1]. In short, the method searches for new correspondences in the local neighborhood of the already established correspondences. To this end, local geodesic spectra for candidate vertices on the skin surface are determined and compared to geodesic spectra that are available for all atlas skin vertices. The pair of vertices in the target and the atlas that yields the highest geodesic spectrum similarity is added to the list of correspondences and so on. In several iterations,

vertices from all over the skin surface are added. Figure 4.2.(d) shows the initial set and the final set of correspondences on the target skin. Using the skin correspondences, the organs can be warped from the atlas domain to the subject domain. In its original form *i.e.,* if used as an interpolant, the TPS does force landmarks in the source domain to fit landmarks in the target domain exactly. However, due to the discretization of the skin surface, in general small spatial errors may occur and this can cause local distortions of the mapping. A remedy is to allow small landmark localization errors and relax the constraint of interpolation towards approximation (thin-plate smoothing spline [11]).

4.2.7   Rule-based µMRI data bone approximation

For mapping individual bones from the atlas to the target domain, we employ a similarity transformation model with 7 DoFs to account for translation and rotation as well as for differences in bone size. This means that in 3*D*, three corresponding points have to be known for each bone. Since all joint locations are available, most of the DoFs for each element can be resolved by mapping the joint in the atlas to the corresponding joint in the target. Taking the right upper hind limb (femur) for instance this means that the right atlas hip is mapped to the right target hip first, resolving the three translation parameters. Second, the right atlas knee is mapped to the right target knee, resolving two rotations and the scaling parameter. The third rotation parameter, the rotation with respect to the longitudinal axis of the bone, cannot be resolved using the hip and the knee joint only. However we can address this problem because the right ankle joint is available, knowing that the knee joint is a hinge joint. Since this joint type allows only one rotation of one bone with respect to the other, a longitudinal bone rotation can be resolved. Both knees as well as the elbows are hinge joints and therefore the transformation parameters for all eight limb bones can be determined uniquely. For the pelvis, four and therefore enough landmarks are available to derive the mapping transformation.

4.3   Experimental results

The validation of the organ approximation method was done using the 3 datasets with manually segmented organs described in 4.2. To have a quantitative estimation of the organ approximation method performance, the Dice index of volume overlap for 6 organs (liver, heart, kidneys, lungs, stomach and spleen) was calculated for the 3 mice and the MOBY atlas:

$$\text{Dice index} = \frac{2|V_s \cap V_a|}{|V_s| + |V_a|} \qquad (1)$$

where *Vs* and *Va* correspond to the subject and atlas volumes respectively.

Examples of the organ & bone approximation and the manually segmented mice are shown in Figures 4.3, 4.4 and quantitative results are presented in Table 4.1.
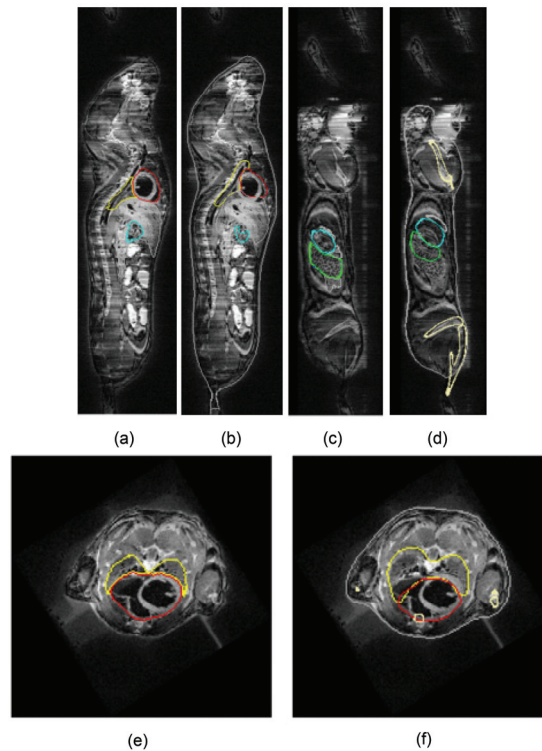
Figure 4.3 Organ & Bone approximation results for μMRI mouse data: (a), (c) & (e)—Manual Organ segmentation. (b), (d) & (f)—Organ & Bone Approximation results. Coronal & Sagittal planes respectively. *yellow*—lungs, *red*—heart, *green*—spleen, *cyan*—stomach, *cream*—bone, *grey*—skin, *white*—liver

The organ approximation method gives excellent fitting results for the heart and kidneys with maximum Dice indices 0.80 and 0.72 respectively. The worst result is obtained for the spleen with the dice index varying between 0.25 and 0.36. For the remaining organs—liver, lungs, stomach the fitting is of moderate success and the dice index is within the 0.39–0.68 interval. These results are comparable with the results obtained by Baiker *et al.* in [12] for μCT data. The heart and liver Dice indices are similar for both methods, whereas the method presented here is a little bit better with respect to the kidneys. However the lung approximation results in [12] are much better which can be explained by the fact that in μCT data this organ could be automatically extracted and registered to the atlas.

Regarding the bone approximation, although we present no quantitative assessment, in Figures 4.3.(d)., (f). and 4.4 it is visible that the obtained results are of moderate success. However there are visible misalignments, especially with respect to the pelvis and this can be explained by imprecisions in manual joint & bone landmark selection process.

The entire organ & bone approximation algorithm was implemented in MATLAB $R2008b$™ and took approximately 3 minutes of runtime in a $2.40GHz$ Intel Quad Core™ with $4GB$ of RAM, Windows™ PC.

(a)   (b)   (c)   (d)
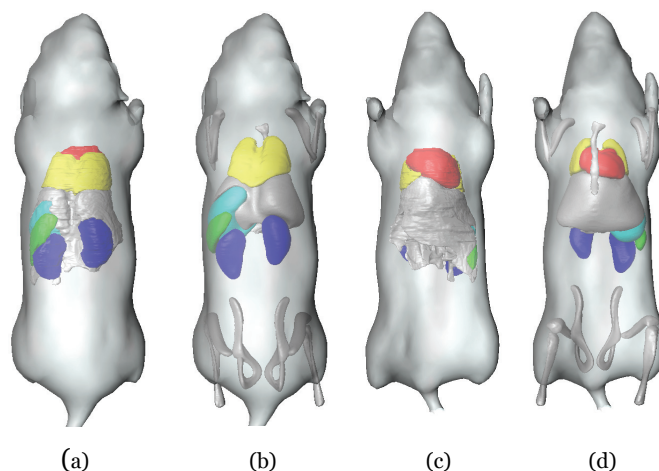
Figure 4.4 Manual Organ segmentation: (a) & (c). Bone and Organ Approximation: (b) & (d). Top & Bottom views respectively

4.4 Discussion and conclusion

In this paper a semi-automated atlas-based organ approximation method for μMRI mouse data is proposed. A manually extracted set of joint & bone landmarks and the automatically extracted skin are used to determine skin correspondences, which in turn are used for a TPS approximation of major organs (heart, lungs, liver, spleen, stomach, kidneys).

For some organs, the obtained results are generally satisfactory and similar to the manual segmentations (heart, kidneys, liver), while for other organs the atlas approximations are more variable. Especially for organs with inherent shape variability such as the stomach and spleen, errors were larger. Also, inaccuracies in manual landmark selection and imperfections in the skin extraction may contribute to these misalignments. In these cases, further manual correction of the contours is required. The computation time of the organ approximation method is very low and though the 18 manual landmark selection is a tedious process taking around 1 hour to perform it is much faster than the manual organ segmentation which takes around 10 hours to execute (for the 6 organs tested). This work represents a first step towards a more automated atlas-based skeleton and organ mapping. Also, a comparison with results obtained with other whole-body atlases like the Digimouse [13] is ongoing.

	Mouse 1			Mouse 2			Mouse 3			[12]
	V_s(mm³)	V_a(mm³)	Dice	V_s(mm³)	V_a(mm³)	Dice	V_s(mm³)	V_a(mm³)	Dice	Dice
Heart	292.62	227.16	0.65	282.36	241.83	0.80	292.56	202.19	0.74	0.81
Spleen	90.79	64.38	0.25	101.69	77.57	0.36	102.65	76.88	0.30	N/A
Lungs	421.15	392.78	0.39	429.74	437.26	0.56	344.55	362.38	0.44	0.70
Kidneys	264.57	268.10	0.43	301.28	268.94	0.72	305.68	231.27	0.72	0.48
Liver	1131.77	1776.11	0.63	1087.54	1939.77	0.68	1484.82	1551.95	0.63	0.73
Stomach	323.80	317.00	0.56	354.30	385.18	0.64	295.24	361.89	0.62	N/A

Table 4.1 Organ approximation results for 3 μMRI mouse datasets: dice indices for 6 major organs—heart, spleen, lungs, kidneys, liver, stomach. Last column: comparison with the automatic organ approximation results obtained by Baiker *et al.* [12] for μCT mouse data. *Vs*=subject volume, *Va*=atlas volume

Acknowledgments

References

[1]. Baiker M., Milles J., Dijkstra J. *et al. Atlas-based whole-body segmentation of mice from low-contrast micro-CT data* Med Image Anal 14(6): 723–737 2010

[2]. Joshi A. A., Chaudhari A. J., Li C. *et al. Posture matching and elastic registration of a mouse atlas to surface topography range data* Proc IEEE Intl Symp Biomed Imaging 366–269 2009

[3]. Wildeman M. H., Baiker M., Reiber J. H. C. *et al. 2D/3D registration of micro-CT data to multi-view photographs based on a 3D distance map* Proc IEEE Intl Symp Biomed Imaging 987–990 2009

[4]. Segars W. P., Tsui B. M. W., Frey E. C. *et al. Development of a 4-D digital mouse phantom for molecular imaging research* Mol Imaging Biol 6(3): 149–159 2004

[5]. Zhou Y. Q., Davidson L., Henkelman R. M. *et al. Ultrasound-guided left-ventricular catheterization: a novel method of whole mouse perfusion for microimaging* Lab Invest 84(3): 385–389 2004

[6]. http://www.amira.com

[7]. Bab I., Hajbi-Yonissi C., Gabet Y. *et al. Micro-Tomographic Atlas of the Mouse Skeleton* Springer 2007

[8]. Lorensen W. E. and Cline H. E. *Marching cubes: A high resolution 3D surface construction algorithm* Proc of the 14th Annual Conf on Computer Graphics and Interactive Techniques 163–169 1987

[9]. http://www.mevislab.de

[10]. Garland M and Shaffer E. *A multiphase approach to efficient surface simplification* Proc Conf on Visualization 117–124 2002

[11]. Wahba G. *Spline models for observational data*, SIAM ISBN-13: 978-0898712445 1990

[12]. Baiker M., Dijkstra J., Que I. *et al. Organ approximation in µCT data with low soft tissue contrast using an articulated whole-body atlas* Proc IEEE Intl Symp on Biomedical Imaging 1267–1270 2008

[13]. Dogdas B., Stout D., Chatziioannou A. *et al. Digimouse: a 3D whole body mouse atlas from CT and cryosection data* Phys Med Biol 52(3): 577–587 2007

4

Chapter 5

Interactive local Super-Resolution Reconstruction of whole-body MRI mouse data: applications to bone and kidney metastases

A. Khmelinskii, E. Plenge, P. Kok, O. Dzyubachyk, T. J. A. Snoeks, D. H. J. Poot, C. W. G. M. Löwik, C. P. Botha, W. J. Niessen, E. Meijering, L. van der Weerd and B. P. F. Lelieveldt submitted *2013*

A. Khmelinskii, E. Plenge, P. Kok, O. Dzyubachyk, D. H. J. Poot, E. Suidgeest, C. P. Botha, W. J. Niessen, L. van der Weerd, E. Meijering and B. P. F. Lelieveldt Proceedings of the 9th IEEE International Symposium on Biomedical Imaging: From Nano to Macro, Pages: 1723–1726 2012

Abstract

A resolution enhancing post-processing technique called super-resolution reconstruction (SRR) has recently been demonstrated to improve visualization and localization of micro-structures in small animal MRI. In such cases, however, the size of the animal under investigation relative to the size of the structures of interest can be very large. This results in high-resolution images of tens of millions of voxels. In such cases, solving the SRR problem becomes very expensive, in terms of both computation time and memory requirements. In this paper we introduce local SRR to overcome these problems. We present a novel method that combines state-of-the-art image processing techniques from the areas of articulated atlas-based segmentation, planar reformation and SRR and allows researchers to efficiently capture both global and local scales in whole-body small animal MRI. The approach is validated in two case studies involving CT, BLI and MRI data of bone and kidney tumors in a mouse model. Using only a few low-resolution images, and a total acquisition time compatible with in vivo experiments, we have produced SRR MR images from which detailed information about the metastases can be inferred. We show that local SRR MRI is a computationally efficient complementary imaging modality for the precise description of tumor metastases, and that it provides a high-resolution alternative to conventional MRI.

5.1   Introduction

In pre-clinical small animal research on skeletal complications of cancer, imaging modalities like bioluminescence (BLI), CT, and MRI are conventionally used. Such imaging techniques allow non-invasive studies on the metastatic behavior of tumors [1]. BLI gives an indication of metastatic tumor growth anywhere in the body (e.g. bones, liver and lungs), but the spatial resolution is not sufficient to distinguish between lesions located in close proximity to each other and to actually localize all individual metastatic processes in an organ. CT gives excellent contrast in calcified tissue and can be used to study tumor-induced changes in the bone, but due to lack of soft tissue contrast it is less suitable to image organs such as liver and lungs. MRI is the preferred imaging modality for imaging liver and lung metastases as it gives sufficient anatomical detail and good contrast between the organs and tumor masses. So, whereas BLI can be used to indicate the total tumor burden in an organ, MRI will give information on the exact location, size and number or metastatic lesions in that organ. Together, CT, MRI and BLI provide a comprehensive picture of the tumor and metastases development and spread in the entire body.

The sensitivity of MRI for small lesions is, however, relatively low compared to BLI, and the most robust pre-clinical protocols are still 2D MRI experiments, with relatively thick slices. This slice thickness results in a large partial volume effect, making precise detection and localization of tumors difficult, especially for early stage tumors and micro tumors [2]. Recently, a resolution enhancing post-processing technique called super-resolution reconstruction (SRR) has been demonstrated to improve visualization and localization of micro-structures in molecular MRI [3]. In a metastatic disease model, however, the size of the object under investigation (the mouse/rat) relative to the size of the structures of interest (the tumors) can be very large. When attempting to capture both global and local

scales in an image, this translates into a large field of view at high image resolution, resulting in images of tens of millions of voxels. In such cases, solving the SRR problem becomes very expensive, in terms of both computation time and memory requirements. Exploring large data sets in this way calls for conceptual new-thinking.

In this study, we overcome the computational issues of whole-body SRR by the combination of state-of-the-art methods from the areas of articulated atlas-based segmentation of whole-body small animal data [4–8], planar reformation [9], and SRR in MRI [3, 10]. We integrate these concepts into a novel localized approach to SRR that enables global-to-local exploration of e.g. whole-body mouse MRI data. The idea is similar to that of well-known web-based geographical maps, where it is possible, from a global overview image, to zoom in on a detail of interest. Guided by user interaction or by registration to images of higher sensitivity, such as BLI, local volumes of interest (VOIs) can be identified in the low-resolution MR image. From the global low-resolution overview these VOIs are then enhanced by SRR to show a higher level of detail.

The aim of our study is thus to determine whether SRR-MRI is a feasible method for improving visualization of tumors in small animal imaging. By feasibility we refer to two aspects:

(i) image quality: when the number of low-resolution images is constrained by acquisition times compatible with *in vivo* experiments, does our local SRR method improve the visualization of small anatomical details over conventional imaging methods?

(ii) computational feasibility: can the local SRR computations be handled on a desktop machine in a close-to-real-time time frame?

In the following sections, we first introduce our approach to local SRR in MRI. We briefly describe its components (for details we refer to previously published work in which each of the components has been thoroughly validated) and validate our approach in two case studies with bone and kidney tumor visualization, respectively.

5.2 Materials and methods

5.2.1 Experimental mouse model and imaging

To test the SRR approach, BLI, CT and MRI were acquired in a mouse model of metastasizing breast cancer. One female, *BALB/c nu/nu* mouse of 19.5 g was used. At 7–8 weeks of age, the mouse was injected with 4T1-luc2 [11, 12] breast cancer cells (100 µl, 150,000 cells) into the left heart ventricle under 2% Isoflurane anesthesia.

After 2–3 weeks BLI and CT scans were made *in vivo*. The anesthesia applied was Ketamine:RomPun:PBS (1:1:1), approximately 60 µl/20 g. This was followed by an *ex vivo* MRI scan. The mouse was euthanized to allow flexibility in the MRI experiments and test different acquisition parameters.

The mouse, lying on its belly, was taped to an in-house made PMMA holder that was used in all three scanners. For BLI imaging, the Xenogen™ VIVO Vision IVIS 3D scanner (Alameda, CA, USA) was used. The acquisition was done at a range of wavelengths between 580–680 nm, at 20 nm intervals with an acquisition time of 10 seconds per wavelength. One of the 8 BLI images is presented in Figure 5.1.

μCT data was acquired on a SkyScan™ 1076 *in vivo* X-Ray Microtomograph μCT scanner (Aartselaar, Belgium) at a resolution of 35 μm. The acquisition was performed with a step size of 1.4 degrees over a trajectory of 360 degrees (Voltage = 49 kV, Current = 200 uA, Exposure time = 100 ms, Filter: AL. 0.5 mm, Frame averaging = 1).

Several strategies can be adopted when acquiring MR data for an SRR experiment. By acquiring the low-resolution slice stacks with rotational increments around either the frequency or the phase encoding direction, as introduced in [13], a more effective sampling of k-space is achieved than by shifting the low-resolution images by sub-pixel distances along the slice selection direction [3]. In this fashion, a whole-body scan of the *post mortem* mouse was acquired on a 7T Bruker Pharmascan™ system using a fast spin echo (FSE) sequence. TR was 5300 ms, TE was 53.2 ms, with $N_{avg} = 4$. The 2D slice stack consisted of 40 slices (0.5 mm thick), with a FOV of 70×45×20 mm, and a resulting resolution of 0.125×0.125×0.5 mm. The scan time per stack was 13 min. The slice stack was acquired at 4 angles with uniform increments of 180/4 degrees around the phase encoding direction. In this study, we performed SRR on subsets of two and four low-resolution images. In the subset of two images, the angular increment between them was 180/2 degrees.

To compare the SRR results with a standard fast scan, an additional 2D scan of 5 minutes was performed. A FSE sequence was used, with a slice stack that consisted of 40 slices (0.5 mm thick), with a FOV of 70×45×20 mm, a resolution of 0.25×0.25×0.5 mm TR = 5300 ms, TE = 55.452 ms, $N_{avg} = 4$.

Animal experiments were approved by the local committee for animal health, ethics and research of Leiden University Medical Center.
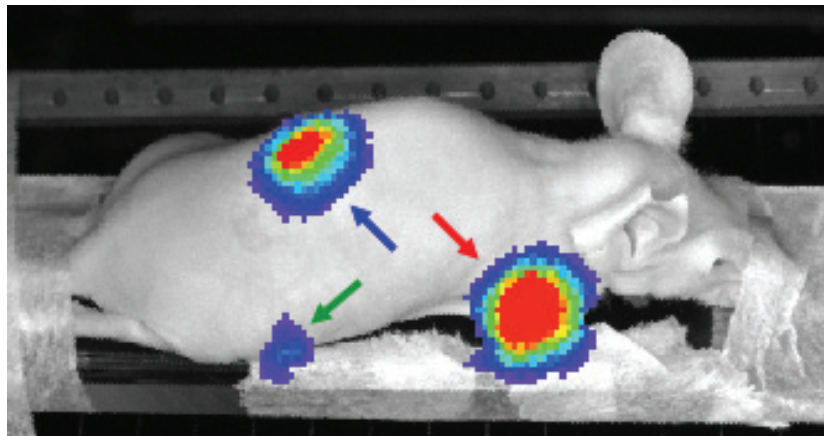

Figure 5.1 A BLI image of the mouse imaged to validate the proposed approach. The arrows indicate the different tumor locations: humerus (red), femur (green), kidney (blue)

5.2.2 Interactive local SRR reconstruction

The local SRR method integrates a series of processing and analysis steps, which depend on the available complementary data (CT, BLI, *etc.*) and vary in their level of user interaction. The overview of the presented method can be seen in the flowchart depicted in Figure 5.2: First, within of a set of low-resolution MRI images, potential VOIs are identified. In our approach this step is either based on user input or it is automated, as described below. Its output is one or more VOIs containing potentially relevant structures. One or more of these VOIs can now be selected for subsequent local SRR.

The methods for segmentation and selection of VOIs are highly specific to the biological problem and to the available complementary data. In the following, we present two situations typical in small animal tumor imaging, in which BLI+CT (Case Study A) and BLI only (Case Study B) are used as complementary modalities to MRI (see Figure 5.2). Each situation presents a different level of automation and requires a different degree of user interaction. The way the relevant information is extracted differs with the choice of the imaging modalities for the study at hand. In Case Study A, the level of user intervention is minimal. The whole-body mouse is automatically segmented using an articulated atlas. Guided by the BLI, the user can then select the VOIs with tumors for further SRR reconstruction, visualize the results side-by-side with the CT data, and, in case a tumor is present near a bone on one side of the body, compare it to the contralateral side, where most likely there is no tumor. In Case Study B, user interaction is necessary to co-register the BLI to the MRI data to define the VOIs. After that, the user can select among the VOIs in which the BLI signal indicate the presence of tumors for SRR reconstruction and further high-resolution visualization and analysis.

5
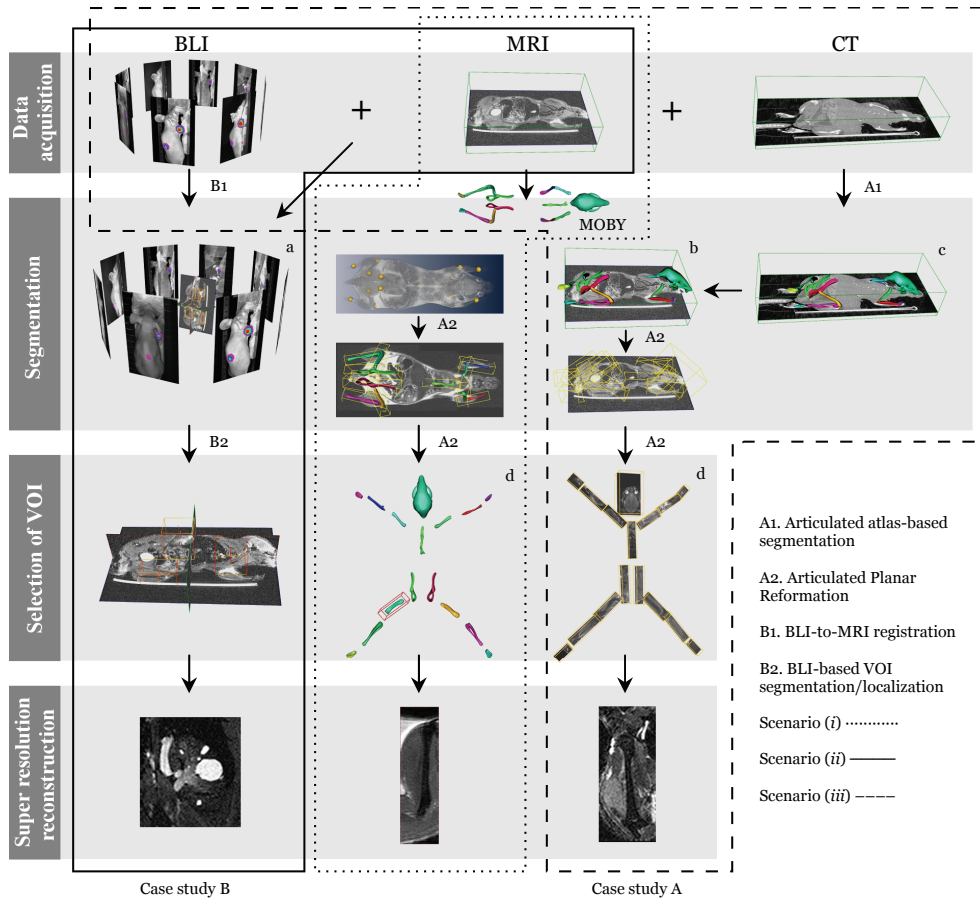
Figure 5.2 Overview of the interactive local SRR of MRI mouse data. Our approach was validated with two case studies. **A (bone metastases):** After rigidly registering CT to MRI, articulated atlas-based segmentation is performed (A1). Subsequently, articulated planar reformation is applied to the segmented MRI and the data is visualized in the standardized atlas space (A2). The user can now interactively select any low-resolution bone of interest guided by the BLI images. A high-resolution SRR image of the humerus with a tumor is presented. **B (kidney tumors):** BLI+MRI mouse data are first co-registered (B1) to define the VOIs (B2) using the BLI. A VOI is interactively selected for performing SRR. A high-resolution SRR image of the kidney with metastases is presented. A global solution to three possible scenarios that takes into account the availability of complementary data was provided: (*i*) only MRI is available [8], (*ii*) MRI+BLI is available, (*iii*) MRI+CT+BLI is available

5.2.3 Case study A: MRI+CT+BLI

This case study was set up to explore the value of SRR-MRI to image bone metastases as a complementary modality to CT, BLI and conventional MRI. In this section, we describe our approach to super-resolution bone MRI.

Articulated atlas-based bone segmentation of CT and MRI mouse data
First, rigid registration of the CT scan to one of the low-resolution MR images was performed [6, 14]. Rigid registration was sufficient in this case because the mouse was fixated in the same animal bed during all imaging procedures and during transport between scanners. The bones were segmented in the CT image using the articulated MOBY mouse atlas [5, 15] (Figure 5.2.c). The fully automated approach presented in [4] was used for this purpose. To deal with the large articulations between bones and/or bone groups, the registration of the atlas to the CT data used a hierarchical model tree. First, a coarse alignment of the MOBY atlas to the CT skeleton was performed. This was followed by the stepwise alignment of the individual atlas bones to the CT data, using the ICP algorithm [16]: we started with the skull, after which each bone was accurately registered to the correspondent bone in the data. Given the CT-to-MR registration parameters, the transform obtained in the segmentation of the whole-body CT data was propagated to the MR. Figures 5.2.b, c show the atlas fitted to the CT and MRI datasets, respectively.

Articulated planar reformation of MRI data
Using the obtained transformations between each bone in the atlas and the low-resolution MR image, articulated planar reformation [9] can be applied to map the labeled data into a standardized atlas space. This method automatically creates a VOI for each bone, which is based on a principal component analysis of the bone shape. By constructing the VOIs in this manner, the final reformatted images are aligned with the principal axes of the bones [9].

Interactive selection of VOIs
Upon segmentation and reformatting, the user is presented with a global view of the segmented bones, see Figure 5.2.d. Guided by the BLI signal, the user can now interactively select a bone for SRR reconstruction.

5.2.4 Case study B: MRI+BLI

This case study was set up to explore the value of SRR-MRI as a complementary modality to BLI and conventional MRI when CT data is not available for establishing anatomical correspondence. In practice, this is usually the case for soft tissue tumors, where bone metastases and bone resorption are not expected. In this section, we describe our approach to super-resolution MRI of kidney tumors.

BLI-to-MRI mouse data registration
After acquisition, the BLI images are registered to one of the low-resolution MR images using a landmark-based approach [6, 14]. A minimum of three landmarks is selected. The location of each landmark is indicated in one of the low-resolution MR images and in two separate BLI images at different angulations. Using the known angle between the two BLI images, back projection is used to find the corresponding point in the three-dimensional space. This point is then paired with the point in the MR image and registration is performed. Typical landmarks

include the snout and limbs because they are most easily identified in both modalities.

BLI-based VOI localization and segmentation

BLI-based VOIs can be localized by simple thresholding on the raw BLI signal. Once the coordinates of the VOIs in world space are known, the BLI-to-MRI registration transform is used to map the VOIs onto the chosen low-resolution MR image. The VOIs are then propagated to the remaining low-resolution MRI images using the transform parameters of these acquisitions. Finally, VOIs are extracted and can be used for SRR.

5.2.5 Super-Resolution Reconstruction

When a VOI has been selected and propagated to all rotated low-resolution MRI images, local SRR can be performed on the volume.

SRR is the process of producing a single high-resolution image from a sequence of low-resolution images, where each low-resolution image transforms and samples the high-resolution scene in a distinct fashion. It is an inverse problem in which the acquisition process is modeled as a linear operator on the high-resolution image. When the high-resolution image is vectorized and put into a large vector $\mathbf{x}$, the acquisition of the low-resolution image k can be modeled as $\mathbf{y}_k = \mathbf{A}_k \mathbf{x} + \mathbf{n}_k$, where $\mathbf{n}$ is Gaussian noise [17]. The linear operator $\mathbf{A}_k$ models the transform due to the rotation of the field of view of the kth image as well as the point spread function of the acquisition.

The objective in SRR is to find an $\mathbf{x}$ that minimizes the difference between $\mathbf{y}_k$ and $\mathbf{A}_k \mathbf{x}$ for all k simultaneously [3]. In general, a direct solution of this objective is not feasible since it involves many operations with all $\mathbf{A}_k \in \mathcal{R}^{n \times m}$, where n and m are the number of voxels in the reconstruction ($\mathbf{x}$) and in a low-resolution image ($\mathbf{y}_k$), respectively. Instead, the reconstruction is obtained by iterative methods such as the conjugate gradient method. In this study, we apply the method described in [10], which is a Tikhonov-regularized least-squares solver that implements $\mathbf{A}$ and $\mathbf{A}^T$ by an affine transformation scheme that minimizes aliasing and spectral distortion. The SRR method is extended with a bias-field correction step removing inhomogeneity over the images caused by variations in coil sensitivity.

5.2.6 Software platform

All computational experiments described beneath were implemented in MATLAB R2009b™ and performed on a 2.80 GHz Intel Xeon™ with 12 GB of RAM, Windows™ PC.

68

5.3 Results

5.3.1 Case study A: MRI+CT+BLI (bone tumors)

Local SRR images of the right femur and humerus with metastases were reconstructed at different levels of quality using 2 and 4 low-resolution images, and compared with conventional MRI, BLI and CT. In addition, reconstruction times of individual bones were compared with that of the entire mouse.

On BLI (Figure 5.1), three distinct signal areas were observed, the smallest one at the position of the right femur (green arrow). The user therefore manually selected the right femur for SRR of the MRI data, using 2 or 4 low-resolution images for the reconstruction SRR (2), and SRR (4) respectively (see Figure 5.3). The arrows in the BLI and the SRR (2) and SRR (4) images point to a tumor adjacent to the medial chondyle. This tumor is neither visible in the CT image, nor in the fast 2D MRI or in the raw low resolution image (1 LR). When using 2 low-resolution images for SRR, the image quality increases and the tumor becomes discernible. Using 4 low-resolution images further improves the visibility of the tumor and its margins.

BLI also showed a high intensity area at the location of the right humerus (Figure 5.1, red arrow). The tumor is not visible on CT. The fast conventional MRI scan does show the tumor, but, due to the relatively thick slices, the tumor margins are blurred, particularly in the transverse plane. As before, the image quality improves when using more low-resolution images, showing a clear delineation of the tumor, with SRR (4) being sharper and less noisy than SRR (2).

Table 5.1 shows how the SRR reconstruction times scale approximately linearly with the size of the low-resolution dataset. Since one low-resolution image of the entire mouse contains approximately 20 million voxels, and a typical VOI contains around 250,000 voxels, we accelerate the reconstruction by approximately a factor 80. From the table, it also follows that the SRR times scale approximately linearly with the number of low-resolution images used. While the entire mouse takes more than 40 minutes to reconstruct using 4 low-resolution images, the VOI can be reconstructed within 1–2 minutes.

The segmentation and selection of VOIs steps described above, each take less than a minute to perform.

5.3.2. Case study B: MRI+BLI (kidney tumors)

BLI showed a single high signal intensity around the area of the right kidney (Figure 5.1, blue arrow). Local SRR images of this area were reconstructed at different levels of quality and compared with conventional MRI and BLI. Figure 5.5 shows orthogonal slices of the kidney for the different image types (fast 2D MRI, one low-resolution image, and SRR on 2, and 4 low-resolution images). On the BLI in Figure 5.1, the spatial resolution is too low to determine whether multiple tumors are present, but on MRI one large tumor and several small metastases can be detected. Most of these are readily detectable on the fast 2D MRI, and the low resolution (1 LR) image. However, the tumors appear blurred and cannot be clearly delineated. In such images, the smallest metastases will be lost due to partial volume effects, but will be recovered in the SRR (2) or SRR (4) images. The high 3D

resolution of the SRR scans also shows that most of these metastases are located in the renal cortex and medulla, whereas the renal pelvis is relatively clean.

	2 low-resolution	4 low-resolution
Femur	56	98
Tibia-Fibula	38	75
Pelvis	79	151
Sternum	31	63
Humerus	48	83
Ulna-Radius	41	78
Whole-Body	1282	2479

Table 5.1 SRR times in seconds for each reconstructed right bone and the whole-body of the mouse, using 2 and 4 low-resolution images
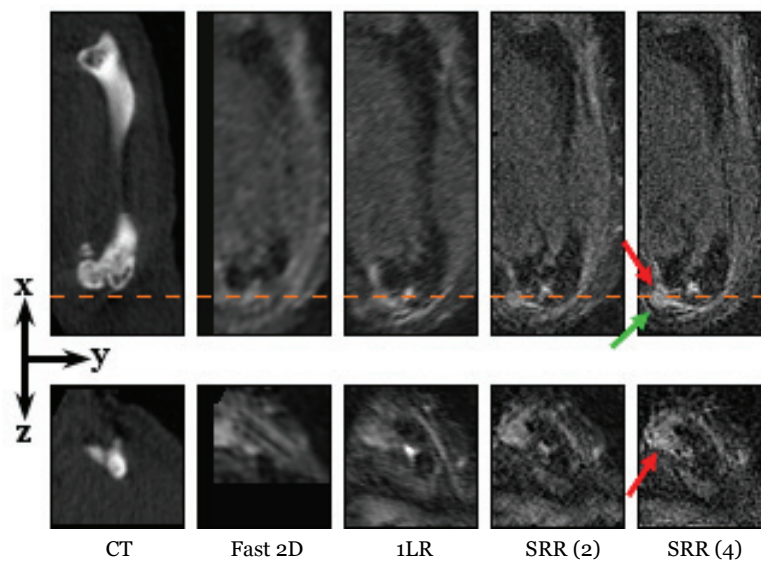
Figure 5.3 Right *femur*. From left to right: a CT scan, a fast MRI scan, one low-resolution image, and SRR reconstructions, each based on a different number of low-resolution images. Two orthogonal slices of the same VOI are shown to illustrate the effect of the SRR in a 3D volume. The orange dashed line indicates where the *yz*-slice (bottom) intersects the *xy*-slice (top). The red arrows points to the (micro) tumor in the knee. The green arrow points to another location, outside the tumor, at which recovery of the fine details is obvious. The CT and all the MR images are shown in the coordinate system associated with the principal axes of the bone, and Fast 2D and the low-resolution (1 LR) volumes are resampled to isotropic resolution beforehand. Image contrast on the MRI images was increased for visualization purposes
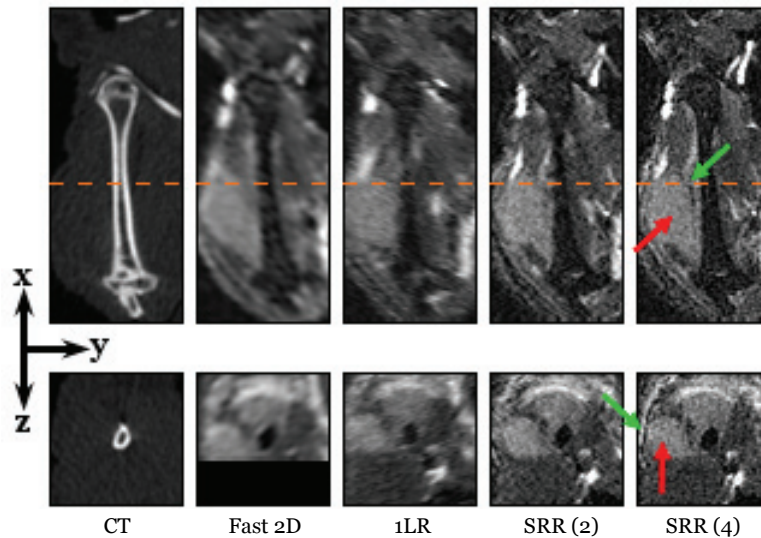
Figure 5.4 Right *humerus*. From left to right: a CT scan, a fast MRI scan, one low-resolution image, and SRR reconstructions each based on a different number of low-resolution images. Two orthogonal slices of the same VOI are shown to illustrate the effect of the SRR in a 3D volume. The orange dashed line indicates where the *yz*-slice (bottom) intersects the *xy*-slice (top). The red arrows point to the tumor. The green arrows point to some of the locations where recovery of the fine details is the most noticeable. The CT and all the MR images are shown in the coordinate system associated with the principal axes of the bone, and Fast 2D and the low-resolution (1 LR) volumes are resampled to isotropic resolution beforehand. Image contrast on the MRI images was increased for visualization purposes
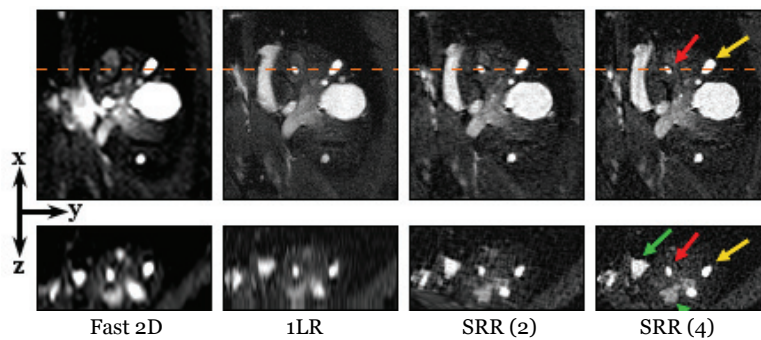
Figure 5.5 Right *kidney*. From left to right: a fast MRI scan, one low-resolution image, and SRR reconstructions each based on a different number of low-resolution images, of the right kidney. The red and yellow arrows point to two different tumors. Two orthogonal slices of the same VOI are shown to illustrate the effect of the SRR in a 3D volume. The green arrows point to other locations where the improvement in image quality is particularly noticeable. The orange dashed line indicates where the *yz*-slice (bottom) intersects the *xy*-slice (top). In all the MR images, the *xy*-view is the in-plane direction of the scans. Note that the metastatic lesion seen in the BLI image (Figure 5.1, blue arrow) actually consists of numerous lesions as shown on MRI scans. For the Fast 2D and the low-resolution (1 LR) the selected views are resampled to isotropic resolution and the image contrast on the MRI images was increased for visualization purposes. Note that for the Fast 2D view the shown slices do not correspond exactly to the other three views due to high sparsity of that data set

5.4   Discussion

5.4.1   Relevance to tumor research and other biological applications

Conventionally, bone resorption and metastases in soft tissues (such as kidney, lung and liver) are visualized using BLI+CT and BLI+MRI, respectively. In this study, we have explored the value of adding SRR-MRI t o improve soft tissue tumor detection. In two case studies, we have shown how an integrated approach, combining state-of-the-art technologies from the area of image processing with the use of multiple imaging modalities, can be used to detect and study bone and soft tissue metastases with much greater sensitivity than by the conventional methods.

In Case Study A, we saw how BLI is a sensitive method to visualize luciferase-positive tumors in a living animal. The BLI signal intensity is proportional to the size of a tumor mass, and BLI can thus be used to give a rough estimate of both size and localization of the lesion. In the case of bone metastases, the location and subsequent bone pathology are usually determined using CT [18]. However, in Case Study A there was no visible bone pathology in the CT scan. When local SRR-MRI was performed, guided by the BLI signal, these images provided the location, size and shape of tumors in the limbs of the animal and confirmed that these metastases were, indeed, soft tissue tumors located outside of the bone. In the conventional fast MRI of the femur, the tumor could not have been identified without the guidance of the BLI images. The SRR-MRI, on the other hand, clearly showed a nodular structure that could be identified as a tumor (Figure 5.3). In the humerus images, which contain a large tumor outside of the bone, it can be appreciated how the delineation of the tumor boundary becomes much sharper in the SRR-MRI than in the fast scan and the single low-resolution MR image (see Figure 5.4; note that the improvement in image quality is especially noticeable when using a high zooming factor). The method thus, has the potential to support detailed quantitative studies of *e.g.* metastases development and assessment of treatment response.

In Case Study B of kidney metastases, CT was not used, as this modality gives insufficient soft tissue contrast without the use of contrast agents. BLI indicated the presence of a cancerous lesion in or around the kidney (Figure 5.1, blue arrow). MRI revealed numerous independent metastases in the kidney (Figure 5.5), which is not possible with BLI alone due to its limited spatial resolution. Moreover, SRR-MRI allows the researcher to not only distinguish, but also to clearly delineate different tumors in close proximity. This cannot be achieved with conventional MRI, as illustrated in Figure 5.5. SRR-MRI can thus provide added value in studies where the number of metastases is an important parameter and where experimental treatment is used to intervene with the metastatic process. For instance, a researcher can differentiate between renal, adrenal and peri-renal cancerous lesions with SRR-MRI but not with BLI.

BLI remains the preferred standard measurement for active tumor size as the signal originates only from living cells and not from a necrotic core or cells killed by a certain treatment. Light, however, only has a limited penetration in bone and the bone can thus mask the BLI signal coming from small tumors which grow on the inside the bone, making these tumors appear smaller than they actually are. Having an MRI dataset in which the tumor can be identified and measured clearly helps overcoming these limitations.

72

An additional point to be made is the possibility to use BLI with SRR-MRI as an alternative for the CT anatomical reference, particularly in longitudinal studies where the repeated exposure to radiation in a CT scan may become a confounding factor or cause adverse effects [19].

Apart from oncology, the presented work flow may be of value in many research areas that requires whole body examination for local ((sub-) slice-thickness sized) effects. Examples are the homing of labeled stem cells after systemic injection, or imaging of systemic inflammatory diseases.

5.4.2 *Post mortem* to *in vivo* SRR-MRI

In this study, we have applied our approach to *post mortem* image data. However, we have well-founded reasons to believe that our results translate to *in vivo* imaging. The SRR quality depends on the amount of artifacts induced by animal movement. Such artifact are reduced by fast LR acquisitions and accurate subsequent registrations. While accurate non-rigid registration of soft tissue structures, such as liver and kidney may be possible, SRR is expected to be most successful for relatively rigid structures, such as the brain, bone, and tissue surrounding bone: cases in which rigid registration will yield accurate alignment of the low-resolution images. In [3], we showed SRR reconstructions of an *in vivo* mouse brain, and several studies have validated the assumption of accurate motion estimation in applications of SRR in fetal brain MRI [20, 21].

5.4.3 Interactive local SRR

One of the results of this work has been the development of an approach that integrates recent progress in the areas of articulated atlas-based segmentation of whole-body small animal data, planar reformation and SRR in MRI into a novel localized approach to SRR that enables global-to-local exploration of *e.g.* whole-body mouse MRI data. Together with the preliminary results first published in [8], we have provided a global solution to three possible scenarios that takes into account the availability of complementary data: (*i*) only MRI is available [8], (*ii*) MRI+BLI is available, (*iii*) MRI+CT+BLI is available (Figure 5.2). From first to last scenario, the proposed approach decreases in the required level of user interaction to segment the data into possible VOIs. Depending on the biological problem, the more complementary data available, the higher the level of automation of the approach and the more data there is for the user to explore, *i.e.:* in the approach of Case Study B (MRI+BLI), the user can choose only among VOIs in which BLI signal is present, for a subsequent SRR reconstruction. Alternatively, (if CT is available) the user can select any bone for the SRR reconstruction and thus compare left with right, compare a bone with a tumor, with the same bone without a tumor on the contralateral side, *etc*. Naturally, the more complementary data available in a study, the more information one can extract. Thus, while in (*i*) only MRI information is available, in (*iii*) one can fully integrate the information provided by the BLI (which quickly locates tumor growth and indicates tumor burden) together with the anatomical information provided by the CT (used to study tumor induced changes in the bone—bone resorption) and the soft tissue information provided by MRI (which can provide the information about the size and the number of metastases).

5.4.4 Image quality *vs* imaging time

A major constraint when applying SRR in small animal MRI is the limited acquisition time that *in vivo* experiments allow. Each of the low-resolution images takes a certain amount of time to acquire and acquisition of multiple such images may quickly exceed the time in which a mouse can be kept sedated. It was shown in [3], that relatively few images were necessary to achieve significant improvements in the image quality. In this study we have limited the number of low-resolution images to four, with a total acquisition time of 52 minutes, a realistic acquisition time for *in vivo* experiments. If the experimental setting allows it, the number of low-resolution images used can be extended at the expense of additional acquisition time. This will have some positive effect on the resolution. For an optimal coverage of k-space, the number of low-resolution images should be $\lceil \pi/2 \times F \rceil$, where F is the anisotropy factor, *i.e.*, the slice thickness relative to the in-plane resolution. In our case, that would mean using 7 low-resolution images. Using more than this number of low-resolution images will not have a significant impact on the resolution but will increase the SNR slightly (for an in-depth study of these trade-offs, we refer the interested reader to [3]).

The major advantage of SRR in small-animal MRI is that it enables obtaining isotropic images in scenarios where T2-weighted image contrast is desired, requiring long repetition times and therefore long scan times, particularly for a 3D acquisition. By combining a small number of relatively fast thick-slice acquisitions with SRR, an isotropic resolution close to the original in-plane resolution is obtained. For comparison, direct acquisition of a 3D fast spin echo image with the same resolution and acquisition parameters would take about 28 hours and thus is clearly infeasible.

5.4.5 Reconstruction times

For large datasets, the SRR method is limited by the memory available on the computer. For the conjugate gradient solver, up to 5 data structures, each the size of the final reconstructed image, and 2 additional data structures, each the size the total low-resolution data, must be kept in memory simultaneously. For large 3D data sets, this soon becomes impossible, even on a high-performance desktop computer. The interactive approach to locally reconstruct VOIs presented here, allows overcoming the time and memory limitations of the SRR technique. However, as shown in Table 5.1, the mean time for the best quality SRR result, *i.e.,* using 4 low-resolution images, is still in the order of minutes—91.3 s. The mean time for SRR using 2 low-resolution images is 48.8 s. These results are still far from the real-time target for this approach. Since the results presented here were acquired on a MATLAB™ implemented prototype, the computation times will decrease by re-implementing the algorithm in a C/C++ and GPU programming environment combination.

5.5 Conclusions

By combining a number of state-of-the-art image processing techniques, we have enabled a global-to-local exploration of whole-body mouse MRI. We have shown that the SRR-MRI is a valuable complementary modality in studies of tumor metastases. Using only a few low-resolution images, and a total acquisition time compatible with *in vivo* experiments, we have reconstructed SRR MR images from which detailed information about soft tissue metastases, not available in conventional imaging modalities, can be inferred. This cannot be obtained from direct MR acquisition within a feasible acquisition time.

Acknowledgments

5

References

[1]. Snoeks T. J., Khmelinskii A., Lelieveldt B. P. F. *et al. Optical advances in skeletal imaging applied to bone metastases* Bone 48(1): 106–114 2011

[2]. Gauvain K. M., Garbow J. R., Song S. K. *et al. MRI detection of early bone metastases in B16 mouse melanoma models* Clinical & Experimental Metastasis 22: 403–411 2005

[3]. Plenge E., Poot D. H. J., Bernsen M. *et al. Super-Resolution Methods in MRI: Can They Improve the Trade-Off Between Resolution, Signal-to-Noise Ratio, and Acquisition Time?* Magn Reson Med 68(6): 1983–1993 2012

[4]. Baiker M., Milles J., Dijkstra J. *et al. Atlas-based whole-body segmentation of mice from low-contrast micro-CT data* Med Image Anal 14(6): 723–737 2010

[5]. Khmelinskii A., Baiker M., Chen X. J. *et al. Articulated whole-body atlases for small animal image analysis: construction and applications* Mol Imaging Biol 13(5): 898–910 2011

[6]. Kok P., Dijkstra J., Botha C. P. *et al. Integrated visualization of multi-angle bioluminescence imaging and micro CT* Proc SPIE Medical Imaging 6509: 1-10 2007

[7]. Khmelinskii A., Baiker M., Chen X. J. *et al. Atlas-based organ & bone approximation for ex-vivo μMRI mouse data: a pilot study* IEEE Intl Symp on Biomedical Imaging 1197–1200 2010

[8]. Khmelinskii A., Plenge E., Kok P. *et al. Super-resolution reconstruction of whole-body MRI mouse data: an interactive approach* IEEE Intl Symp on Biomedical Imaging 1723–1726 2012

[9]. Kok P., Baiker M., Hendriks E. *et al. Articulated planar reformation for change visualization in small animal imaging* IEEE T Vis Comput Gr 16(6): 1396–1404 2010

[10]. Poot D. H. J., Van Meir V., Sijbers J. *General and efficient super-resolution method for multi-slice MRI* Proc 13th MICCAI: Part I, 615–622 2010

[11]. Kim J. B., Urban K, Cochran E. *et al. Non-invasive detection of a small number of bioluminescent cancer cells in vivo* PLoS One 5: e9364 2010

[12]. Bolin C., Sutherland C., Tawara K. *et al. Novel mouse mammary cell lines for in vivo bioluminescence imaging (BLI) of bone metastasis* Biol Proced Online 14(6) doi:10.1186/1480-9222-14-6 2012

[13]. Shilling R. Z., Robbie T. Q., Bailloeul T. *et al. A super-resolution framework for 3-D high-dimensional and high-contrast imaging using 2-D multislice MRI* IEEE Trans Med Imaging 28: 633–644 2009

[14]. CVP: http://graphics.tudelft.nl/pkok/CVP/

[15]. Segars W. P., Tsui B. M. W., Frey E. C. *et al. Development of a 4-D digital mouse phantom for molecular imaging research* Mol Imaging Biol 6(3): 149–159 2004

[16]. Besl P. J. and McKay N. D. *A method for registration of 3D shapes* IEEE T Pattern Anal 14(2): 239–256 1992

[17]. Gudbjartsson H. and Patz S. *The Rician distribution of noisy MRI data* Magn Reson Med 34(6): 910–914 1995

[18]. Baiker M., Snoeks T. J. A., Kaijzel E. L. *et al. Automated Bone Volume and Thickness Measurements in Small Animal Whole-Body MicroCT Data* Mol Imaging Biol 14(4): 420–430 2012

[19]. Hindorf C., Rodrigues J., Boutaleb S. *et al. Total absorbed dose to a mouse during microPET/CT imaging* Eur J Nucl Med Mol Imaging 37: S274 2010

[20]. Rousseau F., Kim K., Studholme C. *et al. On super-resolution for fetal brain MRI* Proc 13th MICCAI: Part II, 355–362 2010

[21]. Gholipour A., Estroff J. and Warfield S. *Robust super-resolution volume reconstruction from slice acquisitions: Application to fetal brain MRI* IEEE Trans Med Imaging 29: 1739–1758 2010

Chapter 6

A visualization platform for high-throughput, follow-up, co-registered multi-contrast MRI rat brain data

Abstract

Multi-contrast MRI is a frequently used imaging technique in preclinical brain imaging. In longitudinal cross-sectional studies exploring and browsing through this high-throughput, heterogeneous data can become a very demanding task. The goal of this work was to build an intuitive and easy to use, dedicated visualization and side-by-side exploration tool for heterogeneous, co-registered multi-contrast, follow-up cross-sectional MRI data. The deformation field, which results from the registration step, was used to automatically link the same voxel in the displayed datasets of interest. Its determinant of the Jacobian (detJac) was used for a faster and more accurate visual assessment and comparison of brain deformation between the follow-up scans. This was combined with an efficient data management scheme. We investigated the functionality and the utility of our tool in the neuroimaging research field by means of a case study evaluation with three experienced domain scientists, using longitudinal, cross-sectional multi-contrast MRI rat brain data. Based on the performed case study evaluation we can conclude that the proposed tool improves the visual assessment of high-throughput cross-sectional, multi-contrast, follow-up data and can further assist in guiding quantitative studies.

6.1 Introduction

Preclinical neuroimaging uses the combination of various imaging techniques to help understand the brain and treat brain disorders. One of the imaging techniques most frequently used to characterize the brain is multi-contrast MRI. Combined, this heterogeneous data allows overcoming the limitations of the individual imaging techniques by providing the researcher with complementary information. However, in studies with several subjects and multiple time-points, exploring and browsing through the multi-contrast, cross-sectional, longitudinal heterogeneous data becomes a very demanding task.

One way to combine heterogeneous data is to use image registration, which allows t o find the spatial relation between the cross-sectional, longitudinal or multi-modal images, thus combining them into a common reference frame [1–7]. In this work we focus on lifespan multi-contrast neuroimaging, where detection of local deformations over the lifespan is essential. Though several registration and brain analysis toolkits are publicly available [8–10], there are currently no simple, dedicated and easy to use applications that allow quick inspection of such life-span MR data in an integrated and intuitive way.

The main contributions of this work are:

   (i)   we provide an intuitive platform to integrate and visualize high-throughput co-registered multi-modal, cross-sectional follow-up data

  (ii)   our approach allows for an efficient data management and improves side-by-side exploration of high-throughput data by automatically linking the

same region of interest(ROI)/voxel in the datasets using the deformation field obtained during the registration. Combining the latter with a determinant of the Jacobian visualization [7, 11–18] allows for a more accurate and faster visual assessment of brain change/deformation with time

(iii)   the presented tool was evaluated by means of an end-user case study evaluation [19] with three experienced domain scientists and made publicly available. Life span, cross-sectional, multi-contrast MRI rat brain data was used

## 6.2   Materials and methods

6.2.1   A visualization platform for high-throughput, follow-up, co-registered multi-contrast MRI brain data

To model local deformation in different regions of the brain over an individual's life-cycle, non-rigid B-spline registration is used [1–7, 11–18]. After a registration is performed, the deformation field and its detJac are calculated. The deformation field is a vector image, where each voxel contains the information about its displacement (in physical coordinates) during the registration. The detJac extracts local expansion/compression information from the deformation field. In the construction of the data visualization application proposed in this work we explore the combination of displaying the images of interest (as originally acquired) with the information provided by the deformation field and its detJac.

When comparing 2 different datasets (*e.g.:* same subject, 2 time-points) the information provided by the deformation field is used to link the same ROI in the displayed datasets of interest: without distorting the original data one can automatically pin-point the exact same region/voxel in both datasets and understand what deformation the brain underwent from one time-point to another in all directions.

The detJac is used to inspect that deformation field: values between 0 and 1 indicate local compression, values above 1 indicate local expansion, and 1 indicates volume preservation [7, 11–18]. Identifying areas of local compression or expansion can facilitate the detection of areas of interest (brain change/deformation) in longitudinal studies and allows for a faster screening of the brain data before further proceeding to quantitative studies.

To handle high throughput co-registered data and to allow quick selection and switching between the hundreds of datasets a logical data management approach was devised. The final application consists of a two-step wizard: after the user defined the main data directory, a list of all the available co-registered data is presented, which can be sorted by subject name, age, modality or type of experiment; in the second step, the user performs the data analysis/exploration, selecting and switching between any dataset of interest. Figure 6.1 shows and describes in more detail the main components of the application.
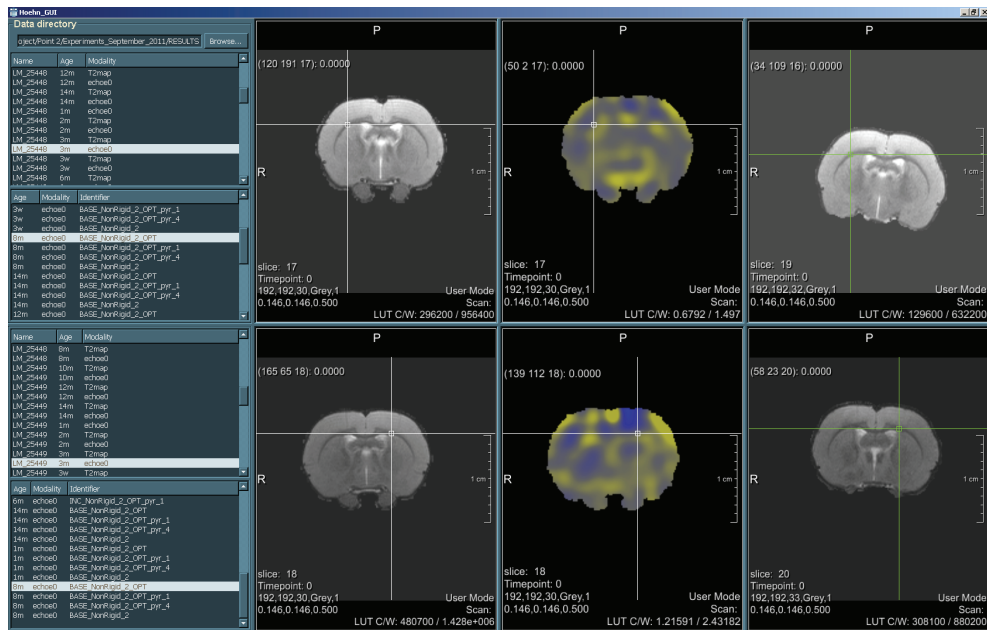
Figure 6.1 A screenshot of the proposed visualization platform for co-registered high-throughput multi-contrast, follow-up, cross-sectional MRI brain data exploration: Once the main directory is defined in (A), (B) presents a list with all the available data: different subjects acquired using different modalities in different time-points. This list can be sorted according to subject name, age or modality. After a baseline dataset of interest is selected in (B) a list of all the datasets co-registered to it (other subjects, time-points, modalities, types of experiment) is presented in (C). This way a quick overview of the co-registered data is available. The view panel (D) shows the selected baseline from (B), and panel (F) shows the dataset of interest that was previously co-registered to the selected baseline. These 2 datasets of interest are now automatically linked using the deformation field obtained in the registration. This way, the anatomical location of a voxel in the baseline dataset on the left (white cursor), is pinpointed on the right (green cursor) allowing for an intuitive side-by-side exploration of the original, non-distorted data. The view panel in the middle (E) shows the detJac, allowing for a quick visual assessment of brain change/deformation that occurred between the time-point in (D) and the time-point in (F). Values above 1 (bright yellow) indicate local expansion, values between 0 and 1 (bright blue) indicate local compression and values equal or very close to 1 (grey) indicate volume preservation. The bottom row—(B'), (C'), (D'), (E') and (F') duplicates the functionality of the top row—(B), (C), (D), (E) and (F). This allows making different types of comparisons as described in the paragraph above. The images displayed are an example of the co-registered rat brain data: on the top row two time-points for subject S1 are shown and compared to the bottom row where the same time-points for subject S2 are presented

6.2.2 Experimental set-up

To demonstrate and evaluate the application potential of the proposed visualization and exploration tool from an end-user point of view, a case-study with three experienced domain scientists was performed. Multi-contrast longitudinal MRI rat brain data from an existing life span study, exploring juvenile development and ageing processes of the brain was chosen to test the application.

6.2.3 Rat brain data

From postnatal day 21, two groups of four male *Wistar* rats (Harlan-Winkelmann GmbH, Borchen, Germany) were housed pairwise under standardized environmental conditions. Food restriction (80% of ad libitum consumption) started at an age of about 3 months in order to minimize obesity, a risk factor for age-related diseases [20]. The different groups were introduced into the study with different ages: Group 1 was followed from the age of three weeks with data available up to 14 months at the time of co-registration; Group 2 from ten until 24 months.

Animals were employed in MRI experiments on a bimonthly basis, with supplementary scans in the first 3 months to account for the fast cerebral growth. MRI experiments were conducted on an 11.7 T Bruker BioSpec™ horizontal bore scanner (Bruker Biospin, Ettlingen, Germany). Animals were anaesthetized using 2% Isoflurane (Forane, Baxter, Deerfield, IL, USA) in 70:30 N2O:O2, and vital functions were monitored continuously.

This study design shows traits of both a longitudinal and a cross-sectional approach. This beneficial combination allows monitoring the development of the same individuals over time, and at the same time excluding, or identifying possible long-term effects created by repeated measurement and anaesthesia.

T2 weighted images were chosen for their anatomical detail, diffusion tensor imaging (DTI) for the information on tissue anisotropy and myelination. T2 maps were calculated from an MSME (multi slice multi echo) sequence (10 echoes) with TE = 10 ms, TR = 5000 ms (IDL version 6.4, Boulder, CO, USA). The DTI datasets were used to calculate fractional anisotropy (FA), mean diffusivity (MD) and eigenvalue maps (DTI studio version 3.0.3, Baltimore, MD, USA). Both datasets were acquired with identical geometry, slice positioning and spatial resolution (FOV = 28 x 28 mm, resolution 0.146 x 0.146 mm inplane and 0.5 mm slice thickness; without gaps). Multiplying the number of subjects by the number of time-points and by the numbers of different MRI maps the total number of datasets exceeds 500.

6.2.4 Image registration

Image registration was performed between every two consecutive time-points and between each time-point and the baseline. In Group 1, the 3m old brain served as the baseline, for Group 2, the 10m old brain served as baseline. All registrations were performed using the first echo of the MSME data, chosen for its high anatomical detail and high SNR. The resultant transforms were propagated to the T2 maps and the DTI data. To compensate for any rotation, translation and scaling that exists between different datasets, rigid and affine transformations were applied. These are linear global transformations. To model local differences that allow detecting changes in different regions of the brain over the life-cycle (deformation, volume change, eventual tumor development, *etc.*), non-rigid B-spline registration was performed after the global initialization. For this data the following parameters were chosen: normalized correlation coefficient as a similarity measure, a four-level Gaussian image pyramid with downsampling and the B-spline with an eight point spacing transformation model. For all images a binary mask was available, made by an expert using the BET tool of the FSL package [9]. The image registration was performed using the publicly available `elastix` toolbox [7, 21].

With the registration results for any possible combination of data at hand, one can easily choose what to visualize and compare side-by-side: same subject-same modality-different time-points, different subjects-same modality-same time-points, same subject-different modalities-different time-points, different subjects-different modalities-same time-point, *etc*. The presented tool was developed in MeVisLab™ [22], is cross-platform and does not require any other software to be installed.

6.2.5 End-user evaluation and results

The proposed visualization and exploration tool was evaluated based on the principles and terminology set out by Yin for case study research [19]. The main study question was formulated as: *"How can the visualization platform assist neuroimaging researchers in studying changes over time in multi-modal rat brain data?"* and the case was defined as *"use of the tool by three domain and widely published scientists, referred to as DW, a clinical and experimental MRI expert, CB, a medical and pre-clinical visualization expert and LvdW, a neuroimaging, pre-clinical MRI expert"*. None of the users was involved in any stage of the development of the application before taking part in the evaluation presented here. Together with each of the domain scientists, in three separate, independent sessions, we used the application to analyze the multi-contrast, follow-up cross-sectional rat brain MRI data. That data was acquired to study juvenile development and ageing processes of the brain. During the evaluation sessions, feedback on the application was gathered and structured according to the following study propositions. Following, each proposition is stated, together with its related feedback, after which general comments and preliminary conclusions are presented.

Easy to use, does not have a steep learning curve

All three users confirmed this statement. CB added that all basic functions were straight-forward and indeed after a few minutes of explanation one could start using the application and that one of the positive aspects of the application was that since all files in the user-defined directory followed a naming convention all the data could be easily read by application. He also pointed out that it was positive that selecting a baseline automatically showed all registered datasets to ease selection of the follow-up datasets. LvdW also confirmed that the application was straightforward and intuitive to use. Both CB and LvdW suggested that auto-adjust the window-level for each selected dataset would be an improvement and that it should also be linked between the datasets being compared side-by-side.

The proposed platform allows for a fast selection and switching between the datasets of interest, efficiently handling the high-throughput data (more than 500 datasets).

DW confirmed this statement. CB commented that the tool indeed allows for fast selection from large sets, without having to waste time with orthodox file opening dialogs. However, there is room for improvement in terms of assisting the user in their progress, for example keeping track of comparisons they've made, perhaps even suggesting interesting comparisons based on image metrics. CB found the proposition a bit too broadly defined: he fully agreed that it facilitates selection and comparison, but there is more to be done in terms of integrated efficient handling of high-throughput data. LvdW noticed that the application is indeed convenient to

load registered/linked data and suggested an improvement: make it possible to sort the data based on modality, subject, age, *etc.*

Automatically linking the same ROI/voxel in the displayed datasets, by using the deformation field of the previously performed registration improves side-by-side exploration of follow-up data.

DW confirmed that the linked cursor improved side-by-side exploration. CB noted that indeed this is an effective way that helps one to relate the registered parts of the two datasets being compared, adding that an interesting possibility would be extending the cursor's region of influence, so that local deformation could be better investigated. LvdW commented that automatic linking contributed to a considerable time saving.

The proposed platform allows for an intuitive exploration of cross-sectional and multi-modal data.

DW and LvdW agreed with the statement, the latter one adding that one really gets to know their data well with this application. CB stated that he was not sure what intuitive meant in this context. He added that slice-views were important in any application based on tomographic data and this tool enables basic comparison with slice-views, and so can form a basic part of any comparison toolbox. He expects that it will be useful for the visual inspection of cross-sectional and multi-modal data.

Combining the display of the two time-points of interest together with a detJac visualization allows for a more accurate and faster visual assessment of brain change/deformation.

DW agreed with this statement. CB stated that the detJac visualization is definitely useful for the quick location of areas of significant shrinkage and expansion, which is important in many small animal follow-up studies. He added that side-by-side visualization of time-points is a basic but reliable way to compare data and in the case of this tool, one could also consider putting the baseline and follow-up views directly adjacent to ease comparison. LvdW said that the assessment of brain change/deformation was definitely faster also because of the linked cursor.

The above also holds true in the detection of asymmetries in brain deformation.

All three users agreed with this statement. CB added, that indeed it seemed easy to spot (as)symmetries in the colour coded detJac and that it would help to have a detJac threshold operator to filter out small changes.

All three also suggested that a colorbar showing color scale of the detJac would be helpful.

The tool can be also used for a fast, qualitative assessment of the registration accuracy, since one can quickly check if the clicked points in image-time-point 1 have the correct correspondence in the image-time-point 2.

All three users agreed that the tool could be in principle used to qualitatively assess the registration accuracy. DW commented that one could recognize misregistration, but for a routine quality check he prefers an overlay image. CB stated that he was not convinced, because one has to probe the positions. He agreed that one can spot-check easily for registration accuracy, but this is not the best way to check for whole slices or even the whole volume. In the case of slices, he would prefer also having alpha-blended slices or even red-green blended slices.

LvdW stated that it required some expertise for someone to notice that something is wrong with the registration accuracy and that this was not the most obvious tool for that; if we want to make it visual, she'd rather look at a difference image.

The tool can help guide the quantitative study of age-related brain deformation, in that, areas of interest can be localized and qualitatively assessed before further studied

DW agreed with the statement and added that it had indeed potential. CB also confirmed this statement, adding that this kind of explorative tool should be part of any quantitative analysis pipeline, both for quality checking the data and for finding areas of interest that deserve further quantification. LvdW stated what this tool is something that she'd certainly use for getting a feel for the data, since often, one starts by looking through the data to see what quantification use in the experiment. She concluded by adding that a possibility to draw a region of interest and propagate through all the time-points would also be advantageous.

Regarding the execution times of the implemented tool, once the user defined the main data directory, the elaboration of the list of all co-registered datasets organized by subject name, age and modality (more than 500) takes no more than10 seconds on a 2.40GHz Intel Quad Core™ with 4GB of RAM, normal Windows™ desktop PC. Once the list is ready, the selection and switching between different datasets of interest takes around one tenth of a second.

6.3 Discussion and conclusion

In vivo visualization of functional and anatomical information produces heterogeneous, high throughput data. Efficiently combining, analyzing and quantifying whole-body small animal cross-sectional, longitudinal and multi-modal data is a complex problem. In this paper, we demonstrated the feasibility of the articulated atlas-based skeleton segmentation approach combined with the articulated planar reformation algorithm for whole-body mouse bone imaging using SPECT.

In this paper we presented a tool that allows to visualize and explore high-throughput multi-contrast, cross-sectional follow-up co-registered MRI data of rat brain. It is independent of the used registration toolkit and does not distort the original data. Using the proposed tool, one can automatically link the same ROI in the displayed datasets by using the deformation field of the previously performed registration, thus improving side-by-side exploration of follow-up data and quickly visually assess brain change/deformation by combining the display of the two time-points of interest together with a detJac visualization.

The proposed visualization and exploration platform was evaluated by three domain experts based on the methods set out by Yin [19] for case study research. All three were enthusiastic with the application. CB commented that he expects it to be useful for the visual inspection of cross-sectional, follow-up and multi-contrast data and form the basis of any comparison toolbox. LvdW commented on the possibility of using the tool in future studies in her research group once the tool becomes publicly available. All three domain experts commented that to assess the

registration accuracy they would prefer either a difference or an overlay or and alpha-blended image. The authors agree with this comment, but since the evaluation of the registration accuracy was not the main concern while implementing this tool, it is definitely a feature that one can add in the future versions together with the option to draw ROIs and propagate their deformation through all the time-points.

Since the performing of the case study evaluation with the domain experts, we implemented several essential suggestions made by the users: auto-adjustment of the window-level and its linkage between the datasets that are being compared; make it possible to sort the listed data (based on modality, subject, age, *etc.*); add a threshold operator to filter out changes and a colorbar showing the color scale of the detJac. Based on the analysis of the performed case study we can conclude that the proposed application can improve the visual assessment of high-throughput multi-contrast follow-up data and further assist in guiding the quantitative studies. The proposed tool was tested and evaluated using longitudinal MR rat brain data. However, it can be applied to any type of co-registered pre-clinical or clinical follow-up, cross-sectional multi-modal data.

Besides the input from the interviewed domain experts, we must add that from our own experience, the side-by-side visualization tool combined with the detJac map was successfully used to identify and follow in time a spontaneous brain tumor growth, later confirmed *ex vivo* and identified as melingeoma [23]; and to detect changes in cortical thickness during juvenile development allowing the creation of physiologically meaningful ROIs for quantitative analysis of imaging parameters [24].

To add new options and features, the presented tool, together with the correspondent source code and a user-manual will be made publicly available for download via www.lkeb.nl

Acknowledgments

References

[1].   Maintz J. B. A. and Viergever M. A. *A survey of medical image registration* Med Image Anal 2: 1–36 1998

[2].   Zitova B. and Flusser J. *Image registration methods: a survey Image* Vision Comput 21: 977–1000 2003

[3].   Lester H. and Arridge S.R. *A survey of hierarchical non-linear medical image registration* Pattern Recognit 32(1): 129–149

[4].   Hill D. L. G., Batchelor P. G., Holden M. *et al. Medical image registration* Phys Med Biol 46(3): R1–R45 2001

[5].   Hajnal J.V., Hill D. L. G. and Hawkes D. J. editors *Medical image registration* CRC Press 2001

[6].   Modersitzki J. *Numerical methods for image registration* Oxford University Press 2004

[7].   Klein S., Staring M., Murphy K. *et al. elastix: a toolbox for intensity based medical image registration* IEEE T Med Imaging 29(1): 196–205 2010

[8].   Gouws A., Woods W., Millman R. *et al. DataViewer3D: An Open-Source, Cross-Platform Multi-Modal Neuroimaging Data Visualization Tool* Front Neuroinformatics 3: 9 2009

[9].   http://www.fmrib.ox.ac.uk/fsl/index.html (Version 4.1.7)

[10]. http://www.freesurfer.net/

[11]. Rohlfing T., Maurer Jr. C. R., Bluemke D. A. *et al. Volume-preserving nonrigid registration of MR breast images using free-form deformation with an incompressibility constraint* IEEE T Med Imaging 22(6): 730–741, 2003

[12]. Lorenzi M., Ayache N. and Pennec X. *Alzheimer's Disease Neuroimaging Initiative, Schild's Ladder for the Parallel Transport of Deformations in Time Series of Images* Inf Process Med Imaging 22: 463–74, 2011

[13]. Maheswaran S., Barjat H., Rueckert D. *et al. Longitudinal regional brain volume changes quantified in normal aging and Alzheimer's APP×PS1 mice using MRI* Brain Res 1270: 19–32 2009

[14]. Lau J. C., Lerch J. P., Sled J. G. *et al. Longitudinal neuroanatomical changes determined by deformation-based morphometry in a mouse model of Alzheimer's disease* Neuroimage 42(1): 19–27 2008

[15]. Zamyadi M., Baghdadi L., Lerch J. P. *et al., Mouse embryonic phenotyping by morphometric analysis of MR images* Physiol Genomics, 42A(2): 89–95 2010

[16]. Spring S., Lerch J. P. and Henkelman R. M. *Sexual dimorphism revealed in the structure of the mouse brain using three-dimensional magnetic resonance imaging* Neuroimage 35(4): 1424–33 2007

[17]. Falangola M. F., Ardekani B. A., Lee S. P. *et al. Application of a non-linear image registration algorithm to quantitative analysis of T2 relaxation time in transgenic mouse models of AD pathology* J Neurosci Methods 144(1): 91–7 2005

[18]. Lerch J. P., Carroll J. B., Spring S. *et al. Automated deformation analysis in the YAC128 Huntington disease mouse model* Neuroimage 39(1): 32–9 2008

[19]. Yin R. K. *Case study research: design and methods* 4th edn. Sage 2009

[20]. Mattson M. P. and Wan R. Q. *Beneficial effect of intermittent fasting and caloric restriction on the cardiovascular and cerebrovascular systems* J Nutr Biochem 16: 129–137 2005

88

[21]. http://elastix.isi.uu.nl

[22]. http://www.mevislab.de/ (Version 2.1(VC8))

[23]. Khmelinskii A., Mengler L., Kitslaar P. *et al. Interactive system for exploration of multi-modal rat brain data* Proc EMIM 2011

[24]. Mengler L., Khmelinskii A., Po C. *et al. Juvenile development and ageing mediated changes in cortical structure and volume in the rat brain* Proc EMIM 2011

6

Chapter 7

Brain maturation of the adolescent rat cortex and striatum: changes in volume and myelination

Abstract

Longitudinal studies on brain pathology and assessment of therapeutic strategies rely on a fully mature adult brain to exclude confounds of cerebral developmental changes. Thus, knowledge about onset of adulthood is indispensable for discrimination of developmental phase and adulthood. We have performed a high-resolution longitudinal MRI study at 11.7T of male *Wistar* rats between 21 days and six months of age, characterizing cerebral volume changes and tissue-specific myelination as a function of age. Cortical thickness reaches final value at 1 month, while volume increases of cortex, striatum and whole brain end only after two months. Myelin accretion is pronounced until the end of the third postnatal month. After this time, continuing myelination increases in cortex are still seen on histological analysis but are no longer reliably detectable with diffusion-weighted MRI due to parallel tissue restructuring processes. In conclusion, cerebral development continues over the first three months of age. This is of relevance for future studies on brain disease models which should not start before the end of month 3 to exclude serious confounds of continuing tissue development.

7.1   Introduction

Brain development is a continuous process, which proceeds well after birth and even adolescence. Most studies employing rats claim to use "young adults", implying a fully matured brain parenchyma. However, the definition for "young adults" is diverse and ranges between two and four months old and body weight of 200 to 350 g.

For longitudinal studies it is particularly important to be able to discriminate between natural, development-dependent tissue changes and those alterations due to induced diseases or lesions. As individual organs, tissues and microstructures mature at different paces, great care must be taken in choosing the age and observation period for the animal model of interest.

Adolescence is understood as the time of transition between infancy and adulthood, despite a lack of clear and unambiguous boundaries between those stadiums. In some cases, adulthood is used equivalent to full sexual maturity. Depending on the research interest, adolescence is described by changes in social [1], cognitive or risk-taking behavior [2], but also in the neurotransmitter system [3]. The onset and extent of this phase may differ for different strains/breeds, between the sexes and for further different parameters, and conservative age range includes postnatal days 28 to 42 [4]. This time window starts about a week after rat's weaning age and ends shortly after sexual maturity.

As many of these characterizations were based on group comparisons at different ages, they describe mere group averaged values, while inter-individual variability in the temporal profile of development may be completely lost. We hypothesized that intra-individual longitudinal studies using noninvasive imaging modalities may allow the identification of biomarkers of developmental phases of the brain which will distinguish between an early, adolescent period of pronounced cerebral development and a later, matured, "steady state" cerebral adulthood. We further hypothesized that such biomarkers could be reflected either in anatomical,

structural and volume changes over time or in quantitative tissue characterization through physiology-based imaging parameters. For this purpose, we have followed male *Wistar* rats from 21 days until 6 months. We measured whole brain, cortical and striatal volume changes with high-resolution T_2-weighted MRI to look for structure-related biomarkers. For developmental tissue changes, T_2 relaxometric imaging and diffusion imaging was recorded to investigate the microstructure of the tissue and the myelination, respectively.

7.2   Materials and methods

7.2.1   Animals

All animal experiments were conducted in accordance with the German Animal Welfare Act and approved by the local authorities (Landesamt für Naturschutz, Umwelt und Verbraucherschutz NRW). From postnatal day 21 on (weaning age) twelve male *Wistar* rats (Harlan-Winkelmann GmbH, Borchen, Germany, and Janvier, Le Genest Saint Isle, Cedex, France) were held in an environment with controlled temperature (21+/-1°C), humidity (55%+/-10%), and light (12/12h dark/light cycle). Animals were housed in groups of four until the age of two months, and in pairs afterwards, and were given access to food and water *ad libitum*.

7.2.2   Study design

Animals were subdivided into three survival groups: three weeks (n=4), three months (n=4) and six months (n=4) to obtain histological specimens of all those ages. MRI experiments were conducted at the age of three weeks (3W), one (1M), two (2M), three (3M) and six (6M) months, until sacrifice, depending on group. Hereafter, we will refer to these time points using the above-introduced abbreviations.

7.2.3   MRI

MRI experiments were conducted on an 11.7T Bruker BioSpec horizontal bore, dedicated animal scanner (Bruker Biospin, Ettlingen, Germany). RF transmission was achieved with a quadrature volume resonator (inner diameter 72mm), while a quadrature rat brain surface coil (~30mm x 30mm) was used for signal reception. After induction of anesthesia with 3% isoflurane, rats were placed in an MRI compatible cradle, and the head was fixed with ear bars and a support ring for the upper incisors in order to reduce movement artifacts. Animals were anesthetized with 2% isoflurane (Forane, Baxter, Deerfield, IL, USA) in a 70/30 mixture of N_2O and O_2, and vital functions were monitored during the whole anesthesia period using DASYLab (version 9.0, Measurement Computing Cooperation, Norton, MA, USA). The breathing rate was assessed via a breathing pillow, placed under the thorax, and kept at 70–80 breaths/minute by adjusting the isoflurane concentration. Body temperature was recorded with a rectal temperature probe, and regulated by a feedback system (set value: 37°C) controlling a heating blanket with warm circulating water (Medres, Cologne, Germany).

T$_2$-weighted imaging (T2WI) was chosen for the anatomical detail of the images (first TE) and the information on tissue microstructure. Diffusion tensor imaging (DTI) was acquired for information on tissue anisotropy and myelination. Both scan protocols, T2WI and DTI, were set to cover the volume between olfactory bulb and cerebellum and were acquired with identical geometry (field of view: 28mm x 28mm, matrix 192 x 192, 0.5 mm slice thickness, no interslice gaps). The number of slices was adjusted individually in every session in order to account for brain growth.

T2WI was acquired using a Multi Slice Multi Echo sequence (MSME; TR/TE=5,000ms/10ms; 10 echoes with 10ms inter-echo spacing). DTI was recorded with an 8-shot spin echo EPI sequence (30 directions; b-value=630s/mm², and five supplementary A$_0$ images) using a Stejskal-Tanner sequence.

The TurboRARE sequence, used for the generation of the rat brain template, used a TR/TE$_{eff}$ = 4,000ms/32.5ms and a RARE factor of 8. Two averages were recorded with a field of view 28mmx28mm (matrix 192x192) and 0.5 mm slice thickness.

7.2.4   Postprocessing

Quantitative T$_2$ maps were calculated from the MSME multi-echo trains assuming mono-exponential decays, using IDL (IDL version 6.4, Boulder, CO, USA). Raw diffusion data was first eddy current corrected (FSL version 4.1.7, FMRIB Centre, Oxford, UK). Then, eigenvalues (λ_1, λ_2, λ_3) and mean diffusivity (MD) maps were calculated using DTI Studio (DTI studio version 3.0.3, Baltimore, MD, USA). As the tensor elements have been reported to be more sensitive than the fractional anisotropy (FA) alone which is a mathematical expression of the combination of the tensor elements [5, 6, 7], we have focused our analysis on $\lambda_\parallel$ and $\lambda_\perp$. The three eigenvalues stand for the length of the three principal axes (directions) measured in diffusion tensor imaging. The first, largest eigenvalue (λ_1) represents the axial or parallel diffusivity ($\lambda_\parallel$), while the perpendicular or radial diffusivity ($\lambda_\perp$) is the average of the two minor axes, the second (λ_2) and third eigenvalue (λ_3). The average of all three eigenvalues is the mean diffusivity (MD) [8].

7.2.5   Registration and VOIs

The registration paradigm included registration to a template brain. This template was generated by registering separate data sets of 35 three months-old male *Wistar* rats to each other. Then one average brain template was generated from these 35 registered data sets. Additionally, volumes of interest (VOIs) for several anatomical structures were manually created based on a rat brain atlas [9]. In the following, the VOIs of the cortex and the striatum are analyzed. All analysis used the brain volume represented by the series of coronal sections shown in Figure 7.1, where the volumes were conservatively selected to avoid errors at the boundaries of the acquired maps and thus in order to avoid an error in volume determination. The ROI "*whole brain*" was defined as the brain tissue limited caudally by the cerebellum and rostrally by the rhinal fissure, as demonstrated in the sagittal section scheme on Figure 7.2.

First, the 3M MRI dataset was registered to the template brain, then, the 2M and 6M data sets were registered to the 3M data set of each subject, the 1M MRI data

was registered to the 2M and the 3W data to that at 1M. Thus, data sets of all time points of each individual were registered step-by-step to the template brain starting with the data sets of the 3months old animals and propagating to the next-closest time point. Using the information provided by the deformation field (see below for details) for each registration step, the template VOIs were propagated from one time point to the next, thereby enabling quantitative comparison of corresponding areas. Subsequently, the VOIs were evaluated quantitatively for MRI parameter changes and for volume change.

All registration steps were carried out with the first echo (TE1) image of the MSME sequence (TR/TE=5,000ms/10ms), chosen for its high anatomical details and high signal-to-noise ratio (SNR). Individual brain masks were created (brain extraction tool in FSL) and applied during all steps of the registration process. The masks of all, the reference data set and the deforming data set, were used to crop the images to sections merely larger than the masks themselves to facilitate the registration steps of the brain. The quality and success of the registration process was controlled by visual inspection using a custom-made graphic user interface (GUI) [10].

Registration was performed in a coarse-to-fine process. Initial registration was accomplished with a rigid transformation for rough global alignment. Subsequently, an affine registration was conducted to compensate for brain size scaling during the animal's developmental growth. Finally, a non-rigid B-spline registration was applied to follow regional changes. A Gaussian image pyramid was employed in all registration steps, applying four resolutions for the rigid and affine and two for the B-spline part. Normalized correlation was used as a similarity metric. The registration was implemented using the open source image registration toolbox `elastix` [11]. Detailed information on the registration parameters can be found at the `elastix` website (http://elastix.bigr.nl/wiki/index.php/Par0020).

The absolute three-dimensional deformation, necessary for the registration of two data sets, is contained in the deformation matrix. The identical geometry of the DTI and MSME (thus also the TE1) data sets allowed us to apply these deformation matrices of the TE1 images in a second step to the parameter maps. The VOIs are then available for all parameter maps of all time points, thereby enabling not only the quantitative evaluation of the T_2 and diffusivity changes, but also the computation of brain structure volumes.

7.2.6   Cortical thickness determination

The mean cortical thickness was assessed by measuring the distance between external capsule/corpus callosum and dorsal brain surface. For this purpose, a semi-automated macro was implemented in ImageJ (version 1.46, NIH, Bethesda, MD; USA) measuring the cortex thickness perpendicular to a manually generated outline of the white matter. In this procedure the most medial part of the corpus callosum was excluded, because the assumption of a parallel cortex is not met in this region.

In detail, in a first step a "profile image" is created: A manually generated outline ("Segmented Line" tool in ImageJ) is used to fit a curve to the center of the corpus callosum using Gaussian combined with Heaviside step functions fits. Straight lines, perpendicular to this curve and reaching the cortical surface, form the "profile image", i.e. the curve is straightened. In a second step, the cortex thickness

is measured in the profile image by determining the length of the straight lines perpendicular to the curve crossing the cortex only. This distinction is achieved by submitting the grey scales in the profile image to a Rodbard fitting function. This procedure of cortex thickness determination was performed for the somatosensory cortex in 5–6 slices.
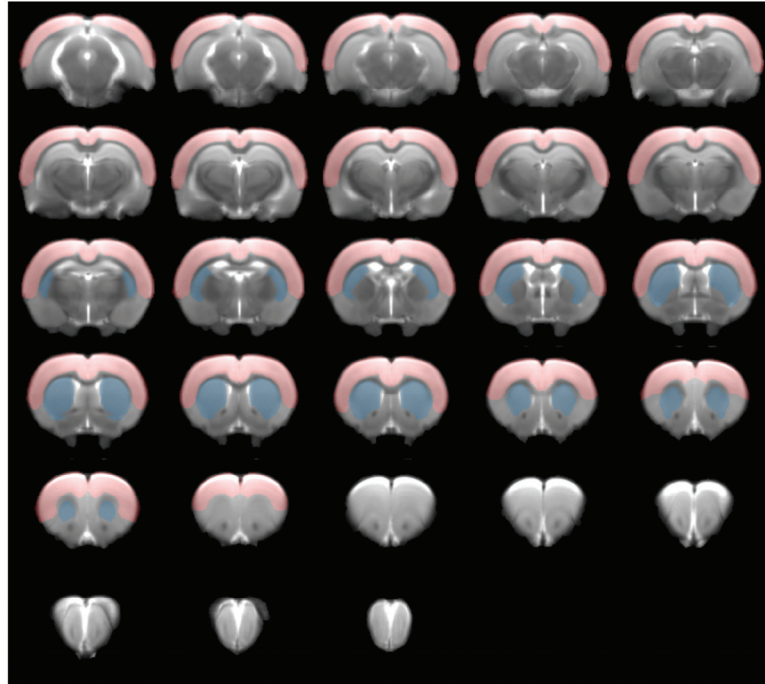

Figure 7.1 Template brain with regions of interest (ROIs). The template brain is an average MR image stack (TurboRARE) of a three months old rat brain (n=35 *Wistar* rats). The extent shown here from the onset of the cerebellum caudally (top left) to the rhinal fissure rostrally (right bottom) was defined as the *whole brain* ROI. Superimposed are the structural ROIs for cortex (red) and striatum (blue), both based on Paxinos and Watson rat brain atlas [9]

7.2.7 Histology

At 3W, 3M and 6M, animals were sacrificed by transcardial perfusion with phosphate buffered solution (PBS) and 4% paraformaldehyde (PFA). Brains were postfixed overnight in 4% PFA before treatment with 30% sucrose. Tissue sections of 40μm thickness were cut (Microtome, Leica Microsystems, Wetzlar, Germany) and preserved at -20°C for histological staining. Sections at six selected levels were stained for both myelin and for cell nuclei, using Black-Gold II (BGII) [12], and cresyl violet (CV), respectively (both: EMD Millipore, Billerica, MA, USA).

In order to assess the cell and myelin density in the brain, image acquisition and evaluation was conducted with a Keyence BZ9000 fluorescence microscope (Keyence, Neu-Isenburg, Germany) with a cell count analysis tool (Keyence). Quantification was based on contrast and color intensity in full-focus projections of images with 20x magnification (focal planes of 3μm). ROIs were chosen in multiple areas: four cortical ROIs per hemisphere, each, in 6 sections (48 in total) and three striatal ROIs per hemisphere, each, in three sections (18 in total). Relative myelin

content was defined as the relative area covered by BGII stained processes; cell density was determined as the number of CV stained cell nuclei per area.
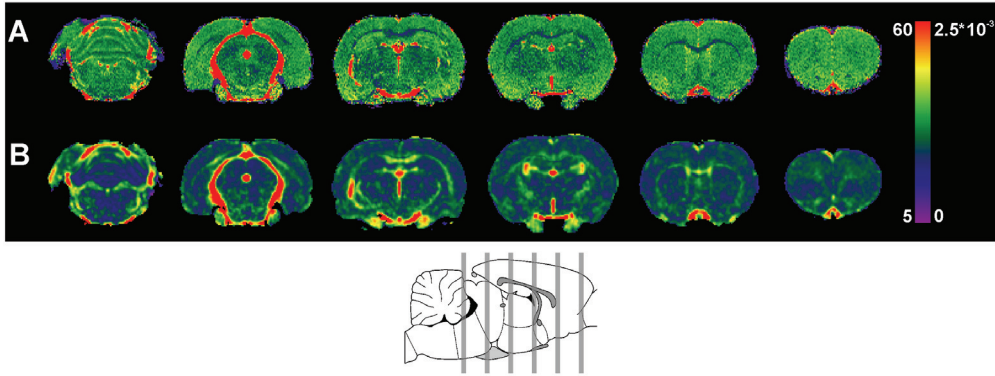
Figure 7.2 Magnetic Resonance data. Representative T_2 (A) and $\lambda_{||}$ (B) map of a 3M old animal, before registration to the template brain. Depicted is every 5th MR image of an acquired 30 slice-stack, grey lines in the rat brain sketch [9] below indicate their anatomical position

7.2.8 Statistics

Longitudinal MRI data was evaluated using repeated measures ANOVA (SPSS version 18, IBM Corp. Armonk, NY, USA) with a repeated within-subject design. Where Mauchly's test indicated that the assumption of sphericity was violated ($p < 0.05$), we report the results with Greenhouse-Geisser corrected (ε) degrees of freedom and significance levels. Post-hoc pairwise comparisons with Bonferroni test are reported for consecutive time points only, unless interpretation of supplementary comparisons was useful. Histological data was checked upon homogeneity of variances using Levene's test and analyzed with a one-way ANOVA with subsequent Bonferroni correction (SPSS). All data were expressed as standard error of the mean (SEM) unless otherwise stated.

7.3 Results

7.3.1 Volume changes during development

The brain undergoes a strong growth during the first postnatal months. This growth curve was found to be quite homogeneous across the eight animals examined in this study. The volume change is significant for all three VOIs (whole brain: $\chi^2(5)=16.7$ $p < 0.05$, $\varepsilon = 0.46$; $F(1.37, 9.6)=68.86$, $p < 0.001$; cortex: $F(3,21)=65.48$, $p < 0.001$; striatum $\chi^2(5)=18.3$ $p < 0.05$, $\varepsilon = 0.4$; $F(1.2, 8.4)=33.5$, $p < 0.001$). Whole brain volume (excluding cerebellum and olfactory bulb) increases from $1202.9 +/- 18.9$ mm^3 (SEM) to $1585.5 +/- 43.9$ mm^3 (SEM) (Figure 7.3A), thus gaining about 30% during the five weeks between postnatal week three and end of month two ($p < 0.001$). After 2M, brain volume is no longer changing significantly. Analyzing the cortical and striatal volumes separately, their volumetric plots (Figures 7.3B and C), both show a highly significant increase ($p < 0.001$) from 3W to 1M, a continuous growth from 1M to 2M ($p < 0.05$), and no significant change from 2M to 3M.
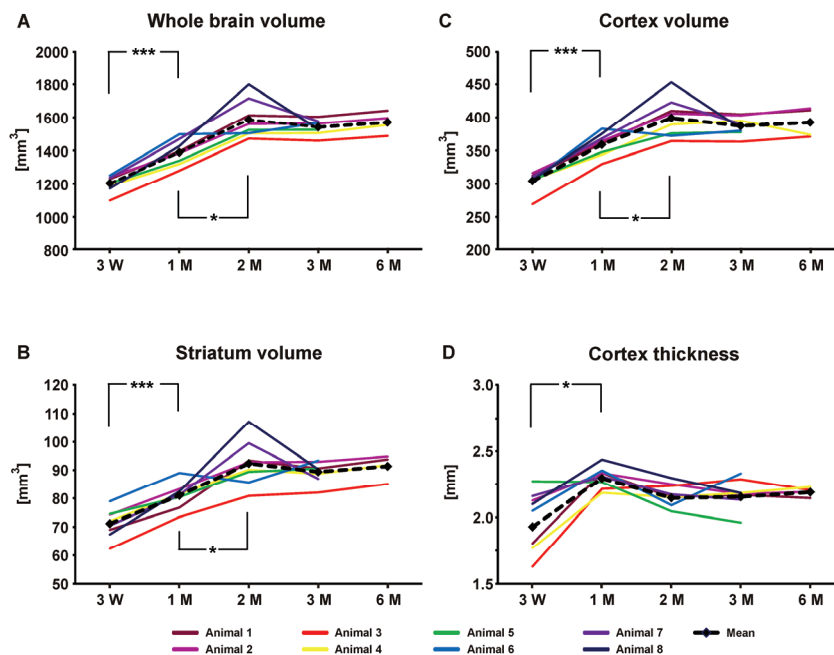
Figure 7.3 Individual volume changes of developing brain regions. The graphs show the absolute volume of the whole brain (A), the striatum (B) and cortex (C) and the cortical thickness (D) plotted against the age for each individual animal. Here and in subsequent figures, ages are given as follows: three weeks, one, two, three and six months: 3W, 1M, 2M, 3M and 6M respectively. Red/yellow lines represent animals #1–4, which were followed from 3W to 6M, blue/green lines indicate animals #5–8, followed from 3W to 3M of age; the broken black line indicates the mean value. Note, for this and subsequent figures statistical significance is indicated for consecutive time points only; significance levels are Bonferroni corrected and represented by * p<0.05, ** p<0.01 and *** p<0.001 and correspond in color to the respective data line

Separate to the strong volume growth of whole brain, cortex and striatum, the cortical thickness shows a different developmental growth pattern. The cortical thickness grows substantially and significantly between 3W and 1M (p<0.05), at which time it stabilizes already (Figure 7.3D) ($\chi^2(5)$=14.96 p<0.05, ε=0.43; F(1.29,9)=6.86, p<0.05).

7.3.2   Quantitative MRI parameter changes during development

Simultaneous with the dramatic volume changes, the quantitative MRI variables are changing. T_2 relaxation time of the whole brain, the cortex and the striatum decreases substantially and continuously in the time window between 3W and 2M (p<0.05 between 3W/1M and 1M/2M) with a statistically significant effect over time (whole brain: F(3,21)=28.84, p<0.001; cortex: F(3,21)=36.4, p<0.001; striatum: F(3,21)=30.6, p<0.001). After 2M, the T_2 decrease in the striatum levels out, while the T_2 values of cortex and whole brain are still decreasing until the age of six months (Figure 7.4A). Note that the T_2 decrease of the whole brain contains a contribution from shrinking relative ventricle volume, while the cortical and striatal T_2 decrease is primarily due to tissue reorganization processes.

The diffusion parameters axial ($\lambda_\parallel$), mean (MD), and radial diffusivity ($\lambda_\perp$) show a decrease during the first six months of cerebral development with a statistical effect over time (repeated measures ANOVA) in all three structures analyzed (Figures 7.4B–D). However, not all parameters show differences between subsequent time points (T-test).

$\lambda_\parallel$ evolves similarly in cortex and striatum, both in respect to the absolute values and the relative change over time. In both areas, $\lambda_\parallel$ shows a light but steady decrease during the first three months (cortex: $F_{(3,21)}=6.72$, $p<0.01$; striatum: $F_{(3,21)}=9.33$, $p<0.001$) followed by stagnation thereafter. Mean $\lambda_\parallel$ of the whole brain is slightly higher compared to the absolute values of cortex and striatum, but follows the same qualitative developmental pattern ($F_{(3,21)}=6.86$, $p<0.01$). None of the three structures shows a significant difference in $\lambda_\parallel$ between sequential time points, but they all show a difference between 3W and 3M ($p<0.05$).

MD values of the three VOIs tend to increase from striatum to cortex to whole brain (Figure 7.4C), though their qualitative development over time is alike and statistically significant in all three cases (Whole brain: $F_{(3,21)}=13.29$, $p<0.001$; Cortex: $F_{(3,21)}=9.1$, $p<0.001$, striatum: $F_{(3,21)}=19.13$, $p<0.001$). The first three time points until 2M show a slowly decreasing trend followed by a steep decline between 2M and 3M and a rather stable phase thereafter (i.e. 3M to 6M). Despite the qualitative similarity in the development, the cortical ROI did not show any significant changes between sequential time points.

$\lambda_\perp$ development with time is similar to MD, but here the cortical values are equal to or even higher than those of the whole brain. In all three VOIs, an effect of time was observed (whole brain: $F_{(3,21)}=11.69$, $p<0.001$; cortex: $F_{(3,21)}=6.72$, $p<0.01$; striatum: $F_{(3,21)}=21.23$, $p<0.001$) with a particularly strong $\lambda_\perp$ decrease between 2M and 3M. This difference was found to be significant in whole brain and striatum ($p<0.05$), while in the cortex, the $\lambda_\perp$ values at 3M significantly differ only from 3W and 1M ($p<0.01$) but not from 2M.

7.3.3   Histological analysis of developmental changes

Histological evaluation of the brains at different developmental stages revealed a pronounced increase in myelinated fibers on Black-Gold II staining during the first six months. This development was analyzed both qualitatively (Figure 7.5) and quantitatively (Figure 7.7A). The three-week young brains show positive staining only in the white matter structures, such as the corpus callosum, the anterior commissure, or fornix (Figure 7.5). At 3W, myelinated fibers are barely detectable in the cortex, their contribution to the tissue is as low as 1% (Figure 7.7A). By 3M, the radially oriented fibers of the cortex become myelinated to a high degree and cover about 15% of the cortex. At six months of age, the cortical layers can be recognized and at this time, 70% of the cortex is BGII+. The increase of cortical BGII+ area is apparent over time and found to be highly significant ($F_{(2,6)}=32,3$, $p<0.001$).

In the striatum changes are not as pronounced upon visual inspection. Quantitative analysis, however, reveals a strong increase in relative area covered with myelin ($F_{(2,6)}=33,4$, $p<0.001$). The white matter bundles of the striatum are already distinguishable at three weeks but make up only 5% of the area; with time they become more intensively stained and increase in numbers until, at three months,

they represent about 28% of the striatal area. Here, in contrast to the cortical maturation, a further increase from 3M to 6M was not observed.

No maturation change is noticeable by visual inspection of CV staining of animals of different ages (Figure 7.6). Quantitative analysis of cell density confirms this impression for the cortical but not for the striatal ROIs (Figure 7.7B). Cell density in the cortex remains stable over the course of the first six months of maturation, with no distinct differences between the single time points. In the striatum, however, cell density is decreasing between 3W and 3M, reaching a constant level thereafter ($F_{(2,6)}$= 25.3, p<0.01).
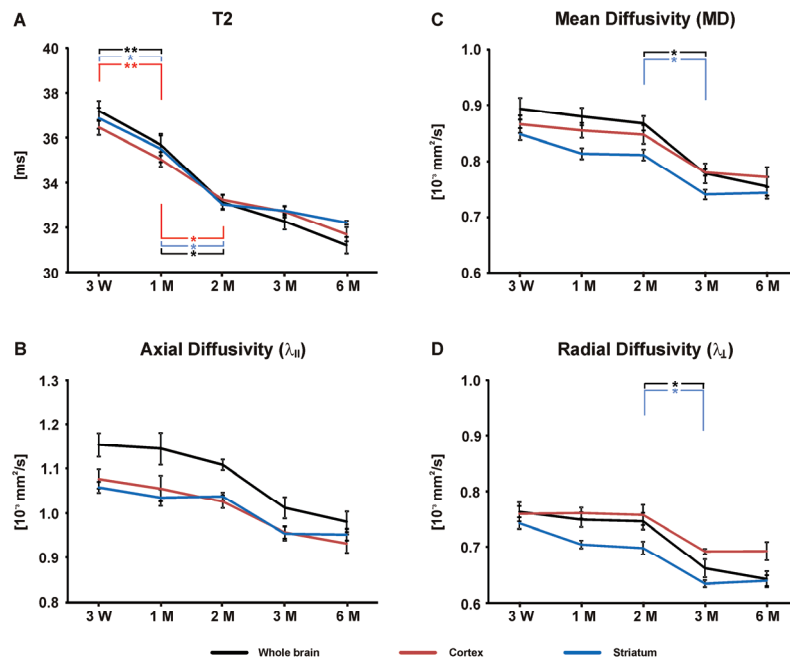

Figure 7.4 Quantitative MR parameters. Evolution of the mean T_2 (A), axial (B), mean (C) and radial diffusivity (D) over time are shown for the three regions of interest: whole brain (black), cortex (red) and striatum (blue). The data shown is an average of n=8 rats until 3M and n=4 rats at 6M of age with error bars indicating the standard error of the mean (SEM)

7.4   Discussion

This study combined a longitudinal and cross-sectional approach to monitor postnatal development in *Wistar* rats by noninvasive *in vivo* MRI and conventional histology. We have assessed the noninvasive *in vivo* biomarkers cerebral growth, tissue water and tissue structure by MRI relaxation time measurements, and tissue diffusion parameters together with *ex vivo* tissue myelination state and cell density. With these parameters, we have been able to characterize and define the time window of brain maturation in the male *Wistar* rat. This novel definition is of paramount importance for longitudinal studies of the rat brain when it is important to discriminate in which phase of development or maturation the subject under investigation is at the start of the study or during its runtime. We have shown in this study that the rat brain and especially the rat brain cortex are indeed not yet fully developed at 3 months of age. Furthermore, individual brain regions and

processes have been shown to have individual time scales for maturation. Based on these observations, we recommend careful examination of the brain structures under investigation before investigating functional topics or disease models in longitudinal examinations.
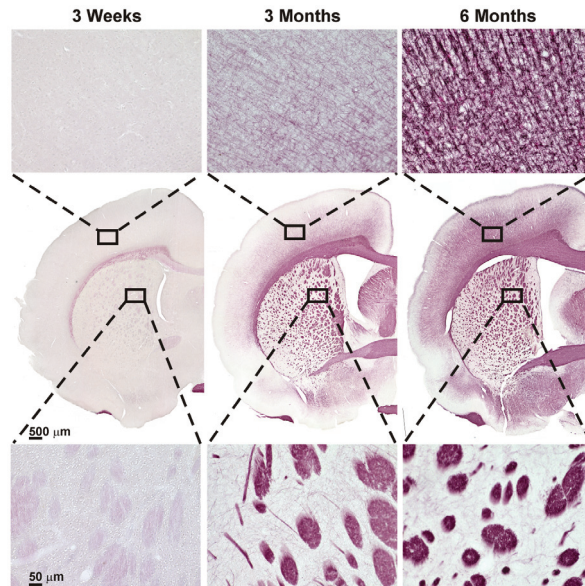
Figure 7.5 Histological evaluation of myelin content. Black-Gold II staining was used to visualize cerebral myelin content, representative brain sections of differently aged animals are pictured here from left to right: 3W, 3M, 6M. The middle row shows an overview (4x magnification) of one hemisphere with the position of the two close-ups indicated by the black squares: the upper row shows a ROI (20x) in the cortex, the lower row in the striatum
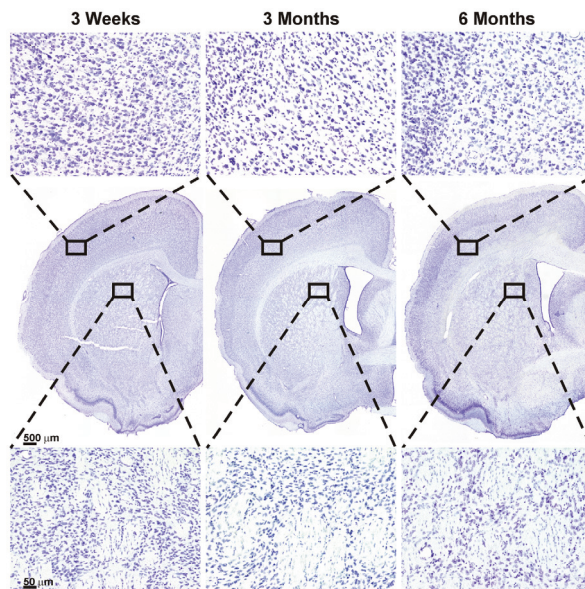
Figure 7.6 Histological evaluation of cell density. Cell density was assessed via cell counting in Cresyl Violet stained sections. Representative brain sections of differently aged animals are pictured here from left to right: 3W, 3M, 6M. The middle row shows an overview (4x magnification) of one hemisphere, the upper and lower row show the close-ups indicated by the black squares: the upper row a ROI (20x) in the cortex, the lower row in the striatum

7.4.1 *In vivo* MRI parameter patterns of brain maturation

When inspecting the *in vivo* data alone, different maturation time profiles become apparent. Changing MR parameters alone, however, do not allow conclusions about single microstructural processes. Yet, the combination of the different *in vivo* measurements in this study suggested cell density and myelination to be strongly responsible for changes in T_2 and diffusion, respectively. Additional histological tissue characterization can reveal such changes in microstructure with high sensitivity, thus permitting unambiguous interpretation of the MRI parameters. In the present study, two tissue properties were analyzed: the development of myelinated fibers was visualized with the well characterized Black-Gold II staining [12], while cell density was evaluated with Cresyl Violet, in order to detect neuronal as well as glial cell types.

Independent of ROI selection (whole brain, cortex or striatum), the first two months show continuous volume changes, accompanied by a dramatic T_2 decrease. This result of decreasing T_2 relaxation time with early growth is supported by an earlier study on postnatal rats in our group [13]. Judging from the T2WI-based volume data alone, one is tempted to believe that brain growth is completed by the end of two months. Interestingly enough, we have found that the quantitative parameter, T_2 relaxation time, continues to decrease beyond 2M, indicative that water content and/or tissue reorganization processes continue to change at a time when the brain volume has reached a mature state. This is in agreement with reports on dramatic decrease of brain water content with increasing gestational age in humans [14], while it continues to further decrease substantially during early development for many species, including rodents [15]. This T_2 decrease (as an indicator of brain water content decrease) may well be related to increasing myelination as a growing tissue compartment, consequently resulting in decrease of the extracellular space available for brain water.

Myelination as well as increased cell density, both decrease the amount of free water in the brain in favor of intracellular water compartmentation [16, 17]. This is in agreement with early neurochemical studies [18, 19, 20] which had reported that brain development is accompanied by a decreasing water content of the tissue and a constant increase of the myelin fraction. Indeed, our diffusion data show that the myelination process is not yet finished at 2M, again in agreement with the early reports describing ongoing myelination increases in healthy rats during their observation period of 52 days [19] and 70 days [18], respectively. Previous studies reported that during adolescence changes in DTI parameters reflect myelination, but during the neonatal period, they rather reflect changes in general water content and structure [21]. In our study, a pronounced decrease in the DTI parameters MD and $\lambda_\perp$ was found between 2M and 3M and reflects the dramatic change of the myelination status, confirmed by histology across the whole brain *ex vivo* between 3W and 3M (Figures 7.5 and 7.7). As discussed earlier in model systems, diffusion anisotropy integrates information on myelination state and on axonal structure [6, 7]. According to these authors, myelination changes are best represented by the radial diffusion tensor eigenvalue $\lambda_\perp$, while these changes have relatively little effect on the maximal eigenvalue $\lambda_\parallel$. Myelination acts like a restriction on radial free water mobility and, in consequence, leads to a reduced mean diffusivity, most clearly seen in a strong reduction in $\lambda_\perp$. This is in line with our MRI and histology results, showing that in the striatum with its strongly myelinated, big fiber bundles,

MD as well as $\lambda_\perp$ are reduced more strongly than in the cortex. The drop in $\lambda_\parallel$ observed here is probably a result of the general diffusivity reduction, rather than actual reduced axial weighting. Though the *ex vivo* data is available only for 3W and 3M, the high temporal resolution of the DWI data suggests that the major period of myelination is between 2M and 3M.
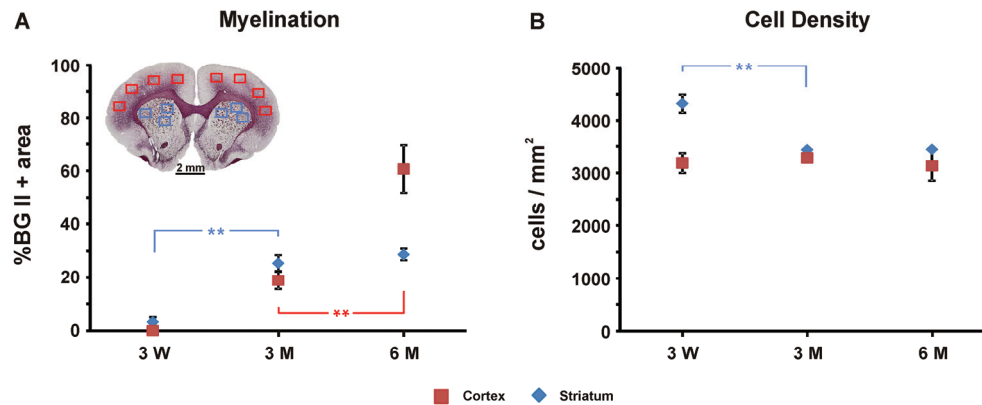
Figure 7.7 *Ex vivo* histological quantification. Quantification of the histological sections was performed on eight cortical and six striatal close ups with 20x magnification per section. A representative overview section (4x) is inserted in the upper left, with the 14 ROIs indicated by red (cortex) and blue (striatum) boxes. The relative BGII⁺ area reflects the extent of myelination (A), while cell density is assessed by the mean number of cells per mm² (B). Both graphs give the mean value for cortex (red) and striatum (blue) with error bars representing SEM (n=3)

When interpreting myelination, as assessed here by BGII staining, one must consider that staining intensity is not taken into account for the present quantification approach, thus denser packing in bundles is not represented in the evaluation. The strong myelination of the first three months is followed by rather subtle changes, observed both in staining intensity and stained area. In contrast to the DWI results, this is indicative that the brain is not completely developed at three months, thereby revealing the sensitivity limit of diffusion MRI.

In the following we discuss *in vivo* as well as *ex vivo* data of the different cerebral structures, followed by a recommendation for age-relevant brain studies.

7.4.2 Whole brain

The whole brain ROI shows higher MD and $\lambda_\parallel$ values and a stronger decrease over time, when compared to cortical and striatal ROIs. As the whole brain ROI includes all cerebral structures between olfactory bulb and cerebellum, it consists to a better part of white matter rich structures such as the hippocampus, the striatum, and the actual white matter. Thus, when interpreting the strong drop in diffusivity values with age, the major cause probably is myelination. As fluid compartments have the highest diffusivity, reduction in the relative size of the ventricles will further lower the mean diffusivity in the whole brain.

7.4.3 Cortex

The *ex vivo* and *in vivo* results for the cortical ROI suggest a rather complex maturation process. Most prominent is the apparent discrepancy between the evolution of cortical volume and of cortical thickness and of MRI diffusivity parameters and myelin content. These apparently contradicting findings reflect only different aspects of the same processes.

The cortical volume was found to increase until 2M, yet the cortex thickness has reached maximum already after 1M. These findings are in full accordance with *ex vivo* examination by Romand and colleagues, reporting a significant cortex increase along the long body axis between postnatal day 36 and 60 while thickness development already ended with postnatal day 36 [22]. Thus, the cortex reaches its final thickness after one month while rostral/caudal expansion of the brain continues until at 2M.

Interestingly, the cortical growth phase is not accompanied by changes in cell density; according to Mortera *et al.* [23] mainly neurogenesis, rather than gliagenesis accounts for the volume increase. With the volume increase, the T_2 is reducing strongly until 2M, showing a decreasing trend afterwards. Apparently this T_2 change is not due to a changing density of cells, but must emerge from other maturation processes. A reduced T_2, as well as MD can indicate a reduction of free water in the tissue [24], thus, decreasing the random movement of free water molecules and resulting in altered spin-spin interaction, the physical mechanism of T_2. Apart from myelination and higher cell density, the observed T_2 decrease may have several additional reasons coming from neuronal ramification and synaptogenesis, to simple compression and fine changes such as changing protein composition of the extracellular matrix. Especially the T_2 change beyond 3M, during growth stagnation and with major myelination processes terminated, reflects the high sensitivity of T_2 for tissue composition changes.

Our histological evaluation does not account for such processes of microscopic tissue composition alterations, so that *ex vivo* explanations for cortical T_2 changes are limited to the aspect of myelination. The BGII staining revealed a continued cortical myelination at least until 6M, contributing to reduction of extracellular space because of constant cell density. Although the radial organization increases pronouncedly on the BGII staining between 3M and 6M, this is not reflected on diffusion parameters. No decrease in either $\lambda_\perp$ or MD could be detected between these time points, indicating that further myelination after 3M was accompanied by other processes diminishing the radial diffusivity sensitivity. This diminishing diffusion sensitivity parallel to the ongoing myelination process may, at least in part, account for the apparent discrepancy between our results and earlier reports by Bockhorst and colleagues, reporting a decrease between postnatal day eight and 28, but no further change in cortical $\lambda_\parallel$, $\lambda_\perp$ or MD after postnatal day 28 [5]. Those earlier data may suffer from technical reduction of diffusion sensitivity: while we recorded our diffusion data at 11.7T, data by Bockhorst *et al.* were collected at 7T and needed more signal averaging, thus resulting in longer scan time, and, in consequence, making the images prone to movement artifacts which may lead to some blurring of the diffusion strength in the reconstructed quantitative parameter images. Support for such explanation comes from those authors reporting that the diffusion-weighted images needed to be warped to minimize image distortions induced by eddy currents. We therefore believe that our observations of diffusion

changes persisting until 3M are based on more robust and more sensitive raw data recording.

The cortical architecture features radial compartments, like the pyramidal axons and functional columns, and layers perpendicular to the radial compartments. From such well characterized cortices as the primary visual cortex, it is known that the radial organization of the pyramidal neurons is established prenatally, and that their processes mature within the first postnatal weeks [25]. This columnar/radial organization is not yet reflected in the histological staining, as the axons are not yet myelinated, but can be found in the DWI when inspecting the direction of the first eigenvector, $\lambda_{\parallel}$ [26]. With the maturation of the cortical layers and the branching of the neurons within, the distinct and homogeneous pattern of the eigenvector dissolves, becoming less regular with increasing age. Though the radial structure appears dominant in the BGII staining, the layering structure of the cortex seems to modulate the major λ values seen in the DWI data afterwards. Cell-dense layers like layer IV, rich on interneurons, branches and cross connections, will have a more restricted and less directed diffusion than layers with fewer cell bodies. Though the spatial resolution is not sufficient to illustrate these differences within the cortex, diffusion of water molecules could be deflected between layers rather than along the myelinated axons in some parts of the cortex and be generally reduced during the maturation of the cortical parenchyma.

7.4.4 Striatum

In the striatum the developmental time scale observed in DWI appears to be consistent with the myelination process visualized in histology, showing big fiber bundles on CV and BGII stained tissue sections. The significant volume growth until 2M and the increasing trend until 6M are accompanied by an antiparallel development of the T_2 values equivalent to those in the cortex and whole brain ROIs. The changes in diffusivity are manifested quite strongly until 3M, as the striatum is rich in white matter bundles stretching toward the internal capsule. Histological assessment shows that in the same time frame, until 3M, cell number and myelin content of the striatum are changing remarkably and stabilize thereafter. Cell density is decreasing between 3W and 3M, maybe due to both, the striatal growth (until 2M) and the volume demanding myelination process. The strong myelination is reflected in the decrease of radial and mean diffusivity between 2M and 3M. At three months, however, all processes seem to be terminated and the striatal tissue has completely matured.

7.4.5 Consequences for investigations on cerebral disease models

Many studies on cerebral diseases are based on the assumption of inducing the disease or lesion on healthy and adult animals. There is, however, a wide body of literature on such disease model investigations using rats of body weight ranging between 270 and 320 g. According to standard weight-age diagrams provided by the animal suppliers for the strain of *Wistar* rats used in the present study, this weight range makes the animals typically around two months old, at any rate clearly younger than 3 months of age. In this case, volume change and cortical thickness have already stabilized, cell density in the striatum has also stabilized but myelination in both, striatum and cortex, continues up to 3M for striatum, for cortex even up to 6M. Based on the diffusion changes alone, myelination changes are very pronounced between month two and three. Taken these new observations

together, it must be cautioned that lesion studies during this age period may be influenced by ongoing developmental brain maturation processes. This situation may be even more complex in the case of studies dealing with evaluation of therapeutic strategies. In light of our new observations, it would therefore be preferable to perform such disease model investigations (including those on therapeutic evaluations) on *Wistar* rats being at least three months of age at the beginning of the investigations.

Future studies will increase the temporal resolution of the maturation and growth changes to even better define the end of the developmental phase. Improvement of spatial resolution of the MRI will permit detailed analysis of structures prone to contain partial volume effects, such as corpus callosum or ventricular spaces, and will extend the whole volume to include hindbrain and olfactory bulb.

7.5 Conclusions

Combining longitudinal MRI measurements with histological tissue characterization, we have derived a temporal profile of postnatal rat brain maturation. Different cerebral structures show an individual timeline for postnatal development. While the striatum seems to be fully matured by three months, the cortex is still changing until at least six months. Our present results convincingly demonstrate that brain volume is a reliable variable of having reached a steady state situation concerning organ expansion while measurement of cortical thickness will be misleading for two to three months old rats. Clear indications of ongoing developmental changes in the rat brain point to the time window until three months of age; in particular persistent myelination aspects in cortex and striatum make it advisable to speak of "adult animals" only from three months of age on. Future investigations on disease models or lesions may have to consider this age of three months as a safer threshold to avoid ongoing developmental changes in the brain opposing the study of the patho-mechanisms of interest.

Acknowledgments

References

[1]. Meaney M. J. and Stewart J. *A descriptive study of social development in the rat (Rattus norvegicus)* Anim Behav 29: 34–45 1981

[2]. Spear L. P. and Brake S. C. *Periadolescence: Age-dependent behavior and psychopharmacological responsivity in rats* Dev Psychobiol 16: 83–109 1983

[3]. Andersen S. L. *Trajectories of brain development: point of vulnerability or window of opportunity?* Neurosci and Biobehav R 27: 3–18 2003

[4]. Spear L. P. *The adolescent brain and age-related behavioral manifestations* Neurosci and Biobehav R 24: 417–463 2000

[5]. Bockhorst K. H., Narayana P. A., Liu R. *et al. Early postnatal development of rat brain: In vivo diffusion tensor imaging* J Neurosci Res 86: 1520–1528 2008

[6]. Deo A. A., Grill R. J., Hasan K.M. *et al. In vivo serial diffusion tensor imaging of experimental spinal cord injury* J Neurosci Res 83: 801–810 2006

[7]. Song S. K., Sun S. W., Ramsbottom M. J. *et al. Dysmyelination revealed through MRI as increased radial (but unchanged axial) diffusion of water* Neuroimage 17: 1429–1436 2002

[8]. Basser P. J., Mattiello J. and Lebihan D., *Estimation of the effectiive self-diffusion tensor from the NMR spin-echo* J Magn Reson Ser B 103: 247–254 1994

[9]. Paxinos G. and Watson C. *The rat brain in stereotaxic coordinates* 4th edn. Academic Press, San Diego, CA 1998

[10]. Khmelinskii A., Mengler L., Kitslaar P. *et al. A visualization platform for high-throughput, follow-up, co-registered multi-contrast MRI rat brain data* Proc SPIE Medical Imaging 8672: 86721W–86721W-7 2013

[11]. Klein S. and Staring M., Murphy K. *et al. elastix: a toolbox for intensity based medical image registration* IEEE T Med Imaging 29(1): 196–205 2010

[12]. Schmued L., Bowyer J., Cozart M. *et al. Introducing Black-Gold II, a highly soluble gold phosphate complex with several unique advantages for the histochemical localization of myelin* Brain Res 1229: 210–217 2008

[13]. Kallur T., Farr T. D., Boehm-Sturm P. *et al. Spatio-temporal dynamics, differentiation and viability of human neural stem cells after implantation into neonatal rat brain* European J Neurosci 34: 382–393 2011

[14]. Hüppi P. S. and Dubois J. *Diffusion tensor imaging of brain development* Semin Fetal Neonat M 11: 489–497. 2006

[15]. Samorajski T. and Rosten C. *Age and Regional Differences in the Chemical Composition of Brains of Mice, Monkeys and Humans* Prog Brain Res: Neurobiological Aspects of Maturation and Aging Elsevier 253–265 1973

7

[16].   Anderson A. W., Xie J., Pizzonia J. *et al. Effects of cell volume fraction changes on apparent diffusion in human cells* Magn Reson Imaging 18: 689–695 2000

[17].   Chabert S. and Scifo P. *Diffusion signal in magnetic resonance imaging: Origin and interpretation in Neurosciences* Biol Res 40: 385–400 2007

[18].   Fuller G. N., Divakaran P. and Wiggins R. C. *The effect of postnatal caffeine administration on brain myelination* Brain Res 249: 189–191 1982

[19].   Lancaster F. E., Philipps S. M., Patsalos P. N. *et al. Brain myelination in the offspring of ethanol-treated rats: in utero versus lactational exposure by crossfostering offspring of control, pairfed and ethanol-treated dams* Brain Res 309: 209–216 1984

[20].   Norton W. T. and Poduslo S. E. *Myelination in rat brain: Changes in myelin composition during brain maturation* J Neurochem 21: 759–773 1973

[21].   Wozniak J. R., Lim K. O. *Advances in white matter imaging: A review of in vivo magnetic resonance methodologies and their applicability to the study of development and aging* Neurosci Biobehav R 30: 762–774 2006

[22].   Romand S., Wang Y., Toledo-Rodriguez M. *et al. Morphological development of thick-tufted layer V pyramidal cells in the rat somatosensory cortex* Front Neuroanat 5 2011

[23].   Mortera P. and Herculano-Houzel S. *Age-related neuronal loss in the rat brain starts at the end of adolescence* Front Neuroanat 2012

[24].   Whittall K. P., Mackay A. L., Graeb D. *A. et al. In vivo measurement of T2 distributions and water contents in normal human brain* Magn Reson Med 37: 34–43 1997

[25].   Miller M. W. *Maturation of rat visual cortex. III. Postnatal morphogenesis and synaptogenesis of local circuit neurons* Dev Brain Res 25: 271–285 1986

[26].   Hoehn-Berlage M., Eis M. and Schmitz B. *Regional and directional anisotropy of apparent diffusion coefficient in rat brain* NMR in Biomed 12: 45–50 1999

Chapter 8

Summary and conclusions

In pre-clinical research, whole-body small animal imaging is widely used for the *in vivo* visualization of functional and anatomical information to study cancer, neurological and cardiovascular diseases and help with a faster development of new drugs. Functional information is provided by imaging modalities such as PET, SPECT and specialized MRI. Structural imaging modalities like radiography, CT, MRI and ultrasound provide detailed depictions of anatomy. Optical imaging modalities, such as BLI and near-infrared fluorescence imaging offer a high sensitivity in visualizing molecular processes *in vivo*. The combination of these modalities enables to follow the subject(s) and molecular processes in time, in living animals.

With these advances in image acquisition, the problem has shifted from data acquisition to data processing. The organization, analysis and interpretation of this heterogeneous whole-body imaging data has become a demanding task.

In this thesis, the data processing approach depicted in Figure 1.1 was further explored. This approach is based on an *articulated* whole-body atlas as a common reference to normalize the geometric heterogeneity caused by postural and anatomical differences between individuals and geometric differences between imaging modalities. Mapping to this articulated atlas has the advantage that all the different imaging modalities can be (semi) automatically registered to a common anatomical reference; postural variations can be corrected, and the different animals can be scaled properly while allowing for proper management of this high-throughput whole-body data.

In this thesis, we have focused on three complementary aspects of the approach described in Figure 1.1, and worked towards an automated analysis pipeline for quantitative small animal image analysis. The specific goals of this thesis were:

(i)   to further generalize the articulated atlas-based registration method to the multi-modality component of the global approach presented in Figure 1.1, focusing on SPECT and MRI whole-body mouse data

(ii)   to expand the Articulated Planar Reformation algorithm by linking it to recently introduced resolution-enhancing MR reconstruction techniques which enable "zooming in" on small anatomical details not detectable with conventional MRI

(iii)   to prove the added value of atlas-based analysis of multi-modal follow-up data in a life-science study of the ageing processes in the brain, with a specific focus on multi-contrast MR rat brain data

In **Chapter 2** we introduced three realistic, articulated skeleton phantoms derived from publicly available small animal atlases. A number of application examples using the MOBY atlas for such articulated atlases were presented. Mainly, it was demonstrated that articulated atlases can be used in correcting the postural variation, in referencing optical to CT data and in organ approximation. By combining the atlas with the hierarchical anatomical model and articulated registration, whole-body skeleton registration could be performed robustly, even in the presence of large postural variations.

The presented articulated models formed the basis of the methodology presented in Chapters 3, 4 and 5 and were made publicly available.

In **Chapter 3,** we demonstrated the feasibility of the articulated atlas-based skeleton segmentation approach combined with the articulated planar reformation algorithm for whole-body mouse bone imaging using SPECT.

Quantitative evaluation was performed by calculating the Euclidian point to surface distance between the registered atlas and the correspondent CT dataset. The obtained mean distance of 2.6 ± 2.2 voxels, showed that the registration accuracy for the SPECT data is of the same order as the previously published results for μCT, 1.8 ± 0.1 voxels [1]. The large difference in the standard deviation between the μCT fittings results and the ones presented in this paper might be due to the variable nature of the SPECT data (tracer uptake and distribution, where the tracer targets the bone growth and not the entire bone and partial volume effect) versus the more robust bone contrast in CT. Due to these factors the extraction of the skeleton out of the data may result in either a partial or a much thinner or thicker skeleton than as seen in the μCT. By collecting data from several different imaging studies, one of the goals of this study was to demonstrate the robustness of the atlas-based segmentation with respect to the different whole-body SPECT scan settings. Depending on the research question, the amount of injected tracer, the pinhole size and scan time a trade-off has to be chosen between resolution and signal. However, as long as a skeleton estimation is possible the approach presented here holds.

In [1], it was demonstrated that the proposed atlas-based segmentation method is robust with respect to osteolytic bone defects. Here, it was demonstrated, that the use of the articulated mouse atlas, with defined DoFs and size restrictions for each bone, proved to be robust for "incomplete" data (*i.e.:* images where large bits of limbs are missing). It also proved to be relatively insensitive to non-relevant objects still present in the image the skeleton extraction, like kidneys, bladder, some lung and liver. The proposed approach effectively compensated for the large variations in posture that existed within the data and yielded segmentation results requiring minimal user input. These were of satisfactory quality for the ensuing mapping of the data to the standard reference and side-by-side visualization. Applying the APR algorithm to multi-modal cross-sectional data proved to be useful to provide proper referencing and visualization for an intuitive exploration and comparison of whole-body μCT, SPECT data.

In **Chapter 4,** a semi-automated atlas-based organ approximation method for μMRI mouse data was proposed. A manually extracted set of joint & bone landmarks and the automatically extracted skin were used to determine skin correspondences, which in turn were used for a Thin-Plate Spline approximation of major organs (heart, lungs, liver, spleen, stomach, kidneys). The obtained results were generally satisfactory and similar to the manual segmentations for heart, kidneys, liver, while for other organs the atlas approximations are more variable (organs with inherent shape variability such as the stomach and spleen), and errors were larger. The calculated Dice coefficients reveal "moderate" (0.41–0.6 [2]) performance for the lungs and mostly "substantial" (0.61–0.80) or "excellent" (>0.7 [3]) performance for heart, liver, and kidneys. The comparison of the calculated Dice coefficients with previously published results shows that while performing better than [4] and at a similar level as [5], the proposed method does not obtain as good results for the lungs as the method proposed in [6] (see Table 4.1). However, the example given in Figure 4.4 reveals that the proposed TPS

8

mapping of the mouse major organs leads to a realistic approximation and can be used by biologists for qualitative anatomical referencing.

In **Chapter 5,** we introduced local super-resolution reconstruction (SRR) in whole-body MRI and validated its feasibility for improving visualization of tumors in small animal imaging studies. We combined a number of state-of-the-art image processing techniques in the areas of articulated atlas-based segmentation of whole-body small animal data and planar reformation to create local volumes of interest for subsequent SRR reconstruction. The approach was validated in two case studies involving CT, BLI and MRI data of bone and kidney tumors in a mouse model. Using only a few low-resolution images, and a total acquisition time compatible with *in vivo* experiments, we have produced SRR MR images from which detailed information about the metastases can be inferred. This cannot be obtained from direct MR acquisition within a feasible acquisition time. We showed that local SRR MRI is an excellent complementary imaging modality in the description of tumor metastases, and provides a high-resolution alternative to conventional MRI.

An additional point to be made is the possibility to use BLI with SRR-MRI as an alternative for the CT anatomical reference, particularly in longitudinal studies where the repeated exposure to radiation in a CT scan may become a confounding factor or cause adverse effects [7].

Chapters 6 and 7 were dedicated to an explorative study of juvenile development and ageing processes of the brain. In **Chapter 6** an intuitive and easy to use, dedicated visualization and side-by-side exploration tool for heterogeneous, co-registered multi-contrast, follow-up cross-sectional MRI data was built. The deformation field, which results from the registration step, was used to automatically link the same voxel in the displayed datasets of interest. Its determinant of the Jacobian (detJac) was used for a faster and more accurate visual assessment and comparison of brain deformation between the follow-up scans. This was combined with an efficient data management scheme. We investigated the functionality and the utility of our tool in the neuroimaging research field by means of a case study evaluation with three experienced domain scientists, using longitudinal, cross-sectional multi-contrast MRI rat brain data. Based on the performed case study evaluation we concluded that the proposed tool improves the visual assessment of high-throughput data and can further assist in guiding quantitative studies.

Longitudinal studies on brain pathology and assessment of therapeutic strategies rely on a fully matured adult brain to exclude confounds of cerebral developmental changes. Thus, knowledge about onset of adulthood is indispensible for discrimination of developmental phase and adulthood. In **Chapter 7,** by combining longitudinal MRI measurements with histological tissue characterization, a temporal profile of postnatal brain maturation was derived. Different cerebral structures showed an individual timeline for postnatal development. While the striatum seemed to be fully matured by three months, the cortex was still changing until at least six months. The presented results convincingly demonstrated that brain volume is a reliable variable of having reached a steady state situation concerning organ expansion while measurement of

cortical thickness is misleading for two to three months old rats. Clear indications of ongoing developmental changes in the rat brain pointed to the time window till three months of age; in particular, persistent myelination aspects in cortex and striatum made it advisable to speak of "adult animals" only from three months of age onwards. Future investigations on disease models or lesions will have to consider this age of three months as a safe threshold to avoid ongoing developmental changes in the brain opposing the study of the patho-mechanisms of interest.

Based on the results presented in this thesis, it can be concluded that all the formulated goals have been achieved to a certain extent. However, there is quite some room for improvement and extension of this work in the future. In **Chapter 2** the strategy applied to make the atlases articulated was outlined to deal with major postural variations (involving long bones or large bone complexes); however, it can be extended to the whole skeleton to cope with smaller anatomical variations. For example, one can define a kinematic model for each vertebra of the columna vertebralis (whereas here the columna vertebralis is defined as a single bone complex) and even to some non-rigid organs.

Chapter 3 describes a segmentation approach that was developed to cope with a scenario when a combined whole-body SPECT/CT bone scan is not always desired or available. Thus, one of the limitations of the proposed approach is the fact that the skeleton should exhibit sufficient image contrast, *i.e.,* direct application of the atlas fitting to SPECT data requires tracer uptake in the skeleton. When that is not the case, this limitation can be overcome by applying the fitting directly to the provided whole-body anatomical CT scan and then propagating the CT-fitted model to the SPECT data. Furthermore, when the method is applied to SPECT directly and correspondent CT data is not available this method requires (minimal) user input during the extraction of the skeleton out of the data. When CT whole-body data is available, this kind of user input is not required anymore, as shown and extensively validated in [1]. The approach presented here can be applied to other animals, provided there is an adequate atlas.

Chapter 4 presented a first step towards an articulated atlas-based skeleton and organ mapping for MRI data, still requiring extensive user interaction to identify the joint rotation centers. Further automation of the atlas fitting process could be achieved for example by applying atlas-based non-rigid registration, using mutual information as a similarity metric.

The results presented in **Chapter 5** represent a pilot study towards interactive super-resolution reconstruction in post mortem image data. However, we have well-founded reasons to believe that our results translate to *in vivo* imaging. Especially SRR is expected to be most successful for relatively rigid structures, such as the brain, bone tissue, and tissue surrounding bone: cases in which rigid registration will yield accurate alignment of the low-resolution images.

The interactive approach to locally reconstruct VOIs presented here, allows overcoming the time and memory limitations of the SRR techniques in large VOIs. However, as shown in Table 5.1, the mean time for the best quality SRR result, *i.e.,* using 4 low-resolution images, is still in the order of minutes—91.3 s. These results are still far from the real-time target for this approach. A re-implementation of the

8

algorithm in a C/C++ and GPU programming environment combination might improve these results.

Apart from oncology, the presented work flow may be of value in many research areas that requires whole body examination for local ((sub-) slice-thickness sized) effects. Examples are the homing of labeled stem cells after systemic injection, or imaging of systemic inflammatory diseases.

The platform for intuitive, integrated visualization and exploration for high-throughput co-registered multi-modal, cross-sectional follow-up data presented in **Chapter 6** would strongly benefit if combined with an image registration package such as `elastix` and features that would allow drawing and performing quantification on ROIs or other user-input templates. The presented tool, will be made publicly available for download via www.lkeb.nl

References

[1]. Baiker M., Milles J., Dijkstra J. *et al. Atlas-based whole-body segmentation of mice from low-contrast micro-CT data* Med Image Anal 14(6): 723–737 2010

[2]. Landis J. R. and Koch G. G. *The measurement of observer agreement for categorical data* Biometrics 33(1): 159–174 1977

[3]. Bartko J. J. *Measurement and reliability: statistical thinking considerations* Schizophrenia Bulletin 17(3): 483–489 1991

[4]. Chaudhari A. J., Joshi A. A., Darvas F. *et al. A method for atlas-based volumetric registration with surface constraints for optical bioluminescence tomography in small animal imaging* Proc SPIE Medical Imaging 6510 Part 2: 651024 2007

[5]. Joshi A. A., Chaudhari A. J., Shattuck D. W. *et al. Posture Matching and Elastic Registration of a Mouse Atlas to Surface Topography Range Data* Proc IEEE Intl Symp on Biomedical Imaging 366–369 2009

[6]. Baiker M., Dijkstra J., Que I. *et al. Organ approximation in μCT data with low soft tissue contrast using an articulated whole-body atlas* Proc IEEE Intl Symp on Biomedical Imaging 1267–1270 2008

[7]. Hindorf C., Rodrigues J., Boutaleb S. *et al. Total absorbed dose to a mouse during microPET/CT imaging* Eur J Nucl Med Mol Imaging 37: S274 2010

Samenvatting en conclusies

Voor de *in vivo* visualisatie van functionele en anatomische informatie wordt in preklinisch onderzoek veel gebruik gemaakt van het afbeelden van het hele lichaam van diermodellen. Hiermee kunnen ziektes zoals kanker, neurologische en cardiovasculaire ziekten worden bestudeerd, met als doel het sneller ontwikkelen en testen van nieuwe medicaties. Functionele informatie kan worden verkregen met beeldmodaliteiten zoals PET, SPECT en speciale MRI sequenties. Structurele beeldmodaliteiten zoals röntgenfotografie, CT, MRI en ultrageluid geven gedetailleerde afbeeldingen van de anatomie. Optische afbeeldingsmodaliteiten, zoals BLI en nabij-infrarood fluorescentie imaging leveren een hoge sensitiviteit als het gaat om het afbeelden van moleculaire processen. Door deze modaliteiten te combineren wordt het mogelijk om zowel het subject als zijn moleculaire processen te volgen in de tijd, in levende dieren.

Door de snelle ontwikkelingen in beeldacquisitie is de verwerking van al deze data een groeiend probleem. De organisatie, analyse en interpretatie van deze heterogene whole-body imaging data is een veeleisende taak geworden.

In dit proefschrift is een nieuwe opzet voor dataverwerking van pre-klinische imaging studies onderzocht, zoals die afgebeeld in Figuur 1.1. Deze benadering is gebaseerd op een gearticuleerd atlas van een compleet lichaam, als een gemeenschappelijke referentiekader om de geometrische heterogeniteit te normaliseren, die wordt veroorzaakt door de posturele en anatomische verschillen tussen individuen en de geometrische verschillen tussen beeldmodaliteiten. postuurvariaties kunnen worden gecorrigeerd, en verschillen tussen dieren kunnen navenant geschaald worden; hierdoor wordt een coherente analyse mogelijk van deze high-throughput data van het complete lichaam.

In dit proefschrift hebben we ons gericht op drie complementaire aspecten van de benadering zoals beschreven in Figuur 1.1, en hebben we een geautomatiseerde analyse pipeline ontwikkeld voor de kwantitatieve analyse van kleine dieren. De specifieke doelen van dit proefschrift waren:

(i)   Het verder generaliseren van de gearticuleerde atlas-gebaseerde registratiemethode naar de multimodale component van de globale benadering zoals beschreven in Figuur 1.1, gefocusseerd op SPECT en MRI data van de gehele muis

(ii) Het uitbreiden van het "Articulated Planar Reformation" algoritme door het te verbinden met een recent geïntroduceerde MR reconstructie techniek die de beeldresolutie verhoogt. Dit maakt het mogelijk om in te zoomen op kleine anatomische details die niet zichtbaar zijn met conventionele MRI

(iii) Het aantonen van de toegevoegde waarde van atlas gebaseerde analyse van multimodale follow-up data in een biologische studie naar verouderingsprocessen in het brein, met een speciale focus op multi-contrast MR rat brein data

In **Hoofdstuk 2** hebben we drie realistische gearticuleerde skelet fantomen beschreven, die zijn afgeleid van publiek beschikbare atlassen van diermodellen. Een aantal voorbeeldtoepassingen werden gepresenteerd, die gebruik maken van de MOBY gearticuleerde atlas. Hiermee hebben we aangetoond dat gearticuleerde atlassen gebruikt kunnen worden voor de correctie van posturele variaties, bij de gecombineerde analyse van optische en CT data en in de benadering van orgaan

locaties. Door de atlas te combineren met een hiërarchisch anatomisch model en gearticuleerde registratie, was het mogelijk om compleet-lichaam skelet registratie robuust uit te voeren, zelfs in de aanwezigheid van grote posturele variaties.

De in Hoofdstuk 2 gepresenteerde gearticuleerde modellen vormden de basis van de methodes gepresenteerd in de Hoofdstukken 3, 4 en 5 en zijn publiek beschikbaar gemaakt.

In **Hoofdstuk 3** toonden we de haalbaarheid aan van een techniek voor skelet segmentatie in SPECT beelden op basis van het gearticuleerde atlas, in combinatie met het "articulated planar reformation" algoritme voor whole-body skeletimaging.

Kwantitatieve evaluatie werd gedaan door het berekenen van de Euclidische punt-vlak afstand tussen de geregistreerde atlas en de corresponderende CT dataset. De aldus verkregen gemiddelde afstand van 2.6 ± 2.2 voxels liet zien dat de nauwkeurigheid van de registratie voor de SPECT data van dezelfde orde is als eerder gepubliceerde resultaten voor μCT, nl. 1.8 ± 0.1 voxels [1]. Het grote verschil in standaard deviatie tussen de μCT resultaten en die gepresenteerd in dit artikel zou kunnen liggen aan de grotere variabiliteit in de SPECT data (tracer absorptie en verdeling, waar de tracer is gericht op bot groei en niet op het gehele bot, en partieel-volume effecten) versus het meer robuuste bot contrast in CT. Door deze factoren zou de extractie van het skelet uit de data kunnen resulteren in of een gedeeltelijk of een veel dunner of dikker skelet dan waargenomen in de μCT. Door data te verzamelen uit verschillende imaging studies, was een van de doelen van deze studie om de robuustheid aan te tonen van de atlas-gebaseerde segmentatie met betrekking tot de verschillende SPECT scan afstellingen. Afhankelijk van de onderzoeksvraag, de hoeveelheid geïnjecteerde tracer, de pinhole grootte en scantijd, moet er een compromis gesloten worden tussen resolutie en signaal. Desalniettemin, zolang er een skeletschatting mogelijk is, kan de gepresenteerde methodologie worden toegepast.

In [1] werd gedemonstreerd dat de voorgestelde atlas-gebaseerde segmentatiemethode robuust is met betrekking tot osteolytische laesies. Hier hebben we laten zien dat het gebruik van de gearticuleerde muis atlas, met gedefinieerde vrijheidsgraden en beperkingen op de grootte van elk bot, robuuster bleek te zijn voor incomplete data (bijv. beelden waar grote delen van de ledematen missen). De voorgestelde benadering compenseerde effectief voor de grote variaties in houding die aanwezig waren in de data, en gaf segmentatieresultaten die minimale gebruikersinterventie nodig hadden. De resultaten waren van voldoende kwaliteit om de data naar de referentie standaard te projecteren voor een zij-aan-zij visualisatie. De toepassing van het APR algoritme op de multi-modale cross-sectionele data bleek nuttig voor vergelijkende visualisatie ten behoeve van een intuïtieve inspectie en vergelijking van whole-body μCT en SPECT data.

In **Hoofdstuk 4** werd een semiautomatische atlas-gebaseerde approximatie methode voorgesteld voor μMRI muis data. Een manueel geëxtraheerde verzameling van gewrichts- en botpunten en de automatisch geëxtraheerde huid werden gebruikt om correspondentie op de huid te bepalen, die vervolgens werden gebruikt voor de "Thin-Plate Spline" benadering van de locatie van de belangrijkste organen (hart, longen, lever, milt, maag, nieren). De behaalde resultaten waren vergelijkbaar met de manuele segmentatie voor het hart, de nieren en de lever, terwijl voor de andere organen de atlas benaderingen meer varieerden (organen met intrinsieke vorm variabiliteit zoals de maag en milt), en met grotere fout. De berekende Dice coëfficiënten laten gemiddelde overeenkomsten (0.41–0.60 [2])

zien voor de longen, en meestal substantiële (0.61–0.80) of excellente (> 0.7 [3]) prestaties voor hart, lever en nieren. De vergelijking van de berekende Dice coëfficiënten met eerder gepubliceerd resultaten van anderen laat zien dat hoewel beter presterend dan [4] en op een vergelijkbaar niveau als [5], de voorgestelde methode minder goede resultaten voor de longen behaalt als de methode in [6] (zie Tabel 4.1). Desalniettemin, het voorbeeld in Figuur 4.4 laat zien dat de voorgestelde TPS mapping van de belangrijkste organen tot een realistische benadering leidt en gebruikt kan worden door biologen als kwantitatief anatomisch referentiekader.

In **Hoofdstuk 5** werd een een lokale Super-Resolutie Reconstructie (SRR) in MRI van het hele lichaam beschreven, en werd gevalideerd in hoeverre tumoren beter zichtbaar kunnen worden gemaakt met behulp van deze techniek. We combineerden een aantal state-of-the-art beeldverwerkingstechnieken op de gebieden van gearticuleerde atlas-gebaseerde segmentatie van whole-body data van kleine dieren en van "planar reformation", om lokale interessegebieden te bepalen voor de daaropvolgende SRR. De benadering werd gevalideerd in twee case studies met betrekking tot CT, BLI en MRI data van bot- en niertumoren in een muismodel. Gebruikmakend van slechts twee laag-resolutie beelden, met een totale acquisitietijd vergelijkbaar met *in vivo* experimenten, konden we SRR MR beelden produceren met meer detailinformatie over kleine metastasen. Dit kan niet worden verkregen uit een directe MR acquisitie binnen een uitvoerbare acquisitietijd. We hebben laten zien dat lokale SRR MRI een excellente aanvullende imaging modaliteit is voor de beschrijving van tumor metastases, en een hoog-resolutie alternatief verschaft voor conventionele MRI.

Een bijkomend punt is de mogelijkheid om BLI samen met SRR-MRI te gebruiken als een alternatief voor de anatomische referentie gebaseerd op CT, specifiek in longitudinale studies waar de herhaalde blootstelling aan straling in een CT scan een beperkende factor kan worden of een nadelig effect kan veroorzaken [7].

Hoofdstuk 6 en 7 waren gewijd aan een verkennende studie van de ontwikkeling van het brein. In **Hoofdstuk 6** was er een intuïtieve en makkelijk te gebruiken, specifieke visualisatie tool gebouwd die zij-aan-zij exploratie mogelijk maakt van heterogene, gecoregistreerde multi-contrast follow-up cross-sectionele MRI data. Het deformatieveld uit de registratiestap, werd gebruikt om automatisch corresponderende voxels in de getoonde datasets te linken. De determinant van de Jacobiaan (detJac) werd gebruikt voor een snellere en meer accurate visuele beoordeling en vergelijking van breindeformaties tussen de follow-up scans. Dit werd gecombineerd met een efficiënt data management schema. We onderzochten de functionaliteit en bruikbaarheid van onze tool in het onderzoeksgebied van de neuro imaging, door middel van een case study evaluatie met drie ervaren domein experts, gebruikmakend van longitudinale, cross-sectionele multi-contrast MRI rat brein data. Op basis van de uitgevoerde case study evaluatie concludeerden we dat de voorgestelde tool de visuele beoordeling van high-throughput data verbetert, en zeer nuttig is bij kwantitatieve studies.

Longitudinale studies naar brein pathologie en de beoordeling van therapeutische strategieën gaan ervanuit dat het brein volledig is volgroeid. Daarom is kennis over het exacte tijdstip van het bereiken van volwassenheid essentieel om het onderscheid te kunnen maken tussen ontwikkelingsfase en volwassenheid, en zo confounders in cerebrale ontwikkeling te excluderen. In **Hoofdstuk 7** was er een temporeel profiel van de postnatale brein ontwikkeling afgeleid, door longitudinale MRI metingen te combineren met histologisch weefselanalyses. Verschillende

hersenstructuren lieten een specifiek postnataal ontwikkelingspad zien. Waar het striatum volledig ontwikkeld leek bij drie maanden, was de cortex nog veranderlijk tot op zijn minst zes maanden. De gepresenteerde resultaten lieten overtuigend zien dat brein volume een betrouwbare indicator is voor stabilisatie van de hersenexpansie, terwijl het meten van de corticale dikte misleidend is bij ratten van twee tot drie maanden oud. Er waren duidelijke aanwijzingen voor aanhoudende ontwikkeling van het rattenbrein tot een leeftijd van drie maanden; in het bijzonder maken aanhoudende myelinatie in de cortex en het striatum het raadzaam om slechts te spreken van "volwassen dieren" vanaf een leeftijd van drie maanden. Toekomstig onderzoek naar ziektemodellen of laesies moeten deze drie maanden in beschouwing nemen als een veilige drempel, waarmee kan worden voorkomen dat aanhoudende hersenontwikkeling interfereert met de studie naar pathologische mechanismen.

Op basis van de in dit proefschrift gepresenteerde resultaten kunnen we concluderen dat al de geformuleerde doelen in zekere mate behaald zijn. Er is echter zeker ruimte voor verbetering en uitbreiding van dit werk in de toekomst. In **Hoofdstuk 2** werd een strategie geschetst om de atlassen gearticuleerd te maken, die kan omgaan met de belangrijkste posturele veranderingen (met betrekking tot lange botten of grote botstructuren); deze strategie kan echter uitgebreid worden naar het hele skelet om zo om te gaan met kleinere anatomische variaties. Men kan bijvoorbeeld een kinematisch model definiëren voor iedere ruggenwervel (waar we in dit werk de complete ruggengraat als een enkele botstructuur definiëren), en zelfs voor een aantal niet-rigide organen.

Hoofdstuk 3 beschrijft een segmentatietechniek die was ontwikkeld om om te gaan met een scenario wanneer een gecombineerde whole-body SPECT/CT botscan niet altijd geschikt of beschikbaar is. Dus, een van de beperkingen van de voorgestelde benadering is het gegeven dat het skelet voldoende tracer absorptie moet laten zien. Als dat niet het geval is, kan de registratie worden toegepast op de whole-body anatomische CT scan, gevolgd door een projectie van het CT geregistreerde model naar de SPECT data. Voorts, als de methode direct wordt toegepast op de SPECT scan en de corresponderende CT data niet beschikbaar is, dan heeft deze methode (minimale) gebruikers input nodig op het moment dat het skelet uit de data wordt geëxtraheerd. Wanneer whole-body CT data beschikbaar is, is deze gebruikersinput niet meer nodig, zoals aangetoond en uitgebreid gevalideerd in [1]. De gepresenteerde benadering kan worden toegepast op andere dieren, zolang er een adequate atlas beschikbaar is.

Hoofdstuk 4 presenteerde een eerste stap in de richting van een gearticuleerde atlas-gebaseerde skelet- en orgaanmapping voor MRI data, die op dit moment nog uitgebreide gebruikersinteractie nodig heeft om de rotatiepunten van de gewrichten te identificeren. Verdere automatisering van het atlas registratie proces kan bereikt worden door bijvoorbeeld een atlas-gebaseerde niet-rigide registratie toe te passen, gebruikmakend van mutual information as similariteitsmaat.

Hoofdstuk 5 beschreef een pilot studie naar de interactieve super-resolutie reconstructie in post mortem beelddata. Desalniettemin hebben we goede redenen om aan te nemen dat deze resultaten over te zetten zijn naar *in vivo* imaging. SRR is naar verwachting het meest succesvol voor relatief rigide structuren, zoals brein,

botweefsel en weefsel rondom botten: gevallen waar rigide registratie een accurate registratie geeft van de laag-resolute beelden.

De interactieve benadering om lokale VOIs te reconstrueren, heft de tijd- en geheugenbeperkingen op van SRR technieken in grote VOIs . Zoals te zien in Tabel 5.1 is de gemiddelde rekentijd voor het beste SRR resultaat, dus met 4 laag-resolutie beelden, toch nog in de orde van minuten—91.3 s. Deze resultaten zijn nog ver van de real-time doelstelling van deze aanpak. Een her-implementatie van het algoritme in een combinatie van C/C++ en GPU programmeeromgevingen zouden deze resultaten kunnen verbeteren.

De gepresenteerde workflow kan naast de gepresenteerde oncologische toepassing, ook van waarde zijn in veel andere onderzoeksgebieden waar whole-body verificatie van lokale ((sub-) plakdikte groot) effecten nodig zijn. Voorbeelden zijn de migratie van gelabelde stamcellen na een systemische injectie, of het afbeelden van systemische ontstekingsziekten.

Het platform voor intuïtieve, geïntegreerde visualisatie en exploratie van high-throughput, geregistreerde multi-modale, cross-sectionele follow-up data zoals gepresenteerd in **Hoofdstuk 6** zou gebaat zijn bij van de combinatie met een beeldregistratiepakket zoals bijvoorbeeld `elastix`, en ook van functies die het mogelijk maken om ROIs in te tekenen en te kwantificeren. De voorgestelde tool zal publiek beschikbaar worden gemaakt voor download via www.lkeb.nl

Referenties

[1].   Baiker M., Milles J., Dijkstra J. *et al. Atlas-based whole-body segmentation of mice from low-contrast micro-CT data* Med Image Anal 14(6): 723–737 2010

[2].   Landis J. R. and Koch G. G. *The measurement of observer agreement for categorical data* Biometrics 33(1): 159–174 1977

[3].   Bartko J. J. *Measurement and reliability: statistical thinking considerations* Schizophrenia Bulletin 17(3): 483–489 1991

[4].   Chaudhari A. J., Joshi A. A., Darvas F. *et al. A method for atlas-based volumetric registration with surface constraints for optical bioluminescence tomography in small animal imaging* Proc SPIE Medical Imaging 6510 Part 2: 651024 2007

[5].   Joshi A. A., Chaudhari A. J., Shattuck D. W. *et al. Posture Matching and Elastic Registration of a Mouse Atlas to Surface Topography Range Data* Proc IEEE Intl Symp on Biomedical Imaging 366–369 2009

[6].   Baiker M., Dijkstra J., Que I. *et al. Organ approximation in μCT data with low soft tissue contrast using an articulated whole-body atlas* Proc IEEE Intl Symp on Biomedical Imaging 1267–1270 2008

[7].   Hindorf C., Rodrigues J., Boutaleb S. *et al. Total absorbed dose to a mouse during microPET/CT imaging* Eur J Nucl Med Mol Imaging 37: S274 2010

List of publications

Peer-reviewed papers in international journals

A. Khmelinskii, E. Plenge, P. Kok, O. Dzyubachyk, T. J. A. Snoeks, D. H. J. Poot, C. W. G. M. Löwik, C. P. Botha, W. J. Niessen, E. Meijering, L. van der Weerd and B. P. F. Lelieveldt **Interactive local Super-Resolution Reconstruction of MRI whole-body mouse data: applications to bone and kidney metastases** *submitted* 2013

L. Mengler, A. Khmelinskii, M. Diedenhofen, C. Po, M. Staring, B. Lelieveldt and M. Hoehn **Brain maturation of the adolescent rat cortex and striatum: changes in volume and myelination** *NeuroImage, Volume 84, Pages 35–44 2014*

A. Khmelinskii, H. C. Groen, M. Baiker, M. de Jong and B. P. F. Lelieveldt **Segmentation and visual analysis of whole body microSPECT mouse data** *PLoS ONE, 7(11): e48976. doi:10.1371/journal.pone.0048976 2012*

T. J. Snoeks, A. Khmelinskii, B. P. F. Lelieveldt, E. L. Kaijzel and C. W. G. M. Löwik **Optical advances in skeletal imaging applied to bone metastases** *Bone, Volume 48, Issue 1, Pages: 106–114 2011*

A. Khmelinskii and M. Baiker, E. L. Kaijzel, J. Chen, J. H. C. Reiber and B. P. F. Lelieveldt **Articulated whole-body atlases for small animal image analysis: construction & applications** *Molecular Imaging and Biology, Volume 13, Issue 5, Pages: 898–910 2011*

A. Khmelinskii, R. Ventura and J. Sanches **A novel metric for bone marrow cells chromosome pairing** *IEEE Transactions on Biomedical Engineering, Volume 57, Issue 6, Pages: 1420–1429 2010*

Peer-reviewed full papers in international conference proceedings

A. Khmelinskii, L. Mengler, P. Kitslaar, M. Staring, M. Hoehn and B. Lelieveldt **A visualization platform for high-throughput, follow-up, co-registered multi-contrast MRI rat brain data** *Proceedings of SPIE Medical Imaging: Biomedical Applications in Molecular, Structural, and Functional Imaging February 9–14, Lake Buena Vista, FL, U.S.A., Pages: 8672: 86721W–86721W-7 2013*

A. Khmelinskii, E. Plenge, P. Kok, O. Dzyubachyk, D. H. J. Poot, E. Suidgeest, C. P. Botha, W. J. Niessen, L. van der Weerd, E. Meijering and B. P. F. Lelieveldt **Super-resolution reconstruction of whole-body MRI mouse data: an interactive approach** *Proceedings of the 9th IEEE International Symposium on Biomedical Imaging: From Nano to Macro, May 2–5, Barcelona, Spain, Pages: 1723–1726 2012*

A. Khmelinskii, M. Baiker, P. Kok, J. de Swart, J. H. C. Reiber, M. de Jong and B. P. F. Lelieveldt **Atlas-based articulated skeleton segmentation of μSPECT mouse data** *Proceedings of the 8th IEEE International Symposium on Biomedical Imaging: From Nano to Macro, March 30–April 2, Chicago, Illinois, U.S.A., Pages: 437–440 2011*

R. Ventura, A. Khmelinskii and J. Sanches **Classifier-assisted metric for chromosome pairing** *Proceedings of the IEEE EMBC'10 – 32nd Annual International Conference of the IEEE EMBS, August 31–September 4, Buenos Aires, Argentina, Pages: 6729–6732 2010*

A. Khmelinskii, M. Baiker, X.J. Chen, J. H. C. Reiber, R. M. Henkelman and B. P. F. Lelieveldt **Atlas-based organ & bone approximation for ex-vivo μMRI mouse data: a pilot study** *Proceedings of the 7th IEEE International Symposium on Biomedical Imaging: From Nano to Macro, April 14–17, Rotterdam, the Netherlands, Pages: 1197–1200 2010*

A. Khmelinskii, R. Ventura and J. Sanches **Automatic chromosome pairing using mutual information** *Proceedings of the IEEE EMBC'08—30th Annual International Conference of the IEEE EMBS, August 20–24, Vancouver, Canada, Pages: 1918–1921 2008*

A. Khmelinskii, R. Ventura and J. Sanches **Chromosome pairing for karyotyping purposes using mutual information** *Proceedings of the 5th IEEE International Symposium on Biomedical Imaging: From Nano to Macro, May 14–17, Paris, France, Pages: 484–487 2008*

Data made publicly available

Lisbon K-1 chromosome dataset
http://mediawiki.isr.ist.utl.pt/wiki/Lisbon-K_Chromosome_Dataset

Articulated small animal's skeletons
www.lkeb.nl

Conference abstracts

D. I. Bink, K. A. Ritz, C. Mackaaij, C. M. van der Loos, O. J. de Boer, A. Khmelinskii, L. van der Weerd and M. J. A. P. Daemen **The effect of cardiovascular risk factors and cerebral hypoperfusion on brain structure and cognitive functioning** *Cardio Vasculaire Conferentie, March 14–15, Noordwijkerhout, the Netherlands 2013*

D. I. Bink, K. A. Ritz, C. Mackaaij, C. M. van der Loos, O. J. de Boer, A. Khmelinskii, L. van der Weerd and M. J. A. P. Daemen **The effect of cardiovascular disease and cerebral hypoperfusion on the brain** *European Society of Cardiology Congress, August 31–September 4, Amsterdam, the Netherlands 2013*

L. Mengler, A. Khmelinskii, M. Diedenhofen, C. Po, M. Staring, B. P. F. Lelieveldt and M. Hoehn **When is a young rat brain adult? Volume and myelination**

changes in cortex and striatum *European Molecular Imaging Meeting, May 26–28, Torino, Italy 2013*

D. I. Bink, K. A. Ritz, L. van der Weerd, A. Khmelinskii and M. J. A. P. Daemen **The effect of cardiovascular risk factors and cerebral hypoperfusion on brain structure and cognitive functioning** *3rd Rembrandt Symposium, November 29, Noordwijkerhout, the Netherlands 2012*

H. C. Groen, A. Khmelinskii, M. de Jong and B. P. F. Lelieveldt **Segmentation of whole-body microSPECT mouse skeleton scans** *Annual Congress of the European Association of Nuclear Medicine, October 27–31, Milan, Italy 2012*

H. C. Groen, A. Khmelinskii, S. Berndsen, B. P. F. Lelieveldt and M. de Jong **Comparison of manual and automatic quantification of bone 99mTc-HDP SPECT/CT mouse scan** *Annual Congress of the European Association of Nuclear Medicine, October 27–31, Milan, Italy 2012*

H. C. Groen, A. Khmelinskii, M. de Jong and B. P. F. Lelieveldt **Segmentation of whole-body microSPECT mouse skeleton images** *World Molecular Imaging Congress, September 5–8, Dublin, Ireland 2012*

H. C. Groen, A. Khmelinskii, S. Berndsen, B. P. F. Lelieveldt and M. de Jong **Comparison of manual and automatic quantification of bone 99mTc-HDP SPECT/CT mouse scans** *World Molecular Imaging Congress, September 5–8, Dublin, Ireland 2012*

A. Khmelinskii, E. Plenge, P. Kok, D. Poot, O. Dzyubachyk, C. P. Botha, E. Suidgeest, W. Niessen, L. van der Weerd, E. Meijering and B. P. F. Lelieveldt **Towards interactive super-resolution resolution reconstruction of whole-body MRI mouse data** *International Society for Magnetic Resonance in Medicine, Annual Meeting & Exhibition, May 5–11, Melbourne, Australia 2012*

A. Khmelinskii, H. C. Groen, M. de Jong and B. P. F. Lelieveldt **Segmentation of whole-body microSPECT mouse data** *Hot Topics in Molecular Imaging, April 15–20, Les Houches, France 2012*

A. Khmelinskii, E. Plenge, P. Kok, O. Dzyubachyk, D. Poot, E. Suidgeest, C. P. Botha, W. Niessen, L. van der Weerd, E. Meijering and B. P. F. Lelieveldt **Super-resolution reconstruction of whole-body MRI mouse data** *Hot Topics in Molecular Imaging, April 15–20, Les Houches, France 2012*

L. Mengler, A. Khmelinskii, C. Po, M. Staring, B. Lelieveldt and M. Hoehn **Mapping postadolescent brain development in rat frontal cortex: changes in volume and cell density** *Neuroscience, November 12–18, Washington, DC, U.S.A. 2011*

A. Khmelinskii, L. Mengler, P. Kitslaar, M. Staring, C. Po, J. H. C. Reiber, M. Hoehn and B. Lelieveldt **Interactive system for exploration of multi-modal rat brain data** *European Molecular Imaging Meeting, June 19–21, Leiden, the Netherlands 2011*

L. Mengler, A. Khmelinskii, C. Po, M. Staring, J. H. C. Reiber, B. Lelieveldt and M. Hoehn **Juvenile development and ageing mediated changes in cortical structure and volume in the rat brain** *European Molecular Imaging Meeting, June 19–21, Leiden, the Netherlands 2011*

T. J. Snoeks, A. Khmelinskii, I. Que, B. P. F. Lelieveldt, E. L. Kaijzel and C. W. G. M. Löwik **A method to follow tumor growth and tumor induced bone loss simultaneously over time, in vivo, using whole body bioluminescence fluorescence imaging** *10th International Conference on Cancer-Induced Bone Disease, September 22–25, Sheffield, United Kingdom, 2010, Bone, Volume 48, Issue 1, Pages: S49–S50 2011*

T. Snoeks, A. Khmelinskii, I. Que, B. P. F. Lelieveldt, E. Kaijzel and C. Löwik **A method to follow tumor induced bone loss over time, in vivo, using whole body fluorescence imaging** *World Molecular Imaging Congress, September 8–11, Kyoto, Japan 2010*

A. Khmelinskii, R. Ventura and J. Sanches **Chromosome pairing using mutual information in bone marrow cells** *Proceedings of the 15th Portuguese Conference on Pattern Recognition, October 23, Aveiro, Portugal 2009*

A. Khmelinskii, R. Ventura, M. Carmo-Fonseca and J. Sanches, **Automatic pairing of metaphase chromosomes with mutual information for karyotyping purposes,** *1st Annual Portuguese Forum on Computational Biology, Gulbenkian Institute of Science, July 10–12, Oeiras, Portugal 2008*

A. Khmelinskii, R. Ventura and J. Sanches, **Chromosome pairing for karyotyping purposes,** *Proceedings of the 13th Portuguese Conference on Pattern Recognition, October 26, Lisbon, Portugal 2007*

Thesis

A. Khmelinskii, **Multi-modal small-animal imaging: image processing challenges and applications,** Ph.D., *Leids Universitair Medisch Centrum, Universiteit Leiden, October 9, Leiden, the Netherlands 2013*

A. Khmelinskii, **Chromosome pairing for karyotyping purposes,** M.Sc., *Instituto Superior Técnico, November 14, Lisbon, Portugal 2007*

Curriculum vitae

Artem Khmelinskii was born in Novosibirsk, Russia, on April 8, 1984. After obtaining his high-school diploma in natural sciences from Escola Secundária João de Deus, Faro, Portugal, he began his studies in Biomedical Engineering at Instituto Superior Técnico (IST), Universidade Técnica de Lisboa, Lisbon, Portugal. He received his M. Sc. degree in November 2007 and continued his research on the subject of chromosome pairing in the same Institute for Systems and Robotics–IST from November 2007 till June 2008. From June 1st 2008 till now 2013 he's been a researcher and a Ph. D. student in the section of Kennisgestuurde Beeldverwerking (KGB) at the LKEB–LUMC, Universiteit Leiden, Leiden, the Netherlands. The results of his work on image processing applied to multi-modal small animal imaging are described in this thesis